LOW-COST MOTOR DRIVE EMBEDDED FAULT DIAGNOSIS SYSTEMS

A Dissertation

by

BILAL AKIN

Submitted to the Office of Graduate Studies of
Texas A&M University
in partial fulfillment of the requirements for the degree of

DOCTOR OF PHILOSOPHY

August 2007

Major Subject: Electrical Engineering

LOW-COST MOTOR DRIVE EMBEDDED FAULT DIAGNOSIS SYSTEMS

A Dissertation

by

BILAL AKIN

Submitted to the Office of Graduate Studies of
Texas A&M University
in partial fulfillment of the requirements for the degree of

DOCTOR OF PHILOSOPHY

Approved by:

Chair of Committee, Hamid A. Toliyat
Committee Members, Shankar. P. Bhattacharyya
Karen Butler-Purry
Mark Holtzapple
Head of Department, Costas N. Georghiades

August 2007

Major Subject: Electrical Engineering

ABSTRACT

Low-Cost Motor Drive Embedded Fault Diagnosis Systems.

(August 2007)

Bilal Akin, B.S., Middle East Technical University, Ankara, Turkey;

M.S., Middle East Technical University, Ankara, Turkey

Chair of Advisory Committee: Dr. Hamid A. Toliyat

Electric motors are used widely in industrial manufacturing plants. Bearing faults, insulation faults, and rotor faults are the major causes of electric motor failures. Based on the line current analysis, this dissertation mainly deals with the low cost incipient fault detection of inverter-fed driven motors. Basically, low order inverter harmonics contributions to fault diagnosis, a motor drive embedded condition monitoring method, analysis of motor fault signatures in noisy line current, and a few specific applications of proposed methods are studied in detail.

First, the effects of inverter harmonics on motor current fault signatures are analyzed in detail. The introduced fault signatures due to harmonics provide additional information about the motor faults and enhance the reliability of fault decisions. It is theoretically and experimentally shown that the extended fault signatures caused by the inverter harmonics are similar and comparable to those generated by the fundamental harmonic on the line current.

In the next chapter, the reference frame theory is proposed as a powerful toolbox to find the exact magnitude and phase quantities of specific fault signatures in real time. The faulty motors are experimentally tested both offline, using data acquisition system, and online, employing the TMS320F2812 DSP to prove the effectiveness of the proposed tool. In addition to reference frame theory, another digital signal processor (DSP)-based phase-sensitive motor fault signature detection is presented in the following chapter. This method has a powerful line current noise suppression capability while detecting the fault signatures. It is experimentally shown that the proposed method can determine the normalized magnitude and phase information of the fault signatures even in the presence of significant noise.

Finally, a signal processing based fault diagnosis scheme for on-board diagnosis of rotor asymmetry at start-up and idle mode is presented. It is quite challenging to obtain these regular test conditions for long enough time during daily vehicle operations. In addition, automobile vibrations cause a non-uniform air-gap motor operation which directly affects the inductances of electric motor and results quite noisy current spectrum. The proposed method overcomes the challenges like aforementioned ones simply by testing the rotor asymmetry at zero speed.

To my family

ACKNOWLEDGMENTS

I would like to thank my advisor, Dr. Hamid A. Toliyat, for his support, continuous help, patience, understanding and willingness throughout the period of the research to which this thesis relates. I am very grateful to work with such a knowledgeable and insightful professor.

I would also like to thank the members of my graduate study committee, Dr. Karen Butler, Dr. S.P. Bhattacharyya, and Dr. Mark Holtzapple for accepting my request to be a part of the committee.

I would like to extend my gratitude to my fellow colleagues in the Advanved Electric Machine and Power Electronics Laboratory: Baris Ozyurt, Dr. Peyman Niazi, Dr. Leila Parsa, Salman Talebi, Dr. Namhun Kim, Nicholas Frank, and Steven Campbell. Furthermore, special thanks goes to Dr. Peyman Asadi for his sincere friendship and support during my hard times.

Also, I would like to express my gratitude toward my friends here in College Station for their support and companionship throughout my four years in town. In particular, I would like to thank Osman Cizmeci, Taner Sumesaglam, Renat Shaykhutdinov, Daniyar Zhussupov, Ahmet Caliskan, Bekir Engin Eser, Ferhat Akbas, Omer Faruk Vural and Sami Keskek. I would also like to acknowledge the Electrical Engineering department, staff at Texas A&M University: Ms. Tammy Carda, Ms. Linda Currin, Ms. Gayle Travis and many others for providing an enjoyable and educational atmosphere.

TABLE OF CONTENTS

LIST OF FIGURES

FIGURE Page

FIGURE Page

FIGURE Page

FIGURE Page

LIST OF TABLES

TABLE Page

CHAPTER I

INTRODUCTION

1.1. Electric Motor Faults and Their Diagnosis

The industry's dependence on AC machines in critical applications often results in very costly shut-downs due to motor failures. Therefore, fault diagnosis and condition monitoring have been studied in the recent decade to prevent costly interruptions due to motor faults. As a widely applied method, phase current analysis has received much attention in search of providing a practical solution to continuous monitoring and incipient fault detection [1-4]. Although vibration analysis with accelerometers and thermal analysis provides satisfactory results [5-7] in addition to traditional current signal analysis, continual low cost protection without the use of extra sensors and hardware is always the most attractive method for a greater market share. Furthermore, practical issues in industrial facilities where a number of motors run simultaneously increase the tendency towards motor current signature analysis due to the shortcomings of aforementioned methods .

Recently, on-line condition monitoring of electric motors has attracted a great attention. On-line systems provide early warning of motor faults which allows for adequate warning of imminent failures, diagnosing present maintenance needs, schedule

---

This dissertation follows the style and format of *IEEE Transactions on Industry Applications.*

future preventive maintenance and repair work, minimum downtime and optimum maintenance schedules. Furthermore, on line diagnosis allows user to have the necessary spare parts before the machine is stripped down, thereby reducing outage times. Diagnostics results can be integrated into the maintenance policy, therefore the usual maintenance at specified intervals can be replaced by a condition-based maintenance [8]. In opposite to offline methods, which require interruption of motor operation, online methods provide motor diagnostics during motor operation. Among these, some of the online motor current analysis do not require additional expensive measurement devices or complicated hardware system.

Line current information of inverter fed motors is readily available for control and protection purposes. Thus, the new trend for low cost protection is the motor drive-integrated fault diagnosis systems without using any external hardware. Although the practical problems of utility driven systems fault diagnosis are well known, inverter driven systems need further analysis to overcome problems such as high noise floor of current spectrum and operating point dependent fault signature frequencies.

Even though numerous offline fault detection methods are reported using complex software and hardware [2-4], the implementation of a low-cost real time monitoring has still been a challenge due to the involved computational complexity and expensive hardware. In order to achieve low-cost online monitoring, the diagnosis algorithms should be simple enough to be executed using industrial microprocessors in real time. Since thousands of data are processed, and the number of data is a critical parameter for precision, the proposed solutions should avoid storing or buffering data.

One of the most commonly used signal-based techniques is the fast Fourier transform (FFT) method [1-4], [6]. The main duty of the FFT-radix algorithms is to reduce the complexity by decomposing the discrete Fourier transforms (DFTs) into smaller DFTs in a recursive manner [9-10]. In order to compute the DFT of discritized signals, all signal data should be stored and indexed. In order to obtain high resolution and accurate results in inverter driven systems, a large number of data points should be buffered due to low signal frequency and high switching frequency constraints. Therefore, implementing FFT algorithms in real time using cheap industrial processors is a challenging task.

Inverter driven motor phase currents are influenced by many factors such as static and dynamic loading, motor speed transients, etc. Therefore, the phase currents and modulated operating point dependent fault signatures are accepted as non-stationary signals [11]. However, it is well known that Fourier transform techniques are not sufficient to represent non-stationary signals. When a non-stationary signal is transformed into the frequency domain, most of the information about the transient components of the signal is lost [12-13]. Even the techniques such as short time Fourier transform, where a non-stationary signal is divided into short pseudo-stationary segments, are not suitable for the analysis of signals with complex time-frequency characteristics [11-12]. During the experimental stage, it is reported that the partial use of these methods suffers from hardware limitations of low-cost real time monitoring systems.

In this dissertation, a simple motor drive-integrated fault diagnosis method is proposed and implemented using the core microprocessor of the inverter, Texas Instruments digital signal processor (DSP) TMS320F2812. As a diagnosis tool, the reference frame theory is employed to measure the normalized amplitude of fault related harmonics. Instead of checking the whole current spectrum, each time only a few fault related harmonics are checked to speed up the process and lower the computational burden.

The rotating frame transformation algorithm is quite simple and short; therefore, it is directly embedded into the main motor control subroutine. Because the stator frequency and shaft speed are mostly available as drive control parameters, the frequency of each fault signature harmonic is updated dynamically using these parameters. These updated frequencies are utilized to synchronize the rotating frame with fault harmonic vectors to watch the motor condition not only at steady state, but also during transients. Furthermore, since each measured data is processed in real time instead of buffering, the method does not suffer from memory shortage. The tests under non-ideal conditions such as offset, unbalance, etc. proved that they do not affect the results. The average of transformed signal into rotating frame converges and settles down to a dc level quite fast; therefore the diagnosis process can be finalized in a few seconds.

1.2. Motor Faults and Detection Techniques

A. Bearing Faults

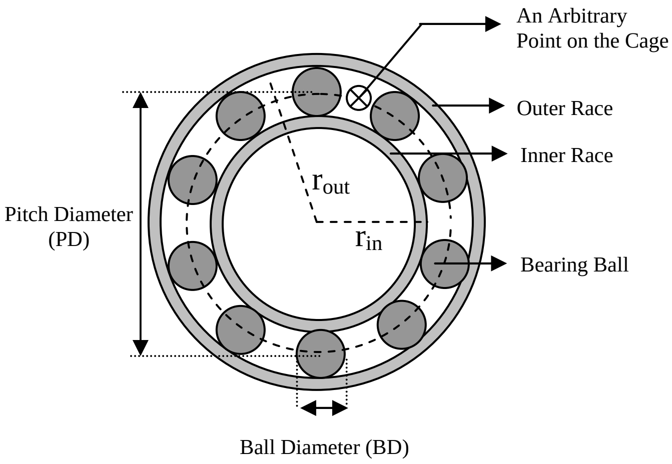

Fig. 1.1. A typical bearing geometry.

Most of the bearings in industrial facilities run under non-ideal conditions and are subject to fatigue, ambient vibration, overloading, misalignment, contamination, current fluting, corrosion, and wrong lubrication. These non ideal conditions start negligible defects that spread and propagate on the inner raceway, outer raceways and rolling elements. After a while the defect becomes significant and generates mechanical vibration causing audible noise. Basically, bearing faults can be classified as outer race, inner race, ball defect and cage defect, which are the main sources of machine vibration. These mechanical vibrations in the air-gap due to bearing faults can be considered as slight rotor displacements which result in instant eccentricities. Therefore, the basic fault signature frequency equation of line current due to bearing defects is adopted from eccentricity literature [2].

Mechanical vibration, infrared or thermal, and acoustic analyses are some of the commonly used predictive maintenance methods to monitor the health of the bearings to prevent motor failures. Vibration and thermal monitoring require additional sensors or transducers to be fitted on the machines. While some large motors may already come with vibration and thermal transducers, it is not economically or physically feasible to provide the same for smaller machines. Then, the small to medium size motors are checked periodically by moving portable equipment from machine to machine in all three methods. Some motors used in critical applications such as nuclear reactor cooling pump motors may not be easily accessible during reactor operation. The lack of continuous monitoring and accessibility are the shortcomings of the aforementioned techniques. An alternate approach based on current monitoring has received much research attention in search of providing a practical solution to continuous monitoring and accessibility problems. Motor current monitoring provides a non-intrusive way to continuously monitor motor reliability with minimal additional cost.

Bearing faults can be classified as outer race, inner race, ball defect and cage defect, which are the main sources of machine vibration. These mechanical vibrations in the air-gap can be considered as slight rotor displacements which result in instant eccentricities. Therefore, the basic fault signature frequency equation of line current due to bearing defects is adopted from eccentricity literature [2].

Each fault has specific vibration frequency components that are characteristic of each defect type which is a function of both bearing geometry and rotor speed [14]. The middle point between the outer and inner raceways assumed as the reference point in order to develop mechanical vibration characteristic frequency expressions. Basically, the middle point velocity, w_x, is the mean of inner and outer race linear velocities as given by

$$w_x = \frac{V_x}{r_x} = \frac{w_{in} r_{in} + w_{out} r_{out}}{2r_x} \tag{1.1}$$

where r_x is the radius of cage, w_{in} and w_{out} are the angular velocity of inner and outer raceways, r_{in} and r_{out} are the radius of inner and outer raceways, respectively. The respective rotational frequencies are f_x, f_{out} and f_{in}, therefore,

$$f_x = \frac{f_{in} r_{in} + f_{out} r_{out}}{2r_x} \tag{1.2}$$

The outer raceway defect frequency f_{ord} is associated to the rate at which the balls pass a defect point on the outer race. Obviously, the frequency increases linearly with the number of balls, therefore the outer race defect frequency is calculated by multiplying the number of balls with the difference of the reference point and the outer race frequencies as given by

$$\begin{aligned} f_{ord} &= n\left|f_x - f_{out}\right| \\ &= n\left|\frac{f_{in} r_{in} + f_{out} r_{out}}{2r_x} - f_{out}\right| \\ &= \frac{n}{2}\left|(f_{in} - f_{out})(1 - \frac{BD\cos\beta}{PD})\right| \end{aligned} \tag{1.3}$$

where n is the number of balls, β is the contact angle, BD and PD are the ball and pitch diameters, respectively. Since the outer race is stationary and the inner race rotates at the same speed as the rotor shaft, the characteristic outer race defect vibration frequency is rewritten as

$$f_{ord} = \frac{n}{2} f_{rmech} (1 - \frac{BD}{PD} \cos \beta) \tag{1.4}$$

following the same method for inner race, the characteristic inner race defect vibration frequency f_{ird} can be found as

$$f_{ird} = \frac{n}{2} f_{rmech} (1 + \frac{BD}{PD} \cos \beta) \tag{1.5}$$

where f_{rmech} is the mechanical rotor speed.

The mechanical oscillations due to bearing faults change the air-gap symmetry and machine inductances like eccentricity faults. The machine inductance variations are reflected to the stator current in terms of current harmonics, which are the indicators of bearing fault associated with mechanical oscillations in the air-gap. Therefore, the bearing fault current harmonic frequencies are given in (1.6) employing the previously found mechanical characteristic frequencies.

$$f_{cf} = \left| f_1 \pm m f_v \right| \tag{1.6}$$

where f_1 is the fundamental stator (carrier) frequency, f_v is the characteristic mechanical vibration (modulation) frequency due to bearing fault and m is an integer.

A generic condition diagnosis tool based on discriminative energy functions is proposed by [15]. These energy functions reveal discriminative frequency-domain regions where failures are identified. Schoen [16] implemented an unsupervised, online system for induction motor based on motor line current. An amplitude modulation (AM) detector is developed to detect the bearing fault while it is still in an incipient stage of development in [17]. In [12], a hidden Markov modeling (HMM) based bearing fault detection and fault diagnosis is developed. Yazici [11], proposed an adaptive statistical time-frequency method for detection of broken bars and bearing faults in motors using stator current.

B. Stator Faults

The major function of insulation materials normally is to withstand electric stress; however, in many cases it must also endure other stresses such as mechanical, environmental etc. Most of the time the insulation has as a prime function the support of electric conductors as in the case of electric machines [18]. In a motor the torque is the result of the force created by current in the conductor and surrounding magnetic field. This shows that insulation must have electrical as well as mechanical properties to withstand mechanical stresses [19]. In addition, electromagnetic vibration twice the power frequency, differential expansion forces due to the temperature variations following load changes, and impact forces due to electrical/mechanical asymmetries are also effective in aging process [20].

Non uniform temperature distribution in a motor will also cause mechanical destruction due to dilation. The manufacturing process itself may constitute a damaging or aging action. The electrical insulation must be strong enough in order to withstand the mechanical abuse while being wounded and installed in motor. Thus, the mechanical stresses are often very severe compared to the subsequent abuse the insulation gets in service [19].

Increased temperatures can cause a number of effects. The material may be inherently weaker at elevated temperatures and a failure may occur simply because of the melting of the material. This can be a very short time failure, because of the short length of time required for the temperature to rise to the melting point. On the other hand, long term elevated temperature can cause internal chemical effects on material [18].

Thermal stress is probably the most recognized cause of insulation degradation and ultimate failure. The main sources of thermal stress in electric machinery are cupper losses, eddy current and stray load losses in the cupper conductors, plus additional losses heating due to core losses, windage etc [21]. High temperature causes a chemical reaction which makes insulation material brittle. Another problem is sudden temperature increase of cupper conductor expand the cupper bars faster than insulation material which cause stress on groundwall insulation [18].

Another significant effect on insulation aging is partial discharges (PD). Partial discharges are small electric sparks that occur within air bubbles in the insulation material due to non uniform electric field distribution. Once begun, PD causes progressive deterioration of insulating materials, ultimately leading to electrical breakdown. On the other hand, motor winding insulation experiences higher voltage stresses when used with an inverter than when connected directly to the a.c. mains supply. The higher stresses are dependent on the motor cable length and are caused by the interaction of the fast rising voltage pulses of the drive and transmission line effects in the cable [22, 23].

In addition to causes given above, delaminating discharges, enwinding discharges, moisture attacks, abrasive material attacks, chemical decomposition, and radiation can also be counted as accelerating effects on aging of insulation [24].

Motor / Generator stator insulation failure during machine operation can lead to a catastrophic machine failure resulting in a costly outage. Prevention of such an outage is a major concern for both the machine manufacturer and user, since it can result in significant loss of revenue during the outage as well as repair or replacement cost. In the literature [18, 24], PD is taken as a signature of isolation aging which begins within voids, cracks, or inclusions within a solid dielectric, at conductor-dielectric interfaces within solid or liquid dielectrics, or in bubbles within liquid dielectrics. Once begun, PD causes progressive deterioration of insulating materials, ultimately leading to electrical breakdown.

When a partial discharge occurs, the event may be detected as a very small change in the current drawn by the sample under test. PD currents are difficult to measure because of their small magnitude and short duration [24]. Therefore, PD in a motor/ generator before a breakdown does not have significant effect on power system.

The most serious result of a major fault is which may not only destroy the machinery but may spread in the system and cause total failure. The most common type of fault which is also the most dangerous one is the breakdowns which may have several consequences. A great reduction of the line voltage over a major part of the power system will be observed. If an alternator is damaged, this might affect the whole system. For example, when a tolerable inter-turn or in-phase fault occurs, the power generation will be unbalanced and the power quality will decrease drastically. Extra harmonics will be injected to the whole system. If the alternator fault is not tolerable or it is phase to phase fault, then the surge will damage the machine itself and some parts of the system. Unlike a motor connected to the utility following a few step-down transformers, the generator faults are more risky in terms of permanent damages and costly shutdowns depending on the network structure. A motor with tolerable inter-turn short behaves like an unbalanced load and disturb the neighboring utility. However, an alternator failure affects the whole system where a motor failure has limited affect on the power system. In both of the case the power quality of the power system will be degraded.

In the literature there are several methods for condition monitoring and protection of motors/generators. The superiority of these methods depends on the type of application, power rating of the machinery, location of the machinery, cost of machine itself and sensors etc. [23, 24].

Monitoring the temperature of the high power motor/generator stator winding, it is possible to determine if the winding is at risk of thermal deterioration. This can be done either by embedded thermocouples or thermal cameras. In addition, by monitoring the temperature, an increase in stator temperature over time under the same operating conditions (load, ambient temperature and voltage) can be indication of the cooling system failure.

Ozone (O_3) gas generation occurs as a consequence of PD on the stator coil. Surface partial discharges are the cause of deterioration from defective slot and end-winding stress relief coatings, as well as conductive pollution. By monitoring the ozone gas concentration over time, failure mechanisms that give rise to the surface partial discharge can be detected [25]. Thus ozone monitoring does not find problems in the very early stages of deterioration. Ozone monitoring can be done periodically with inexpensive chemical detectors that are thrown away after each use. Otherwise, continuous ozone monitoring is now feasible with electronic detectors.

In addition, phase and ground fault relays are installed in a machine to prevent severe machine damage caused by insulation failure [19]. Another effective solution is online monitoring of partial discharge that warns the user before a catastrophic damage. This can be done either by monitoring differential phase current or using some special sensors such as antennae, HV capacitors on the machine terminals, and/or radio frequency (RF) current transformers at the machine neutral or on surge capacitor grounds, are needed to detect the PD. These sensors are sensitive to the high frequency signals from the PD, yet are insensitive to the power frequency voltage and its harmonics [24].

C. Broken Rotor Bar Fault

Cage rotors are basically of two types: cast and fabricated. Previously, cast rotors were only used in small machines. Today, casting technology can be used even for rotors of machines in the range of thousands kW. Almost all squirrel cage motor bars and end rings are made of alloys of either aluminum or copper or pure copper. Copper and copper alloy rotors are usually of fabricated design. Aluminum rotors are dominantly die-cast constructions, with the bars and end rings are being cast in one machine operation. Cast rotors, although more rugged than the fabricated type, can hardly be repaired once faults like cracked or broken rotor bars develop in them.

There a lot of reasons cause rotor bar and end-ring breakage. They can be caused by thermal, magnetic, dynamic, environmental, mechanical and residual stresses. Normally, the stresses remain within the tolerance bandwidth and the motor operates properly fir years. When any of these stresses are above allowable levels, the lifetime of motor shortened.

A broken rotor bar can be considered as rotor asymmetry [8, 14] that cause unbalanced currents, torque pulsation and decreased average torque [15]. The electric and magnetic asymmetry in induction machine rotors boosts up the left hand side sideband of excitation frequency [8]. The broken rotor bar fault signatures frequency around the fundamental is modeled as:

$$f_{left\_sideband} = (1 \pm 2s) f_e \tag{1.7}$$

where the left sideband is due to electrical asymmetry and the right sideband is due to the speed oscillations. Due to the electrical and mechanical interactions inside the motor, the model of fault frequency can be extended as [26]:

$$f_{left\_sideband} = (1 \pm 2ks) f_e \qquad k = 1, 2, 3 \ldots \tag{1.8}$$

The motor-load inertia also affects the magnitude of these sidebands. Other components in the current spectrum are given by [1]

$$f_{left\_sideband} = \left[\left(\frac{k}{p}\right)(1-s) \pm s\right] f_e \tag{1.9}$$

k = Harmonic index (k/p =1,3,5,…)
s = Per unit slip
p = Number of fundamental pole pairs
f_e= Supply frequency

In [27], it is shown that broken bar fault can be detected by time and frequency domain analysis of induced voltages in search coils placed in the motor. During regular operations, a symmetrical stator winding excited at frequency f_e induces rotor bar currents at sf_e frequencies [26]. When an asymmetry is introduced in the rotor structure, the backward rotating negative sequence $-sf_e$ components start the chain electrical and mechanical interactions between rotor and stator of the motor. Initially, stator EMF at frequency $(1-2s)f_e$ is induced that cause torque and speed ripples. Afterwards, torque and speed ripples are reflected to the stator as line current oscillations at frequency $(1+2s)f_e$. Next, $(1+2s)f_e$ component induces rotor currents at $\pm 3sf_e$ and this chain reaction goes on until completely being filtered by the rotor inertia. A parameter estimation based broken bar detection is reported in [28]. The harmonics at the stator terminal voltages immediately after switching off the motor can al be used as a diagnostic method [29].

D. Eccentricity Fault

Air gap eccentricity is known as a condition that occurs when there is a non-uniform distance between the rotor and stator in the air gap. When there is an eccentricity in the air gap, varying inductances cause unbalanced magnetic flux with in the air gap that creates fault harmonics in the line current which can be identified in the spectrum. There are two types of eccentricity: static and dynamic. When static eccentricity occurs, the centerline of the shaft is at a constant offset from center of the stator or rotor is misaligned along the stator bore. On the other hand when dynamic eccentricity occurs, the centerline of the shaft is at a variable offset from center of the stator or minimum air gap revolves with the rotor. If the distance between the stator bore and rotor is not equal throughout the entire machine, varying magnetic flux within the air gap creates imbalances in the current flow, which can be identified in the current spectrum. Improper mounting, loose or missing bolt, misalignment, rotor unbalance might be causes of air gap eccentricity.

Eccentricity is a quite well-known problem and analytical results supported by experiments have already been reported. In the literature, there are several successful works reporting diagnosis of eccentricity based on line current measurement studied by Nandi, Dorrell, and Debortoli.

Unlike bearing faults, it is easier to diagnose eccentricity even for inverter driven cases due to their high amplitude of fault signatures with respect to the noise floor in the current spectrum. Because both static and dynamic eccentricities tend to coexist in practice, only mixed eccentricity is considered in this paper to show the effects of inverter harmonics. Magnetic field in the air gap of an eccentric motor is always non-uniform. Since the flux linkages in the air gap oscillate with synchronous frequency, any additional harmonics oscillating at the rotor speed due to non-uniform structure are expected to take place at rotating frequency sidebands of the synchronous frequency.

Static and dynamic eccentricities can be modeled in the current spectrum as:

$$f_{sidebands} = f_e\left[\left(kR \pm n_d\right)\frac{(1-s)}{p} \pm v\right] \tag{1.10}$$

where $n_d = 0$ in case of static eccentricity, and $n_d = 1,2,3..$ in case of dynamic eccentricity (n_d is known as eccentricity order), *f* is the fundamental supply frequency, *R* is the number of slots, *s* is the slip, *p* is the number of pole pairs, *k* is an integer, and *v* is the order of the stator time harmonics that are present in the power supply. However, if both static and dynamic eccentricities exist together (mixed), low frequency components near the fundamental given by [5]

$$f_1 = f_e \pm f_r \tag{1.11}$$

1.3. Research Objectives

The purpose of this research is to analyze fault signature characteristics in the current spectrum of inverter driven motors and detect these signatures using readily available hardware embedded into motor drive.

The first objective of this research is to understand the effects of inverter harmonics on motor current fault signatures. These effects are studied in detail to enhance the reliability of fault decisions by introducing the new fault signatures. It is shown that the fault signatures caused by the inverter harmonics are similar and comparable to those generated by the fundamental harmonic on the line current, according to the same physical phenomenon. The new findings are mathematically modeled and the derivation of these models is given in chapter II.

In the literature, a lot of effective fault diagnosis methods are proposed, however implementation of these solutions in real time is mostly impractical using industrial microprocessors. Therefore very simple novel schemes are should be proposed for real time applications. Existing products in the market are expensive and quite prone to negative effects of harsh environment for continuous condition monitoring. Instead, simple, low cost, robust and physically small solutions constitute a significant need in the market today. Therefore, in this dissertation a digital signal processing based, drive embedded solution is focused on to overcome aforementioned problems. The proposed method use reference frame theory to detect the fault harmonics in real time using the core processor and sensors of motor drive. Consequently, a no cost, fast, robust solution is implemented as explained in chapter III.

One of the most challenging problems of inverter driven motor line current analysis is reported as noise. In general the amplitude of fault signals is very small; hence they can easily be masked by the noise modulated on the line current. In order to reduce the negative effects of noise, a simple fault detection algorithm solution is proposed that run at an operating point where the noise impact on signature detection is minimum.

It is very important for any vehicle to monitor its vital equipments continuously. Therefore, nowadays almost all vehicles are equipped with on-board diagnosis (OBD) system. This system has been used for warnings and monitoring critical failures in the vehicle such as ignition, battery, oil and gasoline level, engine, brakes, etc. Hybrid electric vehicles (HEV) have taken their place in the market today. One of the most critical parts of HEV can be considered as electric motor which is mainly responsible from traction and propulsion. Therefore, the condition of electric motor should also be tracked on board the vehicle. However, the operating point of the electric motor integrated to an HEV continuously changes causing non-stationary current. Second, mechanical vibrations due to road vehicle interaction have enormous disadvantage on fault analysis. Thus, the best alternative is condition monitoring of electric motor at idle mode or start up. A rotor asymmetry of an asynchronous motor case is studied at standstill that can easily be adapted to HEV on board diagnosis technology.

1.4. Conclusion

In this chapter, a summary of the induction machine faults and their diagnostic methods have been presented. The research objectives and outcomes as outlined are discussed in the new few chapters.

.

CHAPTER II

LOW ORDER PWM INVERTER HARMONICS CONTRIBUTION TO THE INVERTER FED INDUCTION MOTOR FAULT DIAGNOSIS

2.1. Introduction

In this chapter, the effects of inverter harmonics on motor current fault signatures are studied in detail to enhance the reliability of fault decisions by introducing the new fault signatures. It is shown that the fault signatures caused by the inverter harmonics are similar and comparable to those generated by the fundamental harmonic on the line current, according to the same physical phenomenon.

Unlike utility-driven motor monitoring the current of inverter fed motor speed control systems is quite noisy which can mask the fault signatures and cause a wrong fault warning. Therefore, the proposed additional fault data is expected to contribute to the inverter fed motor fault decision making algorithms positively.

During the experiments, the new fault signatures due to harmonics are investigated for bearing raceway defect, eccentricity and rotor asymmetry cases. It is confirmed that the extended bearing fault, eccentricity and broken rotor bar relations given in this paper including the effects of electrical harmonic terms match with the experimental results. Furthermore, it is observed and reported that the asymmetries on the rotor caused by broken rotor bar boost the even harmonics. These harmonics are assumed to be zero in symmetric systems or low if there is physical imperfections in the machine structure. Thus, even harmonics also provide robust indications about the asymmetries (due to manufacturing errors, broken or high impedance rotor bar, etc.) which support the model and parameter estimation based broken rotor bar detections to distinguish homogeneous impedance increase due to temperature effects. In order to confirm these claims, bearing fault, eccentricity and broken rotor bar faults are tested and the line current spectrum of each faulty motor is compared with a healthy one.

Even though numerous successful line driven motor fault detection methods are reported in the literature, inverter fed driven motor systems still require more attention due to high speed switching noise effects on the line current data and closed loop controller bandwidths [31, 32]. Different from the motor line current fed directly from utility, the inverted fed motor line current includes remarkable EMI noise that adversely affects the fault diagnosis due to inherent floor noise which reduces the possibility of true fault pattern recognition using line current spectrum. Therefore, one should take into consideration as much fault signatures as possible to enhance the reliability of fault diagnosis.

It is well known that adjustable speed motor drives generate sharp-edged waveforms at the output voltage, which cause of time harmonics. In this work, it is shown that the resultant low order harmonics contribute to the fault diagnosis by repeating the same physical interaction between excitation and machine structure consecutively like fundamental harmonic. Thus, the harmonic contents, which are normally known as a major side effect of inverter, give rise to extra signatures and turn out to be useful in distinguishing faulty current spectrum patterns from healthy ones.

Although the bearing faults are the most commonly reported type with an occurrence of 40%, the diagnosis of these faults are the most challenging even under line driven motor case when compared to the other faults, because of the low amplitude fault signatures in the current spectrum. However, bearing fault detection of induction motor fed by inverters has not been investigated in the literature adequately and there are limited resources on the diagnosis and side effects of current spectrum floor noise that mask small fault related signals. In this work, in addition to well-known harmonics due to bearing failures, new bearing fault signatures excited by low order inverter harmonics are investigated theoretically and experimentally for inverter driven motors to enhance the overall fault information clarity. Similarly, it is reported that eccentricity and broken rotor bar faults introduce extra signatures on the line current by interaction of inverter harmonics and modified machine structure which provide useful data for fault detection algorithms.

The aim of this chapter is to develop a theoretical approach and present experimental verifications for bearing faults, eccentricity and asymmetry faults including low order inverter harmonics and their positive effects for diagnosis purposes. In addition, generalized theoretical fault relationships that are supported by experimental results for each fault will be presented. Finally, it is claimed and experimentally confirmed that the rotor asymmetry give rise to even harmonics of the line current spectrum as new fault signatures.

2.2. Accelerometer Outputs and Signatures Due to Fundamental Harmonic

Detection of bearing fault using accelerometer output is more expensive but relatively easier than stator current data analysis. In Fig. 2.1, accelerometer results of bearing (RU6206) outer race defect are given for two different fault levels. It is obvious that the outer race defect signals are located exactly at the multiples of fundamental mechanical vibration frequency, f_o= 107.9 Hz. The amplitude of the fault signal increases relatively with the severity of mechanical fault; therefore, one can easily monitor the condition of bearing and classify the fault level by analyzing the vibration spectra. In addition to characteristic vibration frequencies, the mean and rms of the vibration signal boost up according to the severity of fault. The mean of accelerometer output increases from -38 db to -32 db due to the introduced severe fault as shown in Fig. 2.1(b).

The stator current analysis can be realized with readily available current sensors integrated into inverters without using expensive external sensors. The main disadvantage of current spectrum analysis is the noise that causes uncertainty while separating the healthy bearing pattern from the defected. In particular, fast switching devices in the inverters generate sharp-edged waveforms with high frequency components that generate significant noise content in the motor current and hence increase noise floor in current spectrum as shown in Fig. 2.2.

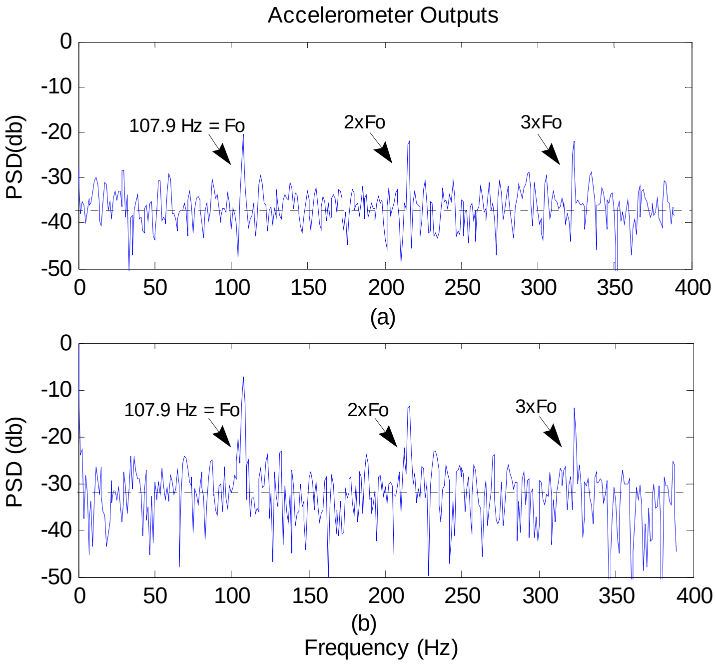

Fig. 2.1. Mechanical vibration spectrum of motor with outer race defected bearing. Top to bottom: (a) tolerable fault, (b) severe fault.

Although the inverter-fed motor stator and rotor faults have been analyzed and the initial results are given in the literature [33, 35, 36-39], they still require further investigation especially for bearing fault. When focused on bearing faults during the project, it is reported that the floor noise level is comparable with bearing fault signature amplitude, hence making it very hard to diagnose incipient bearing defects in early stages. When compared to the line driven motor test results, the test results of V/f control captured from the same test setup under the same conditions still look promising despite the higher inverter current spectrum noise floor. Further experimental analysis showed that, unlike V/f control, closed loop field oriented control (FOC) current regulators and high stator current spectrum floor noise mask the small bearing fault signatures.

Apparently, observing the bearing fault of motor driven by field oriented controlled ac drive, sensing either voltage or current is not enough without certain changes on FOC structure.

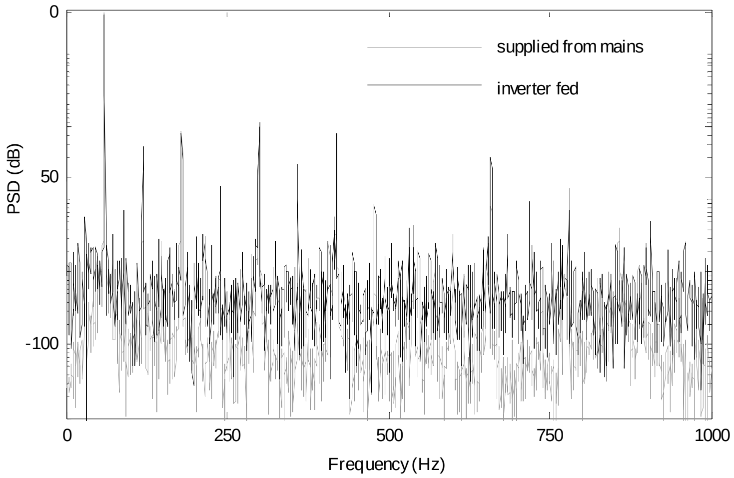

Fig. 2.2. Comparison of typical motor line current noise content for inverter-fed and utlity-fed supplies.

In Fig. 2.3., a 3-hp induction motor phase current spectrums with healthy and outer race defected bearings are given. The mechanical characteristic vibration frequency of bearing is approximately 108 Hz and the inverter frequency is set to 59 Hz. The experimentally obtained fault signatures due to fundamental harmonic on the current spectrum are shown in Figs. 2.3.(a) through (e) at the calculated fault signature frequencies according to the relationship given by (2.5). One should notice that the current spectrum figures are not normalized and the peak of the fundamental harmonic is about -10 db. Even though the amplitude of the harmonic associated with faults are small in Figs. 2.3.(a) through (e), unlike FOC driven case, they can be distinguished from noise floor. It is clear from the given test results that the online diagnosis accuracy of inverter driven motor bearing faults need further useful fault data due to inherent switching noise and EMI which are introduced in the next section.

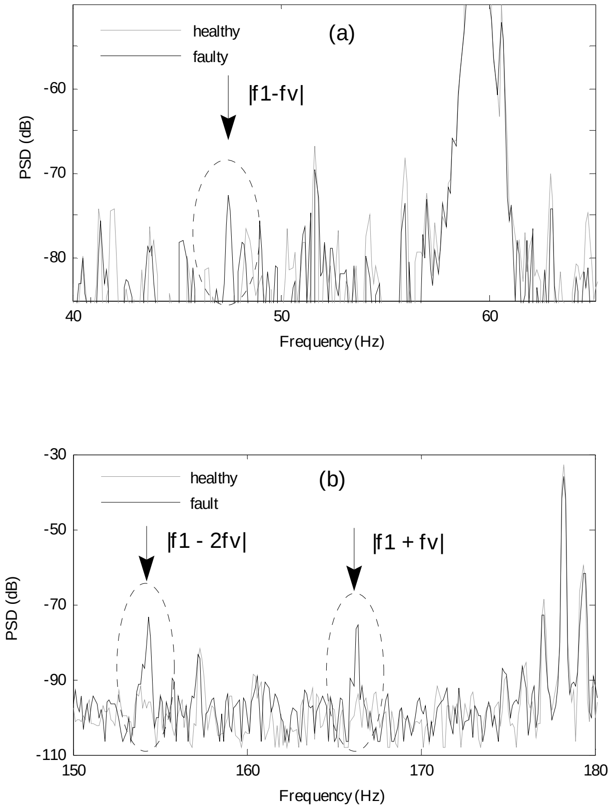

Fig. 2.3. Current spectrum of inverter fed induction motor with healthy and outer race defected bearing (for f_1=59 Hz).

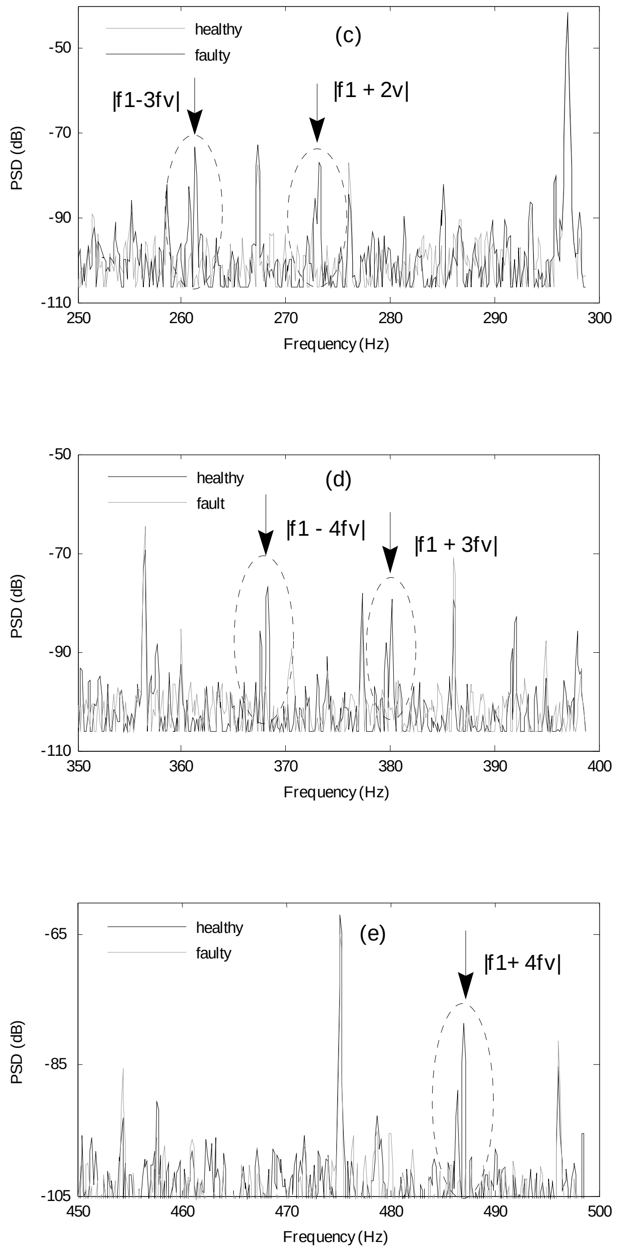

Fig. 2.3. Continued.

2.3. Theoretical Approach to Determine Bearing Fault Signatures

The main difference between the dynamic eccentricity and bearing fault is the characteristic of the mechanical oscillation characteristic. Regardless of rotor position, an eccentric rotor causes a non-uniform sinusoidal air-gap. However, bearing raceway and ball defects cause an instantaneous mechanical impulse in the air-gap [37]. For instance, in case of outer race defect a rolling element pass over the defect and generate a force vector periodically. What is measured with the accelerometer is the response of motor to this radial force. Assuming the outer race is stationary, the mechanical impulse train can be represented by

$$x(t) = a\sum_{z=-\infty}^{\infty}\delta(t - Tz) \tag{2.1}$$

where $\delta(t)$ is continuous time impulse, T is the period of impulse train, and a is the amplitude of periodic impulse train. These mechanical vibrations directly affect the permeance of the air-gap and give rise to current harmonics associated with vibration frequency. If the permeance oscillates at frequency f_{osc} and the excitation frequency is f_1, then the current will be modulated with harmonics at frequency $f_1 \pm f_{osc}$. References [38, 39] physically show the current harmonic frequencies due to the permeance variations for a small level of rotor eccentricity describing the air-gap length as

$$g(\varphi) = g_0 - \rho . g_0 . \cos(\varphi) \tag{2.2}$$

Fourier series expansion of permeance variation due to static eccentricity is

$$P_g \approx P_0 + \sum_n P_n \cos(n\varphi + \phi_n) \approx P_0 + P' \cos(\varphi) \tag{2.3}$$

The air-gap in case of dynamic eccentricity is given by

$$g(\varphi, \theta_r) = g_0 - \rho . g_0 . \cos(\varphi - \theta_r) \tag{2.4}$$

and the Fourier series expansion of permeance variation due to dynamic eccentricity is represented by

$$\begin{aligned} P_g &\approx P_0 + \sum_n P_n \cos(n(\varphi - \theta_r) + \phi_n) \\ &\approx P_0 + P'' \cos(\varphi - \theta_r) \end{aligned} \tag{2.5}$$

where ρ is the degree of eccentricity, $\rho \in (0,1)$, θ_r is the angular position of the rotor with respect to some stator reference and g_0 is the radial air-gap length in the case of a uniform air-gap, φ is the particular angular position along the stator inner surface, P_0 is the average air-gap permeance and ϕ is the phase delay. However, in case of bearing fault an exact eccentricity does not occur. Instead of continually rotating off-centered rotor, instant mechanical replacements of the rotor occur when the balls pass over the defect points. This situation can be generalized as vibrations causing permeance variation that is a complex sum of an infinite number of rotating eccentricities [7]. Thus, the air-gap should be rewritten taking these instant eccentricities into consideration

$$g(\varphi, w_{bf}, t) \approx g_0 - \sum_k \rho . g_0 . \cos(\varphi - w_{bfk} t) \tag{2.6}$$

and the Fourier series expansion permeance variation due to bearing fault vibration is

$$\begin{aligned} P_g(\varphi,\theta) &\approx P_0 + \sum_k \sum_n P_{n,k} \cos(n\varphi - w_{bfk}t - \phi_{n,k}) \\ &\approx P_0 + \sum_k P_k \cos(\varphi - w_{bfk}t) \end{aligned} \tag{2.7}$$

where w_{bfk} is the frequency of k^{th} vibration due to bearing defect. MMFs due to stator current can be shown by

$$F_1 = A\cos(p_m\varphi \pm wt) \tag{2.8}$$

where $p_m = mp$; m is the number of harmonic, w is the excitation frequency. The stator air-gap field, interaction of bearing fault with stator MMFs with respect to the stator can be expressed as: See equation (2.9) at the bottom of the page. When the frequency of the k^{th} mechanical vibration and inverter harmonics taken into consideration the above equation can be rewritten as: See equation (2.10) at the bottom of the page, where i represent the i^{th} inverter harmonic. It is clear from (2.10) that the bearing fault vibrations interacts with the inverter harmonics and generate stator current sidebands at frequencies corresponding to $(w_{bfk} \pm w_i)$.

$$\begin{aligned} B_s(\varphi,t) &= AP_0\cos(p_m\varphi \pm wt)\ldots \\ &+ \sum_k \frac{AP_k}{2}\left[\cos\big((p_m+1)\varphi - (w_{bfk} \pm w)t\big) + \cos\big((p_m-1)\varphi + (w_{bfk} \pm w)t\big)\right] \end{aligned} \tag{2.9}$$

$$\begin{aligned} B_s(\varphi,t) &= \sum_i AP_0\cos(p_m\varphi \pm w_i t)\ldots \\ &+ \sum_k \sum_i \frac{AP_k}{2}\left[\cos\big((p_m+1)\varphi - (w_{bfk} \pm w_i)t\big) + \cos\big((p_m-1)\varphi + (w_{bfk} \pm w_i)t\big)\right] \end{aligned} \tag{2.10}$$

Further experimental studies to confirm (2.10) and the explanations given above proved that the frequencies of these current fault signatures can be expressed as the extension of general bearing fault in (1.6) given by

$$f_{cf} = \left| kf_1 \pm mf_v \right| \tag{2.11}$$

where k is an integer. The associated frequencies where extra fault signatures expected due to inverter harmonics are given in Table 2.1.

Table. 2.1. Current spectrum fault signature frequencies due to the inverter harmonics (for f_1 = 60 Hz)

	m=1	*m=1*	*m=2*	*m=2*	*m=3*	*m=3*	*m=4*	*m=4*	*m=5*	*m=5*
k=1	168	48	276	156	384	264	372	492	480	600
k=3	288	72	396	36	504	144	252	612	360	720
k=5	408	192	516	84	624	24	132	732	240	840
k=6	468	252	576	144	684	36	72	792	180	900
k=7	528	312	636	204	744	96	12	852	120	960
k=12	828	612	936	504	1044	396	288	1152	180	1260

Beside the given mathematical explanations, the physical phenomenon reflected in the line current due to inverter driven motor with bearing fault can be briefly summed up using the well known stationary reference frame equations given by (2.12) and (2.13).

$$\begin{aligned} v_{qs}^{s} &= r_s i_{qs}^{s} + \frac{d}{dt}\lambda_{qs}^{s} \\ v_{ds}^{s} &= r_s i_{ds}^{s} + \frac{d}{dt}\lambda_{ds}^{s} \end{aligned} \tag{2.12}$$

If the voltage drops on the stator resistor are neglected, it can be clearly seen from the above equations that the flux linkages oscillate at the frequency of fundamental component and harmonics of the inverter. The stator flux linkages can be expressed in terms of self and mutual inductances of the machine as

$$\begin{aligned} \lambda_{qs}^{s} &= L_s i_{qs}^{s} + L_m i_{qr}^{s} \\ \lambda_{ds}^{s} &= L_s i_{ds}^{s} + L_m i_{dr}^{s} \end{aligned} \tag{2.13}$$

where

v^{s}_{dqs} – dq-axis stator voltages in stationary reference frame;
i^{s}_{dqs} – dq-axis stator currents in stationary reference frame;
i^{s}_{dqr} – dq-axis rotor currents in stationary reference frame;
λ^{s}_{dqs} – dq-axis stator flux linkages in stationary reference frame;
L_s, L_m – stator self inductance and magnetizing inductance.

Since the machine inductances are functions of the flux, the fault harmonics produced in the air-gap by the bearing defects are reflected as fault harmonics in the self and the mutual inductance of the machine. Since the flux linkages oscillate at the frequency of fundamental component and harmonics of inverter, it is clear from the above equations that any fault harmonics in the inductances at bearing fault characteristic frequencies result in current harmonics at sidebands of the fundamental and each inverter harmonic frequency as explained in the previous part.

2.4. Experimental Verifications of Fault Signatures Due to Inverter Harmonics

As explained in the previous section, the consecutive permeance variations in the air-gap due to mechanical vibrations caused by raceway defect reflect their effects on the line current under the excitation of each inverter harmonics similar to the fundamental harmonic. The experimental results in Fig. 2.4 show the new fault signatures at some of the frequencies given in Table I. Some of these signatures that are given rise by inverter harmonics are comparable with the previously defined bearing fault signatures as shown in Fig. 2.3 and are given by (1.6). Thus, one can use these extra fault indicators reliably to reinforce the fault claim. The source of the inverter harmonics and associated signatures are roughly given below.

The well-known inverter harmonics, $6k\pm1$ (i.e. 5, 7, 11, 13...) odd harmonic pairs, are the most common low order harmonics on the voltage spectrum as mentioned in the literature abundantly [40, 41]. These odd harmonics generate new fault signatures in the current spectrum at frequencies such as f =12 Hz, 192 Hz, 228 Hz etc. A similar result is mentioned in [33] where motors are driven with six-step converter and $6k\pm1$ harmonics reported to be dominant when compared to others.

Besides the odd harmonic pairs some of the remarkable signatures other than the fundamental are observed due to multiples of third and sixth harmonics commonly expected according to Table 2.1 such as f = 288 Hz where (k=3,m=1; k=6,m=6; k=12,m=4), f=504 Hz where (k=3,m=3; k=6,m=7; k=12,m=2), etc. Although third harmonic is not expected in a Y-connected system, during the experiments remarkable third harmonic is noticed as a result of non-ideal machine conditions and imperfections even for healthy machine. The sources of third harmonic and multiples are basically dc bus voltage utilization maximization of SVPWM strategy, saturation of iron core, and winding harmonic effects. On the other hand, it is known that dead-time effect, non idealities and PWM zero state space phasor also give rise to multiples of sixth harmonics [42-44]. In two-level three-phase PWM strategies, six voltage states and two zero states phasors where all phase legs switched to the same states are used. Generally, zero state phasor varies six times in constant time period. Hence, the ratio of "on" and "off" states will vary six times in one period, generating sixth harmonics and their multiples of which cause new fault signatures at frequencies such as f = 144 Hz, 468 Hz, 504 Hz as shown in Fig. 2.4.

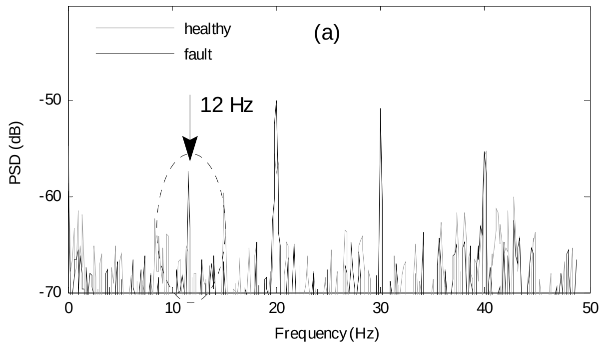

Fig. 2.4. Current spectrum of inverter fed induction motor with healthy and outer race defected bearing (for f_l= 60Hz).

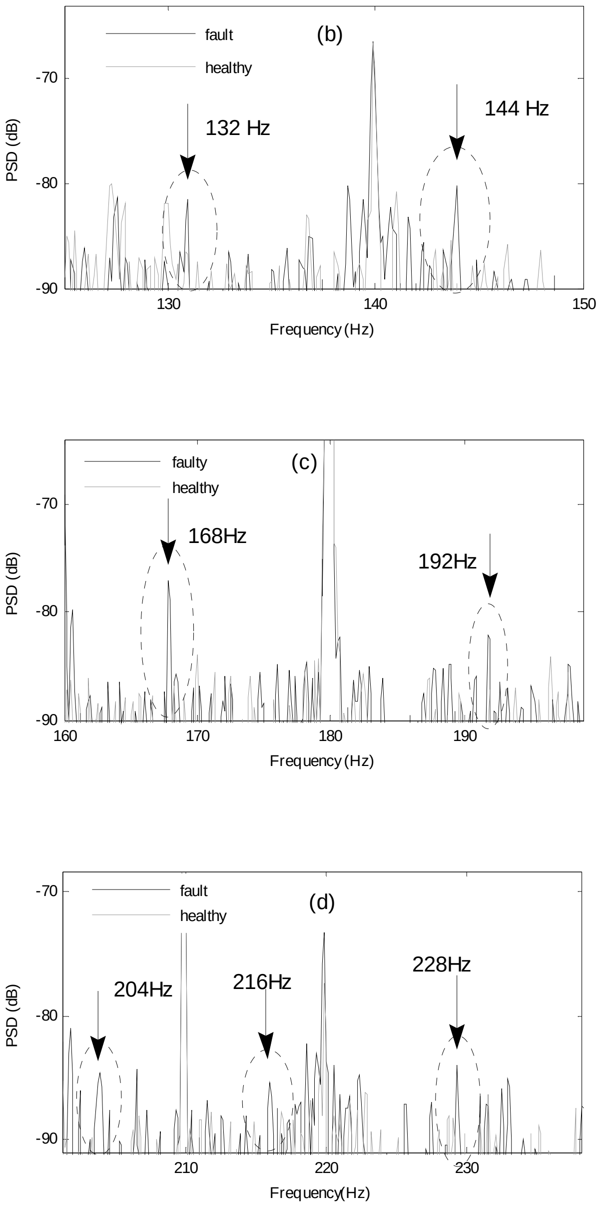

Fig. 2.4. Continued.

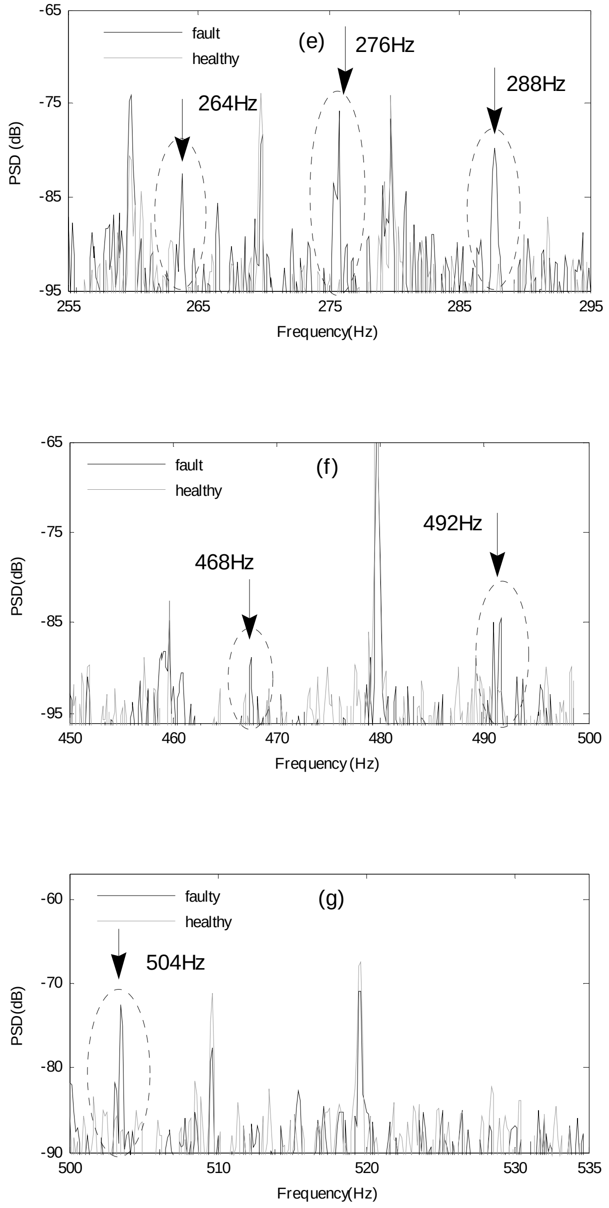

Fig. 2.4. Continued.

In order to recognize the faulty bearing pattern using the current spectrum, various methods are proposed in the literature such as: time and frequency domain techniques, high order spectral analysis, neural network, model based techniques, and statistical analysis [11, 16, 45-46]. The accuracy of these algorithms depends on the clarity and quantity of data provided. Therefore, the additional fault signatures correlated with the characteristic mechanical vibration and excitation frequencies are expected to contribute positively to bearing fault analysis.

2.5. Eccentricity Signatures in Inverter-Fed Motor Line Current Spectrum

Today, eccentricity is a quite well-known problem and analytical results supported by experiments have already been reported. In the literature, there are several successful works that report diagnosis of eccentricity based on line current measurement [4-5], [47-48] where a few of which analyze inverter-fed motor case [32]. Unlike bearing faults, it is easier to diagnose eccentricity even for inverter driven cases due to their high amplitude of fault signatures with respect to the noise floor in the current spectrum.

Because both static and dynamic eccentricities tend to co-exist in practice, only mixed eccentricity is considered in this paper to show the effects of inverter harmonics. Magnetic field in the air gap of an eccentric motor is always non-uniform. Since the flux linkages in the air gap oscillate with synchronous frequency, any additional harmonics oscillating at the rotor speed due to non-uniform structure are expected to take place at rotating frequency sidebands of the synchronous frequency. Monitoring mixed eccentricity using single-phase line current can be computed using (2.3), (2.5) and (2.8) by Nandi [4].

$$\begin{aligned} B_s(\varphi,t) &= AP_0\cos(p_m\varphi \pm wt) \\ &+\frac{AP_1}{2}\left[\cos\left((p_m+1)\varphi \pm wt\right)+\cos\left((p_m-1)\varphi \pm wt\right)\right] \\ &+\frac{AP_2}{2}\left[\cos\left((p_m+1)\varphi-(w_r\pm w)t\right)+\cos\left((p_m-1)\varphi+(w_r\pm w)t\right)\right] \end{aligned} \tag{2.14}$$

The sidebands of the excitation frequency is given as

$$\begin{aligned} f_{eccentricity} &= f_1\left[1\pm m\left(\frac{1-s}{p/2}\right)\right] \qquad m=1,\,2,\,3\,\ldots \\ &= f_1 \pm m.f_r \end{aligned} \tag{2.15}$$

where m is an integer, s is the per unit slip, f_1 is the fundamental excitation frequency, f_r is the mechanical rotation frequency, and p is the number of the poles. When the inverter harmonics taken into consideration and substituted with the excitation frequency in (2.8), then (2.15) can be rewritten as

$$\begin{aligned} B_s(\varphi,t) &= \sum_i AP_0\cos(p_m\varphi \pm w_i t) \\ &+\sum_i\frac{AP_1}{2}\left[\cos\left((p_m+1)\varphi \pm w_i t\right)+\cos\left((p_m-1)\varphi \pm w_i t\right)\right] \\ &+\sum_i\frac{AP_2}{2}\left[\cos\left((p_m+1)\varphi-(w_r\pm w_i)t\right)+\cos\left((p_m-1)\varphi+(w_r\pm w_i)t\right)\right] \end{aligned} \tag{2.16}$$

where i represent the i^{th} inverter harmonic. It is clear from (2.16) that the eccentric air-gap excited by the inverter harmonics result in stator current sidebands at frequencies corresponding to $(w_r \pm w_i)$. When the effects of the inverter harmonics are taken into consideration, (2.15) above can be rewritten as

$$f_{eccentricity} = k.f_1 \pm m.f_r \tag{2.17}$$

where k is an integer representing inverter harmonics and f_r is the rotating frequency. These fault signatures due to the inverter harmonics given by (2.17) are observed during the experiments as shown in Fig. 2.5. Although not all the introduced signatures by inverter are as noticeable as the sidebands of the fundamental, they can be used as extra fault information to support the fault decision making algorithms.

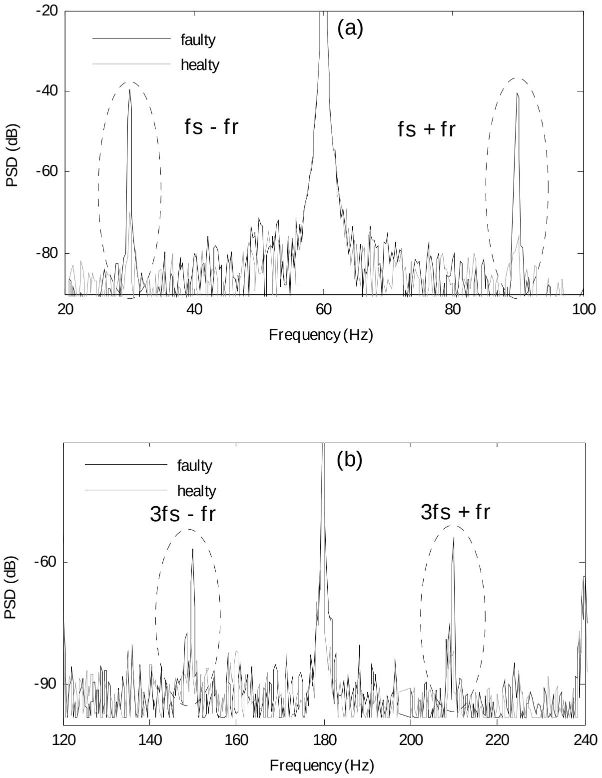

Fig. 2.5 Current spectrum of inverter fed healthy and eccentric induction motor (for f_1=60 Hz).

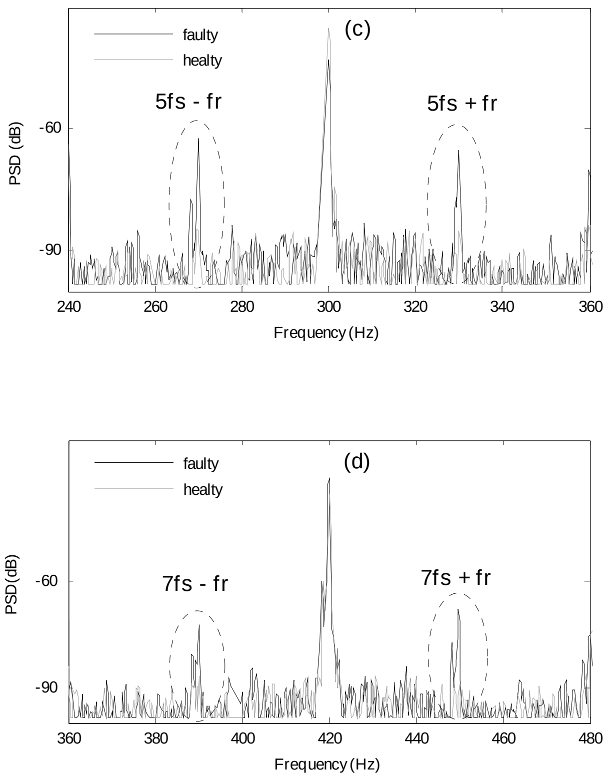

Fig. 2.5 Continued.

2.6. Rotor Asymmetry Signatures in Inverter-Fed Motor Line Current Spectrum

The electric and magnetic asymmetries in induction machine rotors boost up the left hand side sideband of excitation frequency [49]. A broken rotor bar can be considered as rotor asymmetry [49, 50] that cause unbalanced currents, torque pulsation and decreased average torque [51]. One of the significant challenges in the rotor broken bar detection is to distinguish the nearby sidebands especially under low slip operation. In this section a new signature is proposed to support the cage fault information provided by sidebands to enhance the reliability of the fault decision.

It is obvious that even number harmonics can be detected by a lack of symmetry about the x-axis. If the top and bottom half of the waveforms do not look like mirror images of each other, the even harmonics are present. Therefore even harmonic coefficients in the Fourier series expansion of symmetrical systems are always zero. A typical induction motor stator and rotor are designed to be mechanically and electrically symmetric except tolerable manufacturing imperfections. Therefore, only inherent even harmonics due to stator and rotor can be observed on the current spectrum of an inverter fed healthy machine. When the inverter harmonic content is considered, the quarter-wave symmetry assumption guarantees that the even harmonics will be zero. If the quarter-wave symmetry constraint is relaxed to a half-wave symmetry constraint, then the even harmonics are still zero [52, 53]. When a rotor bar is broken the MMF waveform cannot stay symmetric with respect to the *x*-axis due to the asymmetric bar current distribution as shown in Fig. 2.6. Eventually, this phenomenon reacts to the terminal quantities of stator.

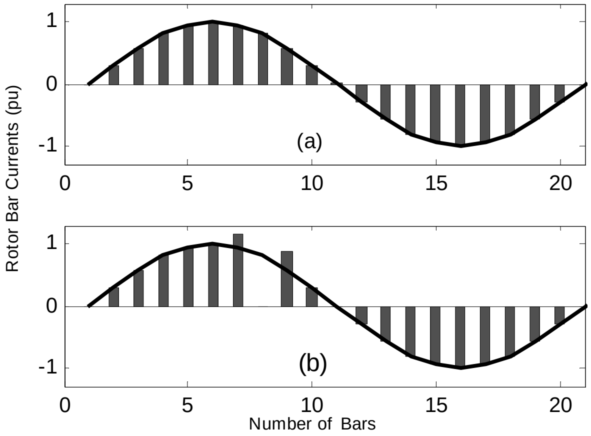

Fig. 2.6 (a) Symmetric and (b) asymmetric bar current distributions with respect to the x-axis.

During the experiments it is recorded that the inherent even harmonics boost up remarkably as shown in Fig. 2.7 when the healthy rotor is replaced with the broken bar rotor. Since symmetric SVPWM references are characterized by modulated pulses which are centered with respect to each PWM period, the observed even harmonics are introduced by asymmetry formed on the rotor. In both healthy and broken rotor bar cases, the same stator used and the rest of the system run under exactly the same conditions to make precise comparison. Hence, the amplified even harmonics are additional signatures for the rotor asymmetry which are easily noticeable fault signature components supporting broken bar fault detection technique. Even harmonics can also be used to support model and parameter estimation-based broken rotor bar diagnosis to distinguish parameter variations either because of fault or evenly distributed temperature increase.

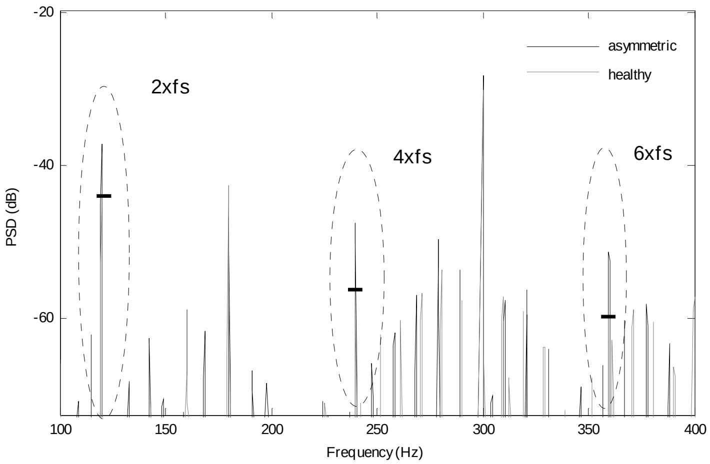

Fig. 2.7 Increase in 2nd, 4th and 6th harmonics due to rotor asymmetry.

Furthermore, other widely used approaches for diagnosis of broken rotor bars in induction machines are based on the monitoring of the stator current sidebands around the fundamental harmonic in the line current [49, 51, 54] and air-gap torque, and speed profile of induction machines [26, 55]. It is well known that any electrical or magnetic asymmetry in the rotor boosts up the left hand side and speed oscillation boosts up the right hand side sideband of the excitation frequency. Indeed, [26] shows that broken bars actually give rise to a sequence of such sidebands given by

$$f_b = (1 \pm 2k\,\mathrm{s}) f_1 \qquad k = 1,2,3... \tag{2.18}$$

where f_1 is the fundamental frequency. During regular operations, a symmetrical stator winding excited at frequency f_1 induces rotor bar currents at sf_1 frequencies. When an asymmetry is introduced in the rotor structure, backward rotating negative sequence $-sf_1$ components start chain electrical and mechanical interactions between rotor and stator of the motor. Initially, stator EMF at frequency $(1\text{-}2s)f_1$ is induced that cause torque and speed ripples. Afterwards, torque and speed ripples are reflected to the stator as line current oscillations at frequency $(1+2s)f_1$. Next, $(1+2s)f_1$ component induces rotor currents at $\pm 3sf_1$ and this chain reaction goes on until completely being filtered by the rotor inertia. When the motor is driven by PWM inverter rotor currents induced at frequency

$$f_{rotor\ current} = (6k \pm 1)|s| f_1 \qquad k = 0,1,2\ldots \tag{2.19}$$

The same chain affect mentioned above is repeated for all odd harmonic pairs due to induced rotor currents given by (2.19). In addition, each mechanical and electrical oscillations introduced by inverter harmonics will mutually interact with each other and the harmonic content of the line current is enriched by the combination of these oscillations. On the other hand, the very first impact of the fundamental harmonic on each supply harmonics is given by [1]

$$f_b = \left(\left(\frac{k}{p} \right)(1 - \mathrm{s}) \pm \mathrm{s} \right) f_1 \qquad \frac{k}{p} = 1,5,7\ldots \tag{2.20}$$

where k is harmonic index and p is the number of pole pair. However, (2.18) does not cover effects of low order inverter harmonics, and (2.20) covers asymmetrical signatures only due to the impacts of fundamental harmonic around each inverter harmonics neglecting chain reactions. Therefore, (2.18) is extended to cover odd harmonic pairs as given by

$$f_b = (m \pm 2nks) f_1 \tag{2.21}$$

k=1,2,3…,
m=1,5,7…(stator current odd harmonic pairs) ,
n=1,5,7… (induced rotor current odd harmonic pairs)

where m represents the odd inverter harmonic pairs inducing rotor bar currents and n represents the induced rotor current harmonics. Indeed, in the second term, k alone represents the effect of consecutive asymmetry signatures due to fundamental harmonic around other odd harmonic pairs. The nk term represents the odd pair multiples of fundamental harmonic including combinations of the mutual interaction between the induced backward rotating rotor currents and their consecutive reflections on the stator side around the odd harmonic pairs.

Referring to the same argument mentioned above that explains the physical facts because of asymmetry on the rotor structure, (2.20) is extended using the original index terms as

$$f_b = \left(\left(\frac{k}{p} \right) (1 - \mathrm{s}) \pm lh\mathrm{s} \right) f_1 \qquad \frac{k}{p} = 1,5,7\ldots \tag{2.22}$$

l=1,3,5…
h=1,5,7… (induced rotor current odd harmonic pairs)

where the first term transfers the induced asymmetry signatures to the stator reference frames, and the second term represent the frequency of induced rotor currents due to rotor asymmetry covering all harmonics and chain reactions. Actually, both (2.21) and (2.22), give the same asymmetry signature clusters tracing the different chain paths due to different relationship configurations and indexing. The extended equations (2.21) and (2.22) were justified experimentally using a 3-hp induction motor with broken bars driven by an inverter as shown in Fig. 2.8. The motor is driven under full load at rated speed during the experiment with s=0.05. The consecutive impacts of the rotor asymmetry around fundamental, 5th, and 7th inverter harmonics due to the induced backward rotating rotor currents can be explicitly observed in Figs. 2.8(a) and (b), respectively.

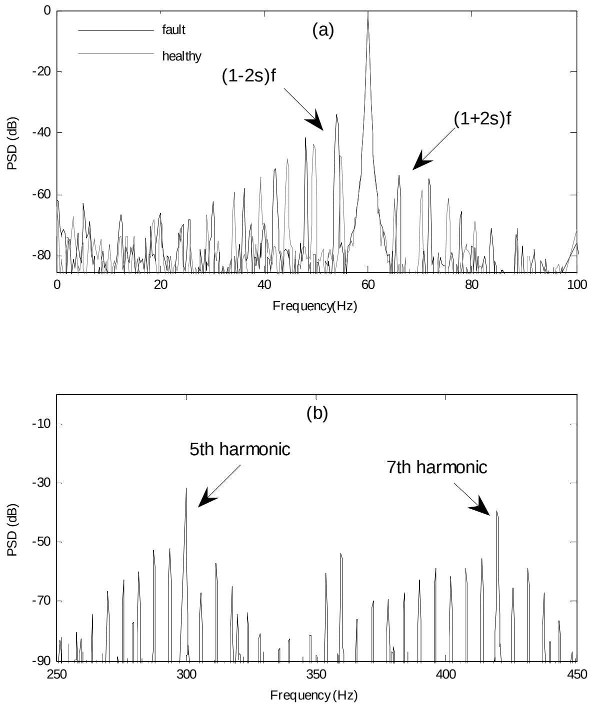

Fig. 2.8. Rotor asymmetry signatures on inverter driven motor line (a) around fundamental, (b) around 5th and 7th harmonics.

Fig. 2.8 (a) shows the sidebands of healthy motor due to the inherent asymmetry and asymmetric motor as well. Generally, the first left sideband is taken into consideration to monitor the broken rotor bar which can most easily be distinguished from healthy motor sidebands [49]. This phenomenon again repeats itself for the odd harmonic pairs. The amplitude of the first left sidebands around the odd harmonic pairs are reported to be approximately 5 dB higher than healthy motor sidebands and can be used to monitor the broken bar as additional signature.

2.7. Conclusions

The additional signatures excited by the inverter harmonics on the stator current spectrum have been analytically and experimentally analyzed in detail. It is proved that theoretically obtained bearing faults, eccentricity and broken rotor bar fault harmonic frequencies can be matched to the experimental stator current harmonics spectrum.

After explaining the challenges often encountered in fault diagnosis of adjustable speed drive systems, the analytical permeance and the field density oscillations under bearing and eccentricity faults are derived. These relationships are used to find the signatures of these faults for inverter-fed machines. The analytical results and new signatures are modeled in terms of extended fault equations covering impacts of the inverter harmonics to enrich the number of fault data. Furthermore, it is explained and experimentally shown that the rotor asymmetry gives rise to even harmonics in the line current spectrum, which can be used as signatures of asymmetrical faults. These observed even harmonics can also be employed as a useful tool to distinguish the reason behind impedance increase, which might either be broken bars or homogeneously distributed temperature effects. Extended broken rotor bar sideband relationship also shows the asymmetrical signature around low order inverter harmonics and proposes the very first left hand side sideband as the broken rotor bar fault signature.

The developed equations will also be tested on field oriented controlled systems with certain changes on closed loop structure to decline the fault signature suppression. The precise positive effects of the proposed signatures will also be examined using various pattern recognition algorithms.

CHAPTER III

A SIMPLE REAL-TIME FAULT SIGNATURE MONITORING TOOL FOR LOW-COST MOTOR DRIVE EMBEDDED DIAGNOSIS SYSTEMS

3.1. Introduction

The topic of phase transformations and reference frame theory constitutes an essential aspect of machine analysis and control. In this project, apart from the conventional applications, it is reported that the reference frame theory can also be successfully applied to fault diagnosis of electric machinery systems as a powerful toolbox to find the magnitude and phase quantities of fault signatures. The basic idea is to convert the associated fault signature to dc quantity, followed by the computation of the signal's average in the new reference frame to filter out the rest of the signal harmonics, i.e. its ac components. Because the rotor and stator fault signature frequencies are well-known, the proposed method focuses only on the fault signatures in the current spectrum depending on the examined motor fault. Broken rotor bar and eccentricity faults are experimentally tested both offline, using data acquisition system, and online, employing the TMS320F2812 DSP to prove the effectiveness of the proposed tool.

In this chapter, it is theoretically and experimentally shown that the proposed method detects the fault harmonics to determine the existence and the severity of machine faults. The advantages of this method include the following: 1- there is no need to employ external hardware or a PC running a high level program; 2- the method provides instantaneous fault monitoring using a DSP controller in real time; 3- the method is embedded into the motor drive, thus readily available drive sensors and the core processor are used without employing additional hardware; 4- no need to store current data, thus no need for large memory size; 5- very short convergence time capability; 6- immune to non-idealities like sensors dc offsets, unbalance etc. ; 7- no need for a notch filter to filter out the fundamental harmonic; 8- steady state or stationary current signal assumptions are not necessary; 9- a familiar concept for motor control engineers; and 10- can be applied to all multi-phase and single phase motors.

3.2. Reference Frame Theory

The introduction of reference frame theory in the analysis of electrical machine systems has turned out not only to be useful in their control and analysis, but also has provided a powerful tool for condition monitoring. By judiciously choosing the reference frame, it is possible to monitor any kind of motor faults, whose effects are reflected to the line current as shown in the following section. One must note that the rotating reference frame module in the software used for fault analysis works separately and independently than the one used for motor control, which is synchronized to the fundamental harmonic vector.

3.2.1. (Fault) Harmonic Analysis of Multi-Phase Systems

The commonly used transformation is the poly-phase to orthogonal two-phase transformation. For the n-phase to two phase case it can be expressed in the arbitrary reference frame as:

$$[f_{xy}] = [T(\theta)].[f_{123....n}] \tag{3.1}$$

where

$$[T(\theta)] = \sqrt{\frac{2}{n}} \begin{bmatrix} \cos(P/2)\theta & \cos(P\theta/2-\xi) & ....\cos(P\theta/2-(n-1)\xi) \\ \sin(P/2)\theta & \sin(P\theta/2-\xi) & ....\sin(P\theta/2-(n-1)\xi \end{bmatrix} \tag{3.2}$$

The electrical angle between adjacent magnetic axes of the uniformly distributed n-phase windings is represented by ξ. The harmonic current space vector in the stationary reference frame is defined as the complex quantity:

$$\hat{i}_{h\alpha\beta}(t) = i_{h\alpha}(t) + ji_{h\beta}(t) \tag{3.3}$$

Complex current harmonic vector describes a circular trajectory in the space vector plane as shown in Fig. 3.1. Therefore, a multi-phase system in phase variables transforms to a circular locus in the equivalent two-axis representation. In Fig. 3.1, the radius of the circle around the origin is the peak magnitude of the inspected harmonic quantities, and the vector rotation frequency is equal to the angular frequency of phase harmonic quantities. Note that the drawings in Fig. 3.1 are exaggerated to explain the basic of the theory explicitly, indeed the magnitude of fundamental harmonic is several times higher than all line and fault harmonics. If the new rotating reference frame is defined where the axes are made to rotate at the same rate as the angular frequency of the inspected harmonic, a stationary current space vector results, where its orthogonal components are dc quantities. The current harmonic space vector in this new reference frame is given by

$$\hat{i}_{hdq} = i_{hd} + ji_{hq} = \hat{i}_h e^{-j\theta_h} \tag{3.4}$$

where θ_h is the phase angle between the stationary reference frame and the reference frame synchronized to (fault) harmonic vector.

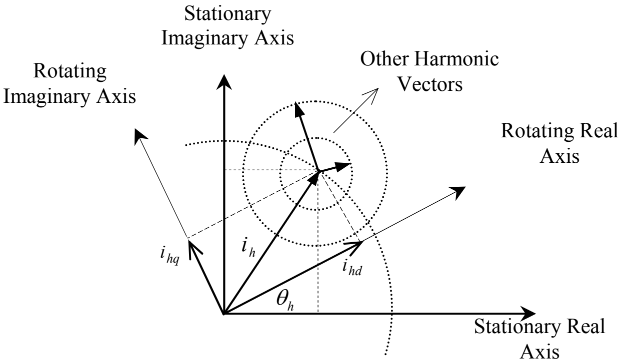

Fig. 3.1. Harmonic space vector with other harmonic vectors in the stationary and rotating reference frames.

Assuming the fault harmonic component in a 3-phase system to be a sinusoidal waveform, $i_{ha}(t) = i_{fault} \sin(\theta_{fault} - \varphi)$ and $i_{hb}(t) = i_{fault} \sin(\theta_{fault} - 2\pi/3 - \varphi)$, $\hat{i}_{h\alpha\beta}$ in (3.3) can be written in the form of $-j\left|i_{fault}\right|e^{j(\theta_{fault}-\varphi)}$ using (3.1) to (3.3) ignoring transformation constant. When this harmonic component is transformed to the reference frame at angular rotation $\theta_h = \theta_{fault}$, the harmonic vector turns out to be dc in this new frame as in the form of $\left|i_{fault}\right|e^{j(-\varphi)}$. In practice, the phase current is composed of infinite harmonic vectors besides the fault components, where $\theta_h \neq \theta_{fault}$. In the new reference frame, all harmonics other than the inspected one remain as ac. The average of these ac harmonics converge to zero and have a negligible effect on the average after a sufficient time. In other words, the reference frame synchronized with fault harmonic shifts the frequency spectrum of the phase current by frequency of the fault component. The rotating frame converts only the associated fault harmonic vector to a stationary vector at zero Hertz whose projection on orthogonal base vectors are dc and the averages are non-zero in time. Thus, when the resultant fault vector modulation is normalized with respect to the fundamental vector which is computed at synchronously rotating reference frame, the ratio gives the relative magnitude of the fault harmonic as:

$$\left|\frac{I_{fault}}{I_1}\right| = 20\log\left[\frac{\left.\left(\left(\sum_k i_{dk}\right)^2 + \left(\sum_k i_{qk}\right)^2\right)\right|_{\theta_h=\theta_{fault}}}{\left.\left(\left(\sum_k i_{dk}\right)^2 + \left(\sum_k i_{qk}\right)^2\right)\right|_{\theta_h=\theta_1}}\right]^{1/2} \text{(dB)} \qquad (3.5)$$

where i_{dk} and i_{qk} are the dq components of phase current in the rotating frame, θ_1 is the angular position of the stator reference frame, I_1 and I_{fault} are the relative magnitudes of the fundamental and fault harmonic vectors, respectively. In addition to fault harmonic magnitude calculation, the phase angle information of associated harmonic vector can also be found using the dq components obtained by the proposed technique. The dq components of the harmonic vectors decouple depending on the phase angle between rotating frame and the vector as shown in Fig. 3.1. Therefore, the phase angle is formulated as:

$$\varphi_{fault} = \tan^{-1}\left(\frac{\sum_k i_{hqk} \Big|_{\theta_h = \theta_{fault}}}{\sum_k i_{hdk} \Big|_{\theta_h = \theta_{fault}}} \right) \tag{3.6}$$

One must note that the notations, indexes and axes of the frames might change depending on how they are defined by the user. In the literature there are different representations of reference frame theory, but the basics of all are the same.

3.2.2. (Fault) Harmonic Analysis of a Single Phase

For further simplification, this method is reduced to a single phase by assuming harmonic vector as imaginary or real. The contribution of single phase analysis has lesser computational burden, greater reliability and implementation opportunity even if only one sensor reading is available. Since the fault signatures are expected to appear in all phases identically, the results are the same as multi-phase analysis case. Although the average of rotating frame d-q components will be different from the ones obtained for multi-phase, the normalized ratios remain constant. In single-phase case, various assumptions are possible for the line current reading as given in Table 3.1.

Table 3.1- Single-phase analysis, αβ –axis alternatives

$i_{h\alpha}(t) = i_{ha}(t)$ $i_{h\beta}(t) = 0$
$i_{h\alpha}(t) = 0$ $i_{h\beta}(t) = i_{ha}(t)$
$i_{h\alpha}(t) = i_{ha}(t)$ $i_{h\beta}(t) = i_{ha}(t)$

In all of the cases, the normalized harmonic magnitude and frequency content will be the same, therefore pure real or pure imaginary choices are more efficient in terms of computation time. If the fault harmonic is assumed to be $i_{ha}(t) = i_{fault}\, Cos(\theta_{fault} - \varphi)$ and $i_{h\alpha}(t) = i_{ha}(t), i_{h\beta}(t) = 0$ as in the first case of Table 3.1, then the normalized magnitude of fault harmonic is calculated with (3.5), (3.13)-(3.15). Using Euler's formula, line harmonic vector in the new reference frame synchronized with fault harmonic vector $(\theta_h = \theta_{fault})$ can be written as:

$$\begin{aligned}\hat{i}_{faultdq} &= i_{ha} . e^{-i\theta_h} \\ &= i_{fault} \cdot \left(\frac{e^{i(\theta_{fault}-\varphi)} + e^{-i(\theta_{fault}-\varphi)}}{2} \right) . e^{-i\theta_h} \\ &= i_{fault} \cdot \left(\frac{e^{-i\varphi}}{2} + \frac{e^{-i(2\theta_{fault}-\varphi)}}{2} \right)\end{aligned} \tag{3.7}$$

where $\frac{e^{-i\varphi}}{2}$ is the dc component, $\frac{e^{-i(2\theta_{fault}-\varphi)}}{2}$ is the ac component and φ is the phase angle between the rotating reference frame and the current harmonic vector. The representation of the vector components are given in Fig. 3.2.

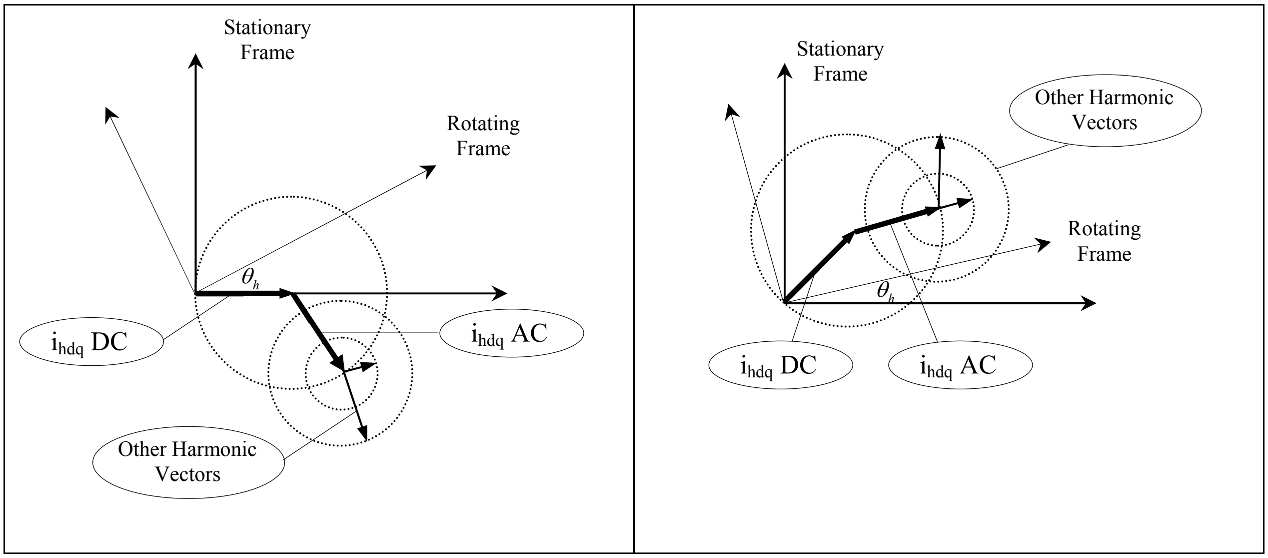

Fig. 3.2. Single-phase harmonic current vector components after transformation for two different arbitrary cases.

The average of transformed fault vector components on the rotating reference frame is calculated as:

$$\bar{i}_{fault\_d} = \frac{i_{fault}}{N}\sum_{k}^{N}\Re\left\{\frac{e^{-i\varphi}}{2}+\frac{e^{-i(2\theta_{fault}(k)-\varphi)}}{2}\right\} \rightarrow \frac{i_{fault}}{2N}\cos(\varphi) \tag{3.8}$$

$$\bar{i}_{fault\_q} = \frac{i_{fault}}{N}\sum_{k}^{N}\Im\left\{\frac{e^{-i\varphi}}{2}+\frac{e^{-i(2\theta_{fault}(k)-\varphi)}}{2}\right\} \rightarrow \frac{i_{fault}}{2N}\sin(-\varphi) \tag{3.9}$$

$$\bar{i}_{fault\_dq} \rightarrow \frac{i_{fault}}{\sqrt{2}N} \tag{3.10}$$

where N is the number of processed data. In practice, the phase current is composed of infinite harmonics including fault component as given in (3.11).

$$i_a(t) = \sum_m i_m Cos(\theta_m - \varphi_m) + i_{fault}\, Cos(\theta_{fault} - \varphi) \tag{3.11}$$

The transformed phase current in the rotating frame $(\theta_h = \theta_{fault} \neq \theta_m)$ will be:

$$\begin{aligned}\hat{i}_{dq} &= \left(\sum_m i_m.\left(\frac{e^{i(\theta_m-\varphi_m)}+e^{-i(\theta_m-\varphi_m)}}{2}\right)+i_{fault}.\left(\frac{e^{i(\theta_{fault}-\varphi)}+e^{-i(\theta_{fault}-\varphi)}}{2}\right)\right).e^{-i\theta_h}\\ &= \sum_m i_m.\left(\frac{e^{i(\theta_m-\theta_h-\varphi_m)}+e^{-i(\theta_m+\theta_h-\varphi_m)}}{2}\right)+i_{fault}.\left(\frac{e^{i(-\varphi)}+e^{-i(2\theta_{fault}-\varphi)}}{2}\right)\end{aligned} \tag{3.12}$$

The average of transformed fault vector components on the rotating reference frame is calculated as:

$$\begin{aligned}\bar{i}_d &= \frac{1}{N}\sum_k^N \Re\left\{\sum_m i_m.\left(\frac{e^{i(\theta_m(k)-\theta_h(k)-\varphi_m)}+e^{-i(\theta_m(k)+\theta_h(k)-\varphi_m)}}{2}\right)\right.\dots\\ &\left.+\,i_{fault}.\left(\frac{e^{i(-\varphi)}+e^{-i(2\theta_{fault}(k)-\varphi)}}{2}\right)\right\} \rightarrow \frac{i_{fault}}{2N}\cos(-\varphi)\end{aligned} \tag{3.13}$$

$$\begin{aligned}\bar{i}_q &= \frac{1}{N}\sum_k^N \Im\left\{\sum_m i_m.\left(\frac{e^{i(\theta_m(k)-\theta_h(k)-\varphi_m)}+e^{-i(\theta_m(k)+\theta_h(k)-\varphi_m)}}{2}\right)\right.\dots\\ &\left.+\,i_{fault}.\left(\frac{e^{i(-\varphi)}+e^{-i(2\theta_{fault}(k)-\varphi)}}{2}\right)\right\} \rightarrow \frac{i_{fault}}{2N}\sin(-\varphi)\end{aligned} \tag{3.14}$$

$$\bar{i}_{dq} \rightarrow \frac{i_{fault}}{\sqrt{2}N} \tag{3.15}$$

which gives the same results as calculated in (3.8)-(3.10).

Finally, the normalized ratio with respect to the fundamental can be calculated in a similar way given in (3.5) where the magnitude of fundamental is calculated using equations (3.8)-(3.10) in synchronously rotating frame. When the αβ-components are taken as $i_{h\alpha}(t) = i_{ha}(t)$ and $i_{h\beta}(t) = i_{ha}(t)$ then the dc components in the new frame will converge to:

$$\bar{i}_{d} \rightarrow \frac{I_h}{2N}(\cos(\varphi) + \sin(\varphi)) \tag{3.16}$$

$$\bar{i}_{q} \rightarrow \frac{I_h}{2N}(\cos(\varphi) - \sin(\varphi)) \tag{3.17}$$

where the relative ratio between the fault component and the fundamental remains the same as calculated in the previous case and multi-phase case.

Typical harmonic vector tracks after single phase transformation are shown in Fig. 3.3 where $\theta_h = \theta_1$ and signal is composed of 1.0pu 1st harmonic, 0.01pu 3rd, 5th, and 7th harmonics. It is clear that only 1st harmonic has dc offset and the rest are located around zero with zero average values. Therefore, after a few cycles the average of the transformed signal magnitude converge the dc offset and the effects of the other ac components converge the zero.

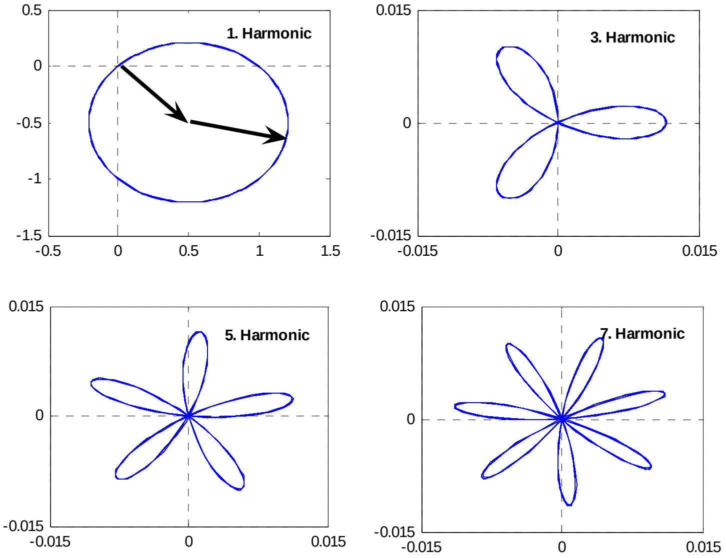

Fig. 3.3. The harmonic vector (1st, 3rd, 5th, 7th) tracks when $\theta_h=\theta_1$.

3.3. Simulation Results

The performance of reference frame theory while detecting relative amplitude of specified harmonic is tested under various conditions before focusing on the fault analysis. Initially, 60 Hz, 3-phase line currents are distorted artificially by injecting 3rd, 5th, 7th and 11th harmonics as shown in Table 3.2 and Fig. 3.4(a).

Table 3.2. Injected harmonic content

	Amplitude	Phase
1st Harmonic	1.00 pu	30°
3rd Harmonic	0.2 pu	-25°
5th Harmonic	0.1 pu	0°
7th Harmonic	0.2 pu	-45°
11th Harmonic	0.1 pu	55°

In Fig. 3.4 (b), the dq components of transformed signal are given when the reference frame is rotating at ($f=f_5$) 5^{th} harmonic frequency. The time average of dq components in Fig. 3.4 (b) are shown in Fig. 3.4 (c) which gives the dq axis components of 5^{th} harmonic on the rotating reference frame. Since the phase angle of 5^{th} harmonic is zero and the fundamental harmonic is 1.0 pu the normalized magnitude of 5^{th} harmonic is found to be $i_{5dq}=0.1$ pu as given in Table 3.2 where $i_{5d}=0.1$pu and $i_{5q}=0$ pu. It is clear that time average of 5^{th} harmonic settles down at 0.20 seconds which is short enough time for real time fault diagnosis analysis.

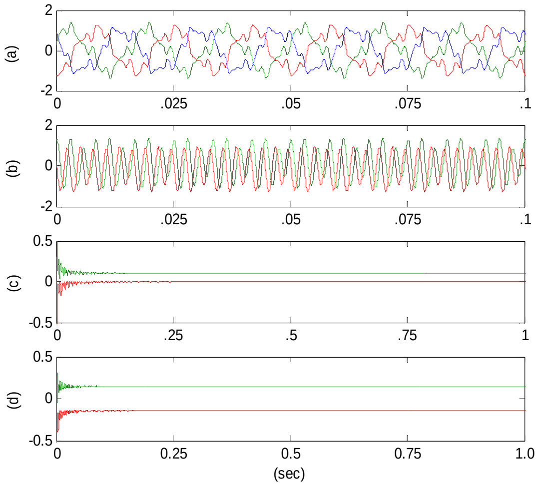

Fig. 3.4. (a) Distorted 3-phase line current by injected harmonics, (b) dq components when the frame is rotating at $f_h=f_5$, (c)time average of dq components when frame is rotating at $f=f_5$ (d) time average of dq components when frame is rotating at $f=f_7$.

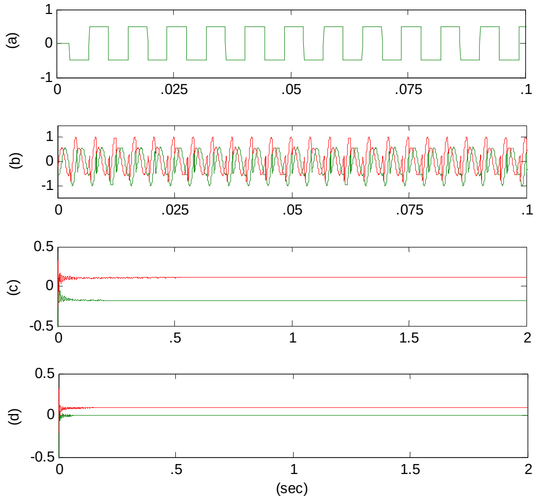

Fig.3.5. (a) 3-phase square wave including infinite harmonics, (b) dq components when the frame is rotating at $f_h=f_3$, (c) average of dq components when frame is rotating at $f=f_3$ (d) average of dq components when frame is rotating at $f=f_7$.

In Fig. 3.4 (d), the 7^{th} harmonic dq components on rotating frame is plotted when the frame frequency is $f=f_7$. Since the phase angle is -45^0, dq components are decoupled equally where $i_{7d}=i_{7q}=0.141$ pu and $i_{7dq}=0.2$ pu as expected. This simulation proves that the reference frame theory work effectively to detect normalized harmonic magnitudes and phase relations within very short convergence time. In the next section, it will also be experimentally shown that this method is very satisfactory to detect line and motor fault harmonics in the line current with high accuracy.

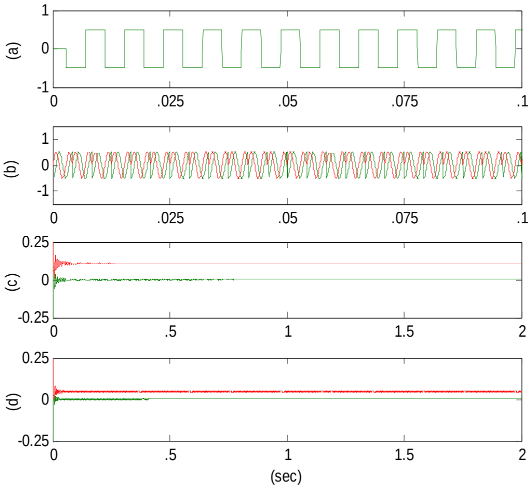

Fig. 3.6. (a) Single-phase square wave including infinite harmonics, (b) dq components when the frame is rotating at $f_h=f_3$, (c) average of dq components when frame is rotating at $f=f_3$, (d) average of dq components when frame is rotating at $f=f_7$.

Since square wave is a combination of infinite number of harmonics, a 3-phase square-wave generator is used to test the method if it can detect the required harmonics. As shown in Fig. 3.5(c) and Fig. 3.5(d), 3rd harmonic and 7th harmonic dq components are successfully extracted from the signal using rotating frames. These two simulations prove that this method works effectively to find out the normalized harmonic magnitude when the input is 3-phase. The same test is applied to single-phase case and it is noticed that it gives the same normalized magnitudes as the 3-phase tests as shown in Fig. 3.6;

however, the amplitude of each harmonic is half of the 3-phase results as expected from (3.13)-(3.14).

3.3.1. Offset Errors

There might be some cases where the motors have to run under non-ideal conditions or measurement devices function incorrectly which are highly possible especially in the harsh industrial plant environment. Here, the effects of most commonly encountered problems on proposed technique are examined. The first possible errors are the line current offset and current sensing system dc errors. As shown in (3.18)-(3.19) and Fig. 3.7, the proposed system is totally immune to offset errors both in 3-phase, Fig. 3.7 (a) and 3.7 (b), and single-phase, Fig. 3.7 (c) and 3.7 (d), harmonic analysis. Assume that phase A has an offset error, $i_{ha}(t) = i_{h\alpha}(t) = I_h \cos(\theta - \varphi) + \xi$, then in 3-phase system the current harmonic vector is written as :

$$\begin{aligned} i_{hdq} &= e^{-i\theta}(e^{i(\theta-\varphi)} + \xi.e^{i0}) \\ &= e^{i(-\varphi)} + \xi.e^{-i\theta} \end{aligned} \tag{3.18}$$

In single-phase analysis, the same current harmonic vector is represented by,

$$\begin{aligned} i_{hdq} &= e^{-i\theta}\left(\frac{e^{i(\theta-\varphi)} + e^{-i(\theta-\varphi)}}{2} + \xi.e^{i(0)}\right) \\ &= \frac{e^{i(-\varphi)}}{2} + \frac{e^{-i(2\theta-\varphi)}}{2} + \xi.e^{-i\theta} \end{aligned} \tag{3.19}$$

In both of these cases the offset components turn out to be ac and its average converges to zero after a long enough time. Therefore, the offset term does not affect harmonic analysis results obtained by the proposed method.

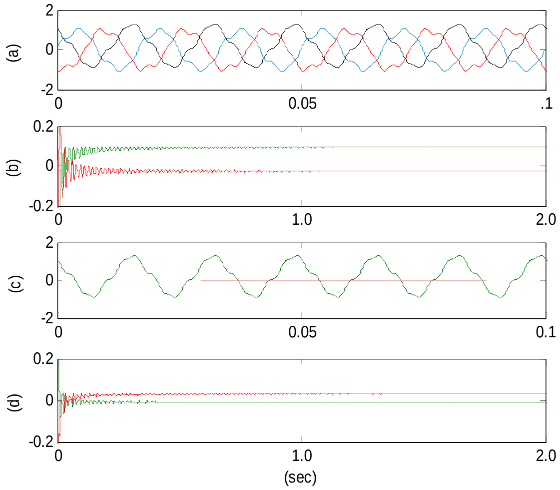

Fig. 3.7 (a) Distorted line currents, phase A has 0.2 pu offset, (b) 3rd harmonic dq components when the frame is rotating at $f_h=f_3$, (c) Distorted line current, phase A has 0.2pu offset, (d) 3rd harmonic dq components when frame is rotating at $f=f_3$.

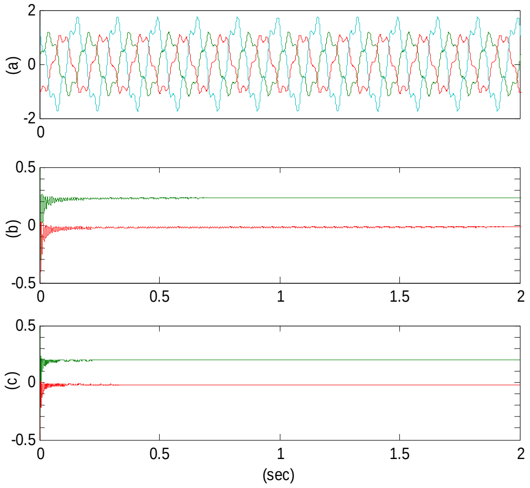

Fig. 3.8 (a) Distorted line currents, phase A has 1.5 times higher amplitude, (b) 5th harmonic dq components when the frame is rotating at $f_h=f_5$, (c) 5th harmonic dq components when frame is rotating at $f=f_5$ (normalized).

3.3.2. Unbalanced Phase Currents

It is obvious that single-phase analysis does not have an unbalance problem; thus this case is considered for 3-phase analysis. Fortunately, the proposed method is not affected when the phase amplitudes are not identical. The most common unbalanced stator conditions are unbalanced source voltages and unbalanced loads [8]. In these cases, the source voltages might be different as $e_{ga} \neq e_{gb} = e_{gc}$, $e_{ga} \neq e_{gb} \neq e_{gc}$ or the applied voltages might be different due to a series additional load as:

$$\begin{aligned} v_{as} &= e_{ga} - \frac{2}{3} i_{as} Z_s \\ v_{bs} &= e_{gb} + \frac{1}{3} i_{as} Z_s \\ v_{cs} &= e_{gc} + \frac{1}{3} i_{as} Z_s \end{aligned} \tag{3.20}$$

where v_s is the applied phase voltage and Z_s is the additional phase load that cause unbalanced load situation in a Y-connected 3-wired system. It is clear that all harmonic content will linearly change in each phase including fundamental component under above unbalanced conditions. Therefore, the resultant transformed and averaged magnitude of each harmonic is different from the balanced condition; however, normalized amplitudes remain constant for single phase and 3-phase system analysis. When the frame transformation (3.1)-(3.5) is applied to unbalanced system currents it will be seen that the averaged magnitude ratio of examined harmonic to fundamental will be the same, due to linearly superposed unbalance effect to each harmonic components. In Fig. 3.8, phase A is applied 1.5 times higher than the other phases to simulate a typical unbalanced 3-phase system. After transformation and averaging, dq components shown in Fig. 3.8 (b) are observed as i_{5d}=0.232 pu and i_{5q}=0.02 pu. These components become i_{5d}=0.199pu and i_{5q}=0.0174pu as shown in Fig. 3.8 (c) after normalization as expected where injected 5th harmonic is 0.2 pu. The simulations prove the proposed method can be applied to unbalanced systems to find normalized motor fault signatures reliably.

3.3.3. Proximity of the Harmonics

In some cases like broken bar fault analysis, fault signatures are in the very close neighborhood of fundamental harmonic or line harmonics. Therefore the resolution of the fault diagnosis tool should be very high to correctly distinguish each harmonic component. In order to test the reference frame theory, a number of harmonics are injected to the fundamental harmonic, the frequencies of which are close to each other. The simulation results prove that the proposed method is highly promising in differentiating neighboring components as shown in Table 3.3, provided that a sufficient number of data is used.

Table 3.3 Analysis of proximate harmonics

Injected Harmonic Freq.	**Injected Harmonic Amplitude**	**Normalized Component i_{hd} (pu)**	**Normalized Component i_{hq} (pu)**	**Normalized Magnitude i_{hdq} (pu)**
54 Hz	0.001 pu	-0.00070711	-0.00070711	0.001
55 Hz	0	< - 100 dB	< - 100 dB	< - 100 dB
56 Hz	0.002 pu	-0.0011756	-0.001618	0.002
57 Hz	0	< - 100 dB	< - 100 dB	< - 100 dB
58 Hz	0.04 pu	-0.02	-0.034641	0.04
59 Hz	0	< - 100 dB	< - 100 dB	< - 100 dB
60 Hz	1.0 pu	-0.86603	-0.5	1
61 Hz	0	< - 100 dB	< - 100 dB	< - 100 dB

3.3.4. Phase Delay

Phase delay between the rotating frame and inspected harmonic or other harmonic components do not degrade the results. In Table. 3.2 and Table 3.3 the line currents are composed of different harmonics at different frequencies and phase delays. In each harmonic inspection, it is reported that the phase differences of injected harmonics, including inspected ones, do not affect examined harmonic current vector dq components and noise floor.

3.3.5 Transient State Analysis

The most widely used condition monitoring methods focus on the steady-state, which assumes that the rotor speed, the fundamental stator frequency and the load are all constant. The classical applications of Fourier transform show an averaged frequency distribution, and there is no time representation. Fluctuations in the instantaneous frequency and amplitude as a result of machine operation or loading effects are averaged out. Accurate detection under transient conditions therefore cannot be easily accomplished. Since only one fault harmonic is inspected each time, low computational burden provides fast scanning opportunity which is an inevitable criterion for transient state analysis. Second, due to the readily available drive control parameters such as stator frequency and rotor speed, one can continually update the operating point dependent fault signatures frequencies and find the track of normalized magnitude during transients. In practice, the steady-state assumption in fault detection analysis is not valid for many applications where constant speed cannot always be guaranteed (e.g., in wind generation or HEV drive cycles).

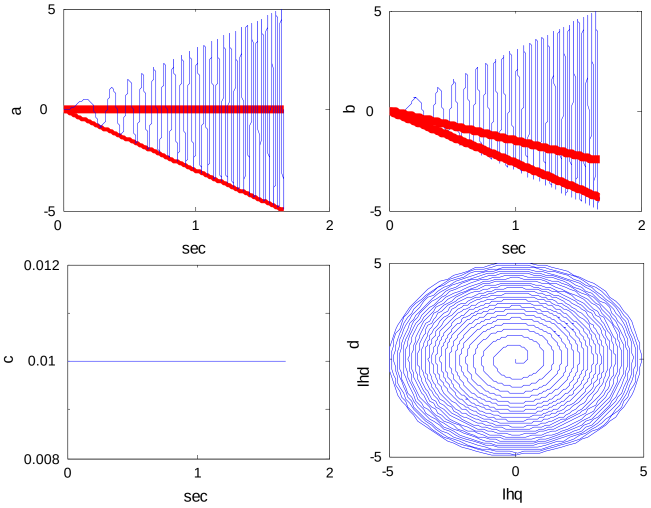

Fig. 3.9 (a) 1st harmonic and instantaneously computed dq components when phase angle is zero, (b) 1st harmonic and instantaneously computed dq components when phase angle is π/3, (c) instantaneously computed normalized 3rd harmonic magnitude, (d) i_{1hd} vs i_{1hq}.

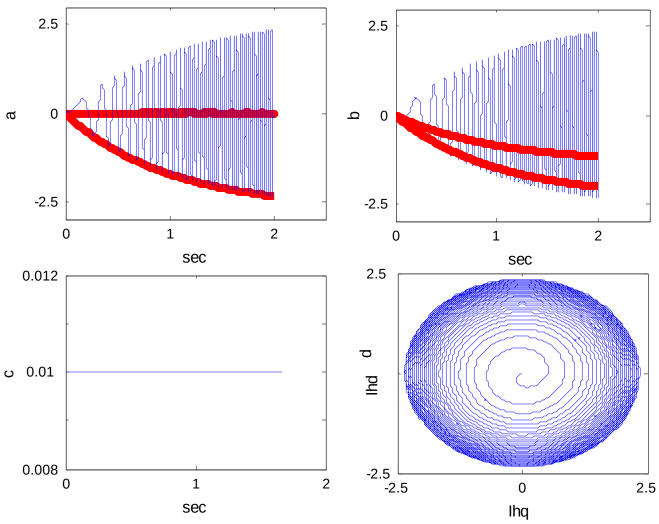

Fig. 3.10 (a) 1st harmonic and instantaneously computed dq components when phase angle is zero, (b) 1st harmonic and instantaneously computed dq components when phase angle is π/3, (c) instantaneously computed normalized 3rd harmonic magnitude, (d)i_{1hd} vs i_{1hq}.

During the transient performance test, a 0.01 pu 3rd harmonic is injected to 1.0 pu 1st harmonic. The frequencies of both 1st and 3rd harmonics increase linearly with amplitude in Fig. 3.9 and exponentially in Fig. 3.10. This proportional increase in both fundamental and harmonic currents during transient is a consistent assumption with the transient model given in [58]. As shown in Fig. 3.9 (c) and Fig. 3.10 (c) the normalized magnitude of 3rd harmonic remains constant as injected, although relative amplitude and frequencies of harmonics vary. The results of these tests confirm that the inspected harmonic can be traced by updating the reference frame angular frequency instantaneously, and this method is capable of capturing the harmonic information during transient conditions as well.

3.4. Offline Experimental Results

The performance reference frame method is experimentally verified both offline and online. In order to implement offline tests, the data acquisition system is used to obtain the motor phase currents and a Matlab-based reference frame code is run to detect broken rotor bar and eccentricity signatures in the line current spectrum. The eccentric motors are mechanically modified to form a mixed eccentricity with 5%, 20.69% DE and 41.37% SE. Broken bar rotor tests are done using 4/44 and 3/28 bars broken rotors under various load conditions at different speeds. These faults are examined while the motor is driven from utility and the inverter is controlled by both FOC and V/f algorithms. In the first experimental stage, a cluster of faulty motor line current data obtained by the data acquisition system are processed using the proposed method and the results are compared with the FFT spectrum analyzer outputs.

3.4.1. Utility Driven Motor Line Current Analysis

Initially, utility driven eccentric motor line current is analyzed using the proposed method both with 3-phase and single-phase currents. In order to detect the eccentricity fault signatures, related fault frequencies are calculated according to ($f_s \pm f_r$) and chosen to be the angular frequency of rotating frame where f_s=60 Hz and $\omega_r \approx$1795 rpm. As shown in Fig. 3.11(a) and Fig. 3.11(b) both the single phase and 3-phase harmonic analysis results are quite close to each other as expected and shown theoretically. Therefore, the rest of the experimental results will be given using single-phase harmonic analysis which is more reliable for industrial environments and cheaper

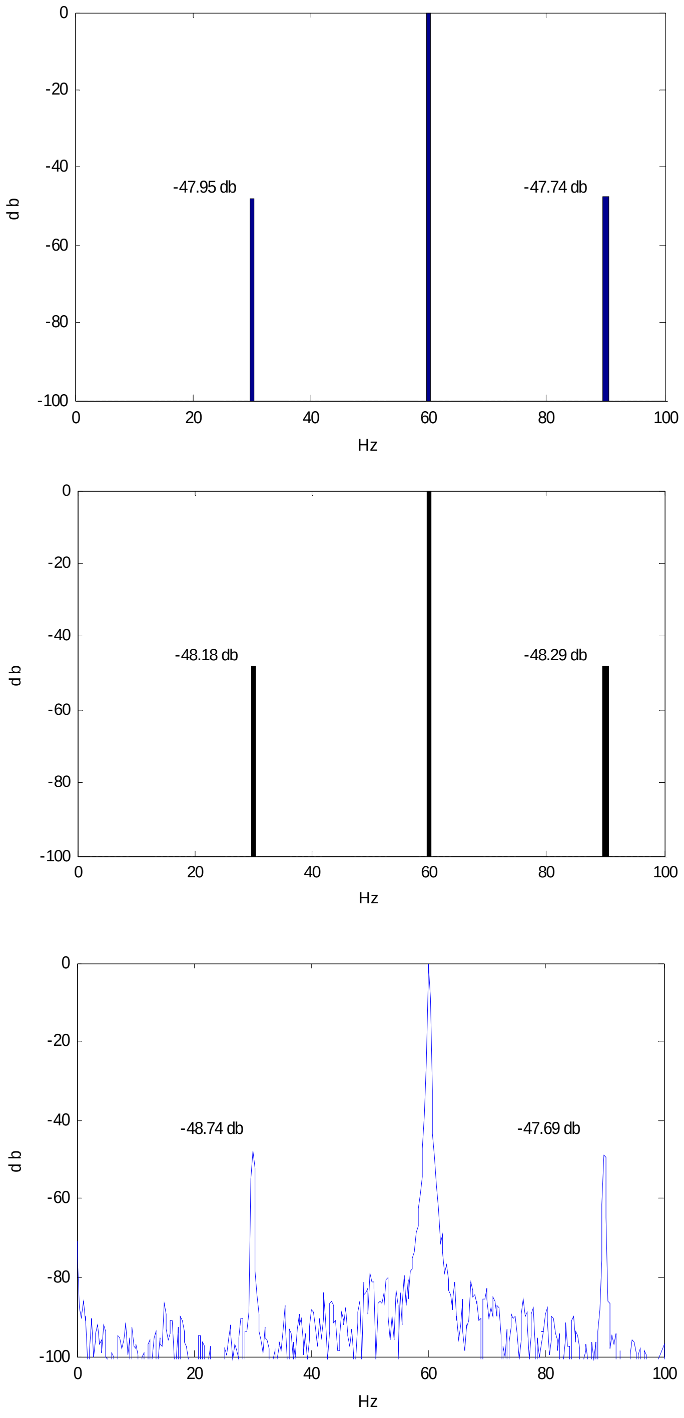

Fig. 3.11. Experimentally obtained utility driven eccentric motor line current harmonic analysis results, (a) single-phase rotating frame harmonic analysis results, (b) 3-phase rotating frame harmonic analysis results, and (c) FFT spectrum analyzer output of the line current.

to implement. In Fig. 3.11(c) line current spectrum of a utility driven induction motor is obtained by FFT spectrum analyzer. The left hand side normalized fault harmonics of single-phase and 3-phase analysis at (f_s-f_r) are found to be -47.95 dB and -48.18 dB, respectively using the proposed method. The FFT spectrum analyzer result for the same test is -48.74 dB. On the other hand, the right hand side normalized fault harmonics of single phase and 3-phase analysis at (f_s+f_r) are found to be -47.74 dB and -48.29 dB, respectively where FFT spectrum analyzer result is -47.69 dB. In brief, Fig. 3.11 experimentally proves that the difference between rotating frame harmonic analysis results and FFT spectrum analyzer results are acceptably negligible for utility driven motor case.

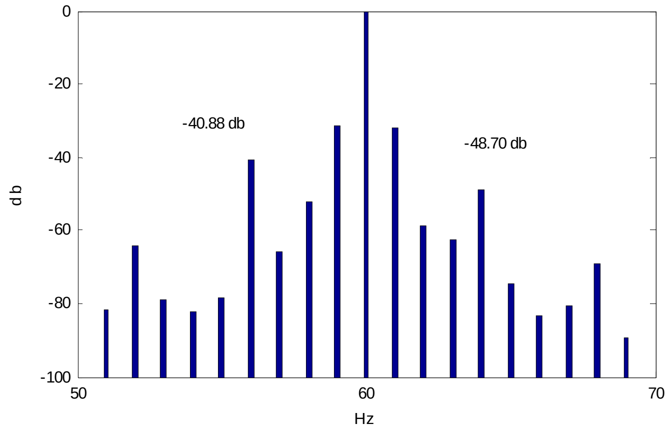

Fig. 3.12. (a) Experimentally obtained utility driven broken rotor bar motor single phase line current rotating frame harmonic analysis result, (b) FFT spectrum analyzer output of line current.

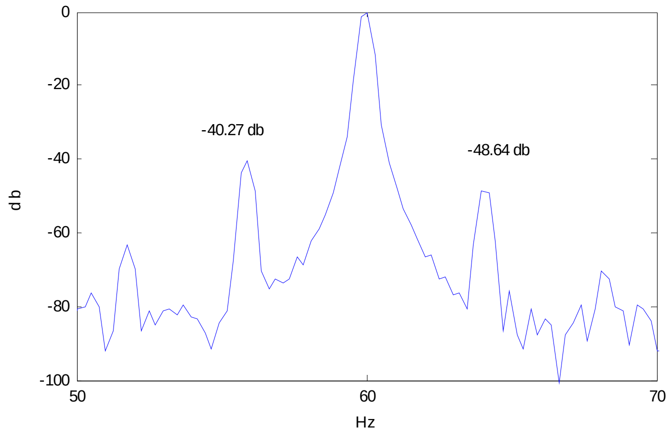

Fig. 3.12 Continued.

The broken bar test of utility driven motor is done using an induction motor with four broken bars under full load where f_s=60Hz, $\omega_r \approx$1720 rpm and fault signatures are expected at $f_s(1 \pm 2s)$ Hertz. Since the fault signatures of broken bar fault are in the neighborhood of fundamental harmonic, the normalized magnitude of current spectrum is computed in 1 Hz incremental steps to examine the resolution of the rotating frame theory. Therefore, the 1 Hz incremental steps are set as the angular frequency of the rotating frame. As shown in Fig. 3.12 (a) the harmonic magnitudes closest to the side bands are -40.88 dB and -48.70 dB. The calculated fault signature magnitudes are very close to FFT spectrum analyzer results given in Fig. 3.12 (b). In real time applications, exact excitation frequency and estimated rotor speed are used to obtain more precise results; therefore, here, the purpose of 1 Hz incremental steps in Fig. 3.12 (a) are to verify and demonstrate the performance of this method when the fault harmonics are close to fundamental or to each other.

3.4.2. V/f Controlled Inverter Driven Motor Line Current Analysis

Secondly, the eccentricity and broken bar fault signatures are examined when the motor is driven by a V/f controlled inverter. Unlike the utility driven case, the excitation frequency and rotor speed are adjustable when the motor is driven by an inverter, therefore the fault signatures dynamically change depending on the stator frequency and slip values. Since the stator frequency and slip are mostly used as control parameters in the inverter control algorithms, the fault signature frequencies can easily be updated using this information.

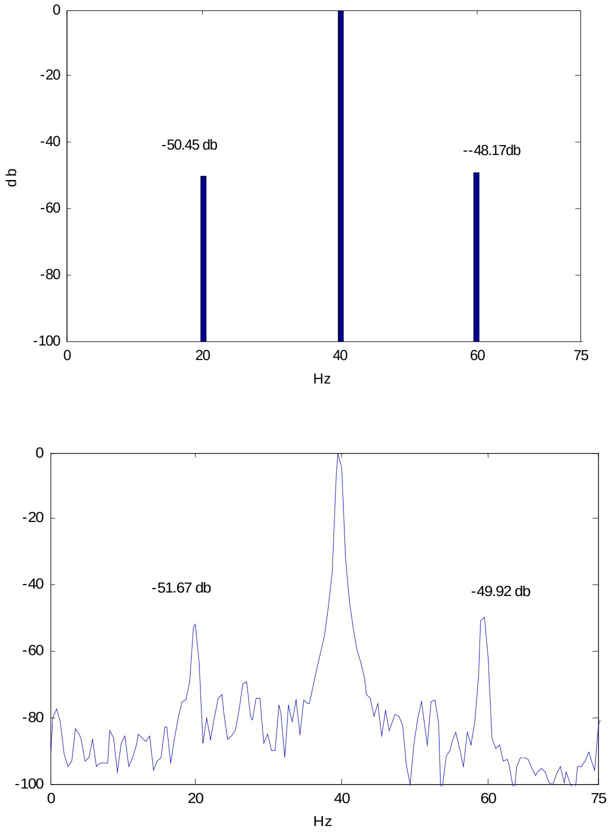

Fig. 3.13. (a) Experimentally obtained V/f controlled inverter driven eccentric motor single-phase line current rotating frame harmonic analysis result, (b) FFT spectrum analyzer output of line current.

In this step, the eccentric motor mentioned in the previous part is driven at 0.66 pu reference speed under no load where f_s=40Hz and $\omega_r\approx$1180 rpm. As shown in Fig. 3.13 (a) the left hand side normalized fault harmonics at (f_s-f_r) Hertz are found to be -50.45 dB using the single-phase harmonic analysis and the FFT spectrum analyzer result is -51.67 dB. On the other hand, the right hand side normalized fault harmonics at (f_s+f_r) Hertz are found to be -48.17 dB using the proposed method, and the FFT spectrum analyzer result is -49.92 dB.

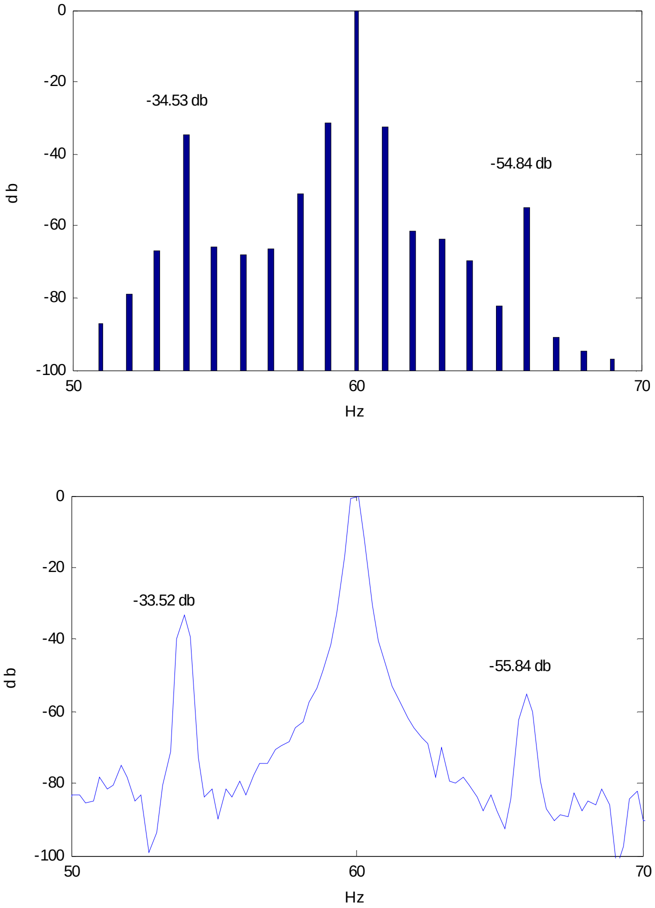

Fig. 3.14. (a) Experimentally obtained V/f controlled inverter driven broken bar motor single-phase line current rotating frame harmonic analysis result, (b) FFT spectrum analyzer output of line current.

The broken bar test of V/f controlled inverter driven motor is done using an induction motor with four broken bars under full load where f_s=60Hz, $\omega_r \approx 1745$ rpm and fault signatures are expected at $f_s(1 \pm 2s)$ Hertz. As shown in Fig. 3.14(b) the side bands of the broken bar motor current spectrum are -33.52 dB, -55.84 dB and the single-phase rotating frame results are -34.53 dB, -54.84 dB.

3.4.3. FOC Inverter Driven Motor Line Current Analysis

Finally, both the broken bar and eccentricity fault diagnosis tests are repeated when the motor is driven by FOC inverter at various speeds under various load conditions. In this project, it is reported that the most challenging fault detection is encountered when the motor is controlled by FOC. The most significant problem is higher noise floor which threatens the small fault signature detection and the other one is signature sharing between voltage and current due to the closed loop control. However, the remarkable fault signatures are not affected from the noise as shown in Fig. 3.15(b).

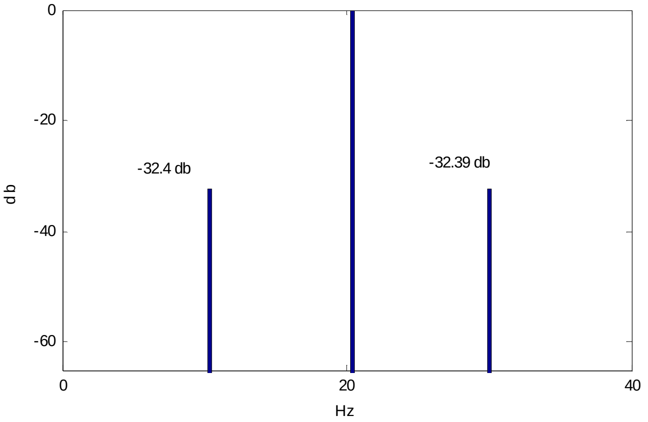

Fig.3.15 (a) Experimentally obtained FOC controlled inverter driven eccentric motor single-phase line current rotating frame harmonic analysis result, (b) FFT spectrum analyzer output of the line current.

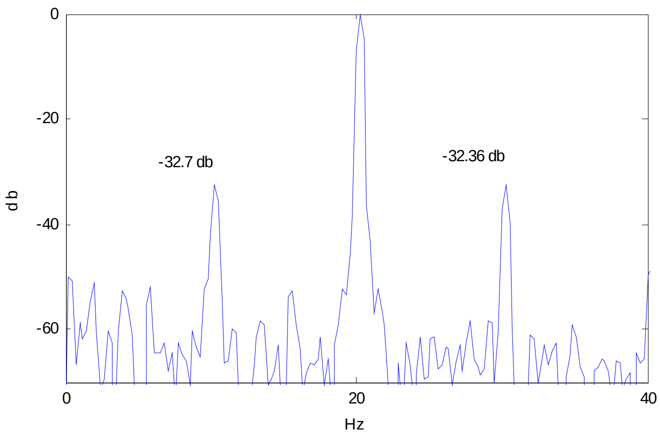

Fig.3.15 Continued.

In this test, the reference speed is 0.33 pu and the motor is run under no load. The excitation frequency is f_s=20.26 Hz and the shaft speed is $\omega_r \approx$594 rpm. The eccentricity indicator side bands are found to be -32.40 dB, -32.39 dB using the proposed method, and the observed values from FFT spectrum analyzer are -32.70 dB, -32.26 dB as shown in Fig. 3.15.

In Fig. 3.16, broken bar test results are given when the motor is run by FOC inverter under full load where the reference speed is 0.66 pu and $\omega_r \approx$1150 rpm. The normalized sidebands are computed to be -40.33 dB, -31.72 dB whereas the FFT analyzer outputs are -40.09 dB, -30.89 dB.

All of the offline experimental results above show that the proposed method works effectively to find out the fault signatures with a very high precision. Since the three-phase and single-phase analyses give almost the same results; the single phase method is mostly employed during the analysis.

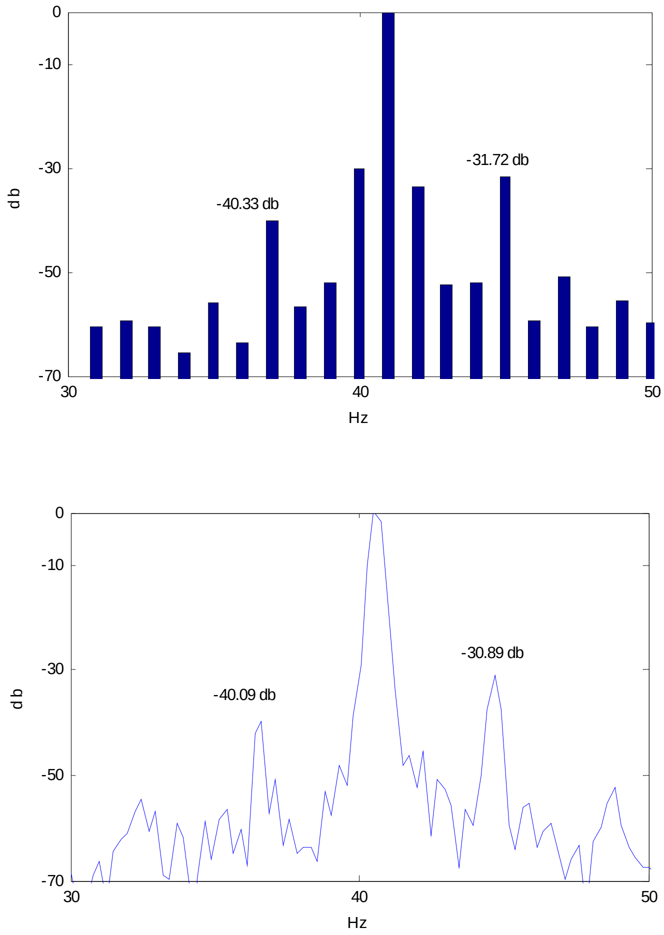

Fig. 3.16 (a) Experimentally obtained FOC controlled inverter driven broken bar motor single-phase line current rotating frame harmonic analysis result, (b) FFT spectrum analyzer output of the line current.

3.4.4. Performance Test under Non-Ideal Conditions

In the previous sections, it is theoretically proven that the offset and unbalance problems do not violate the results obtained by reference frame theory. In this section, these claims are verified experimentally. Three-phase line currents of V/f controlled motor are used to analyze the sidebands of eccentricity. One of the phase current signals is modified by simple signal conditioning to insert 0.2 pu dc offset to phase-A as shown in Fig. 3.17 (a). On the other hand, in order to obtain an unbalanced set of 3-phase currents phase-A current is multiplied by 1.5 as shown in Fig. 3.17 (b). In all ideal and non ideal cases, it is reported that the normalized left eccentricity sideband is exactly -50.04 dB and the right sideband is -48.42 dB. Both the theoretical and offline experimental tests show robustness and reliability of the proposed method even under non ideal conditions, which are run into often in harsh industrial facilities.

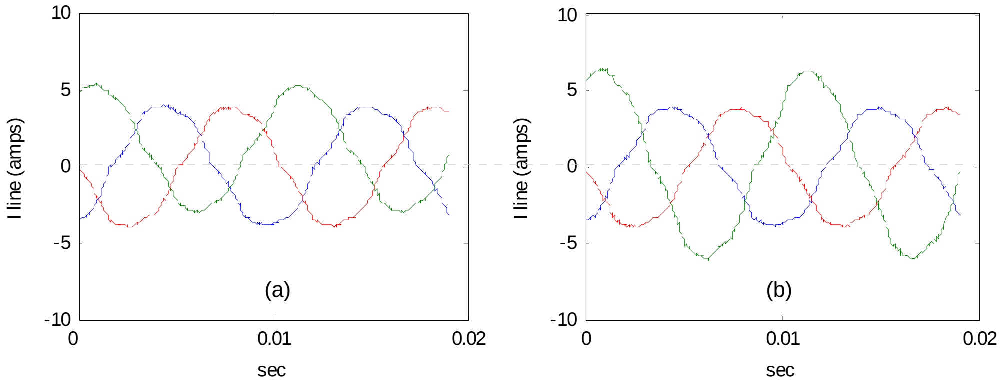

Fig. 3.17 Experimentally obtained V/f controlled inverter driven eccentric motor 3-phase line currents, (a) 0.2 pu offset added to phase-A current sensor reading, (b) Phase-A current sensor reading modified to obtain unbalanced 3-phase.

3.5. Online Fault Detection Results

Similar tests are repeated online using the TMS320F2812 DSP, which is employed both for inverter control and fault signature detection. Several experiments are realized under various conditions such as different rotor speeds, slip values, load conditions, switching frequencies, sampling frequency and the number of data processed.

When using DSP core for both control and fault purposes, the fault code is embedded into the main control algorithm as a subroutine that processes the instantaneously measured current data for both fundamental component and fault signature frequency. The same experiments are also successfully repeated for utility driven motors where the DSP is responsible only for fault analysis rather than control issues. Although undersampling and oversampling are possible, generally switching frequency is accepted to be the sampling frequency of the current data to synchronize the fault subroutine with the main control. The number of data is chosen to be the same as the sampling frequency, which can be adjusted between 4k and 20k depending on the applications. The stator frequency can either be calculated or equated to the reference value depending on the control type, and the rotor speed can either be measured using encoder or estimated to update the signature frequencies in real time. Though the DSP processor of the inverter is used in this project, the very simple algorithm of reference frame theory can be implemented using a simpler microcontroller as well.

3.5.1 V/f Controlled Inverter Driven Motor Line Current Analysis

The eccentricity and broken bar tests are repeated using TMS320F2812 DSP controlled inverter where ω_{rref} = 0.99 pu. The motor is run at no load and at full load for eccentricity tests and broken bar tests, respectively. As shown in Fig. 3.18 both the eccentricity and broken rotor bar sidebands found by DSP microprocessor are very close to ones observed by FFT spectrum analyzer at $(f_s \pm f_r)$ and $(1 \pm 2s)f_s$, respectively. The time spent to process 5k-20k data and detect these signatures is 1 sec, which is sufficiently short for fault monitoring where there is no strict time limitation. Depending on the resolution requirements and the system control parameters, execution time might be shortened or extended.

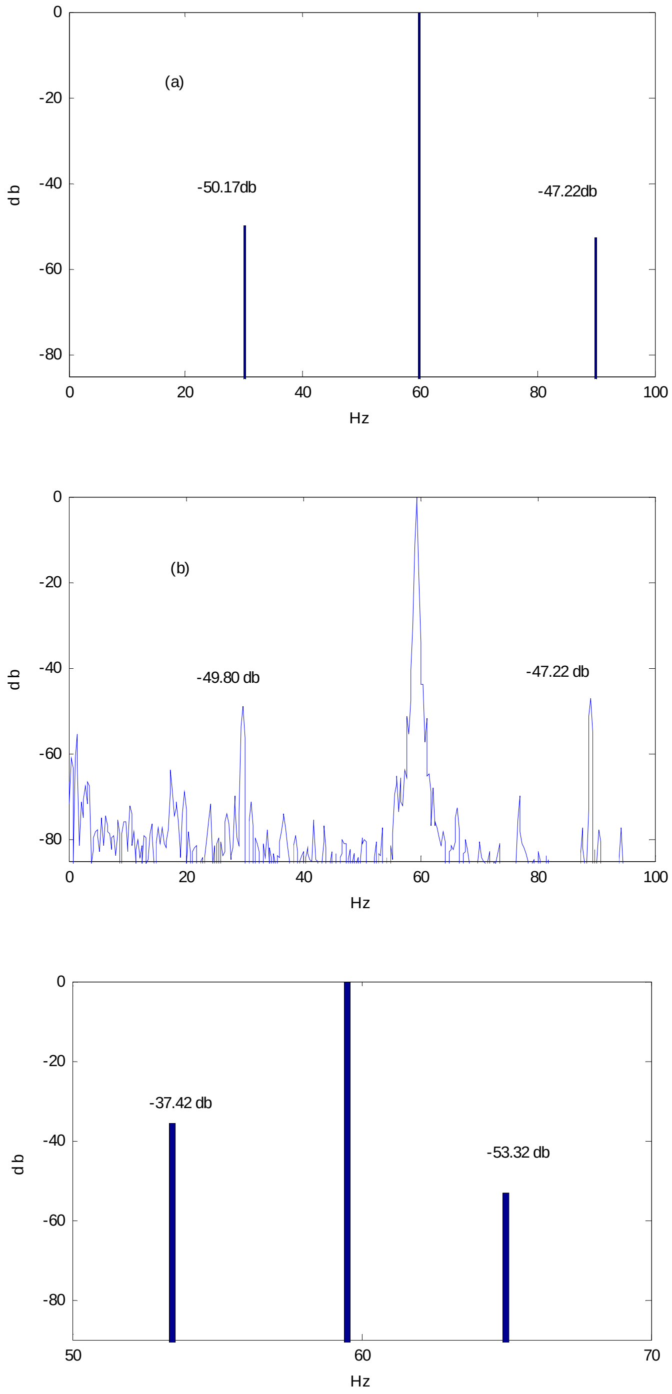

Fig. 3.18 Experimentally obtained V/f controlled inverter driven motor single phase harmonic analysis result, (a) eccentricity signatures detected by DSP using rotating frame theory, (b) FFT spectrum analyzer output of eccentric motor line current, (c) broken bar signatures detected by DSP using rotating frame theory, (d) FFT spectrum analyzer output of broken bar motor line current.

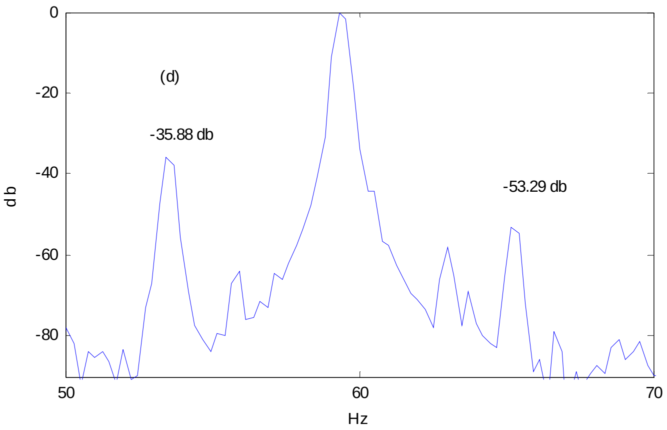

Fig. 3.18 Continued.

3.5.2. FOC Controlled Inverter Driven Motor Line Current Analysis

In Fig. 3.19, the same experiments are repeated running the motor with closed-loop field oriented control algorithm at various operating points. The results obtained by industry purpose processor and 12-bit ADCs are very close to FFT spectrum analyzer outputs which has two DSP core and 16-bit ADC with a sampling rate of 256 kHz. These online experimental results confirm that the proposed method can be adapted to the real time applications successfully.

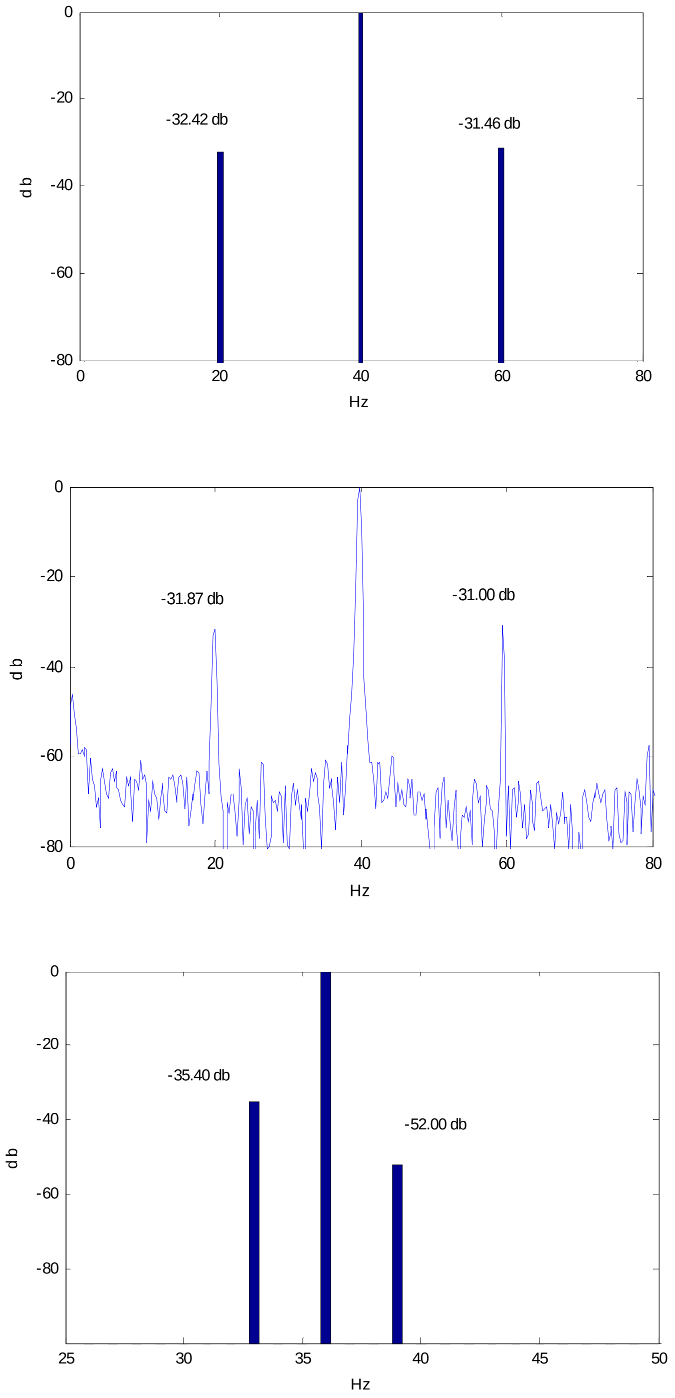

Fig. 3.19 Experimentally obtained FOC controlled inverter driven motor single phase harmonic analysis result, (a) eccentricity signatures detected by DSP using rotating frame theory, (b) FFT spectrum analyzer output of eccentric motor line current, (c) broken bar signatures detected by DSP using rotating frame theory, (d) FFT spectrum analyzer output of broken bar motor line current.

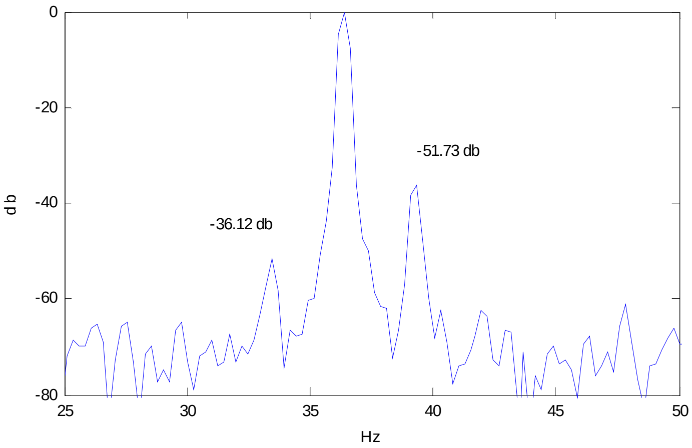

Fig. 3.19 Continued.

3.5.3. Instantaneous Fault Monitoring in Time-Frequency Domain and Transient Analysis

A stationary motor line current signal repeats into infinity with the same periodicity. However, this assumption is not realistic for most of the industrial applications where duty cycle profile of the motor cannot be guaranteed to operate at steady state and single operating point. Instead, duty cycle involves various operating points at different load and speed combinations for an unknown time period.

On the other hand, the motor current spectrum analyses done using Fourier transform assumes that the current signal is stationary. The Fourier transform performs poorly when this is not the case. Furthermore, the Fourier transform gives the frequency information of the signal, but it does not tell us when in time these frequency components exist. The information provided by the integral corresponds to all time instances because the integration is done for all time intervals. It means that no matter where in time the frequency appears, it will affect the result of the integration equally.

This is why traditional application of Fourier transform is not suitable for non-stationary signals.

As stated earlier, continuous stator frequency and shaft speed information are available and are used to update fault signature frequencies at all operating points. The updated fault signature frequency is utilized to synchronize the reference frame and associated fault vector component of the line current. Therefore, even the motor excitation frequency or rotor shaft speed change due to acceleration, deceleration, loading, etc. the normalized fault signature magnitude is instantaneously and continuously monitored without using additional algorithms. In brief, this advantage provides real time tracing of fault signature components in the frequency domain. In Fig. 3.20 (a) and Fig. 3.20 (b), the right eccentricity sideband magnitude and rotor speed are shown, respectively. The dynamic characteristics of right eccentricity sideband at transients and different rotor speeds are traced experimentally by DSP processor in real time as shown in Fig. 3.20 (a). A similar test is done under load when the motor is driven by V/f open loop control at 0.4 pu speed as shown in Fig. 3.20 (c) and Fig. 3.20 (d). In Fig. 3.20 (c), the eccentricity right sideband track in real time is shown when the motor is loaded while running at no-load and in Fig. 3.20 (d) the phase-A current vector magnitude is shown to identify the load characteristics.

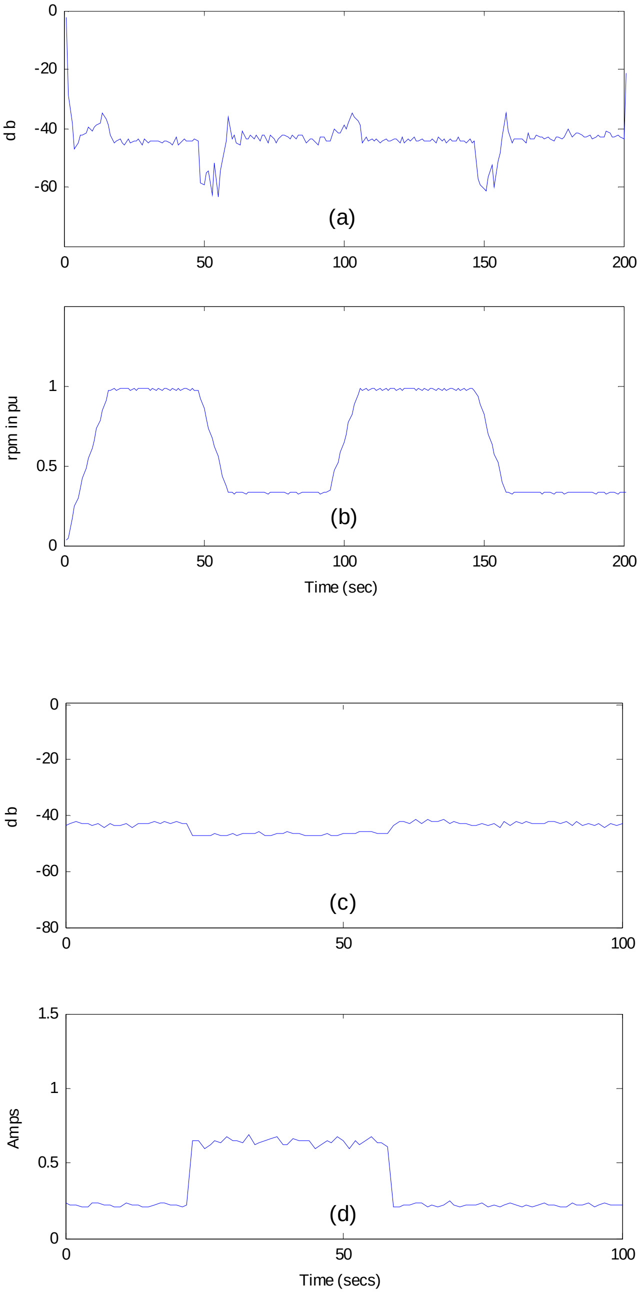

Fig. 3.20 Experimentally obtained V/f controlled inverter driven motor single phase harmonic analysis result (a) normalized eccentricity sideband variation detected by DSP using rotating frame theory, (b) motor speed in pu, (c) normalized eccentricity sideband variation detected by DSP using rotating frame theory, (d) motor line current in Amps.

3.6. Conclusions

This paper has presented the experimental and the analytical validation of the reference frame theory application to electrical motor fault diagnosis. The proposed method has many advantages over existing fault diagnosis methods using external hardware and powerful software tools. The experimental test results are compared with FFT spectrum analyzer results to confirm the accuracy of this method. It is experimentally shown that this simple diagnosis algorithm can be embedded in the main control subroutine and run by the motor drive processor in real time without affecting control performance of the inverter. Therefore, it can even be considered as a no cost application, which is highly promising for future fault diagnosis products.

CHAPTER IV

PHASE SENSITIVE DETECTION OF MOTOR FAULT SIGNATURES IN THE PRESENCE OF NOISE

4.1. Introduction

In this chapter, digital signal processor (DSP)-based phase-sensitive motor fault signature detection is presented. The implemented method has a powerful line current noise suppression capability while detecting the fault signatures. Because the line current of inverter driven motors involve low order harmonics, high frequency switching disturbances, and the noise generated by harsh industrial environment; the real-time fault analyses yield erroneous or fluctuating fault signatures. This situation becomes a significant problem when signal to noise ratio (SNR) of the fault signature is quite low. It is theoretically and experimentally shown that the proposed method can determine the normalized magnitude and phase information of the fault signatures even in the presence of noise, where the noise amplitude is several times higher than the signal itself.

4.2. Digital Signal Processing in Fault Diagnostics

Although a great many studies have been done on motor fault analysis, drive embedded real time fault analyzers have not taken their place in the market. The main features expected from such a product are: low cost, noise immunity, and simple algorithms that might be realized in real time on the existing motor drive processor.

Now that digital signal processing (DSP) technology is being applied to motor drive control, the improved benefits of this processing unit are being realized in more applications than ever before such as fault detection. The proposed fault detection method is implemented using the inverter existing processor; therefore it does not produce any extra computing cost. Control and protection purpose current sensors installed in the motor drive provide line current information for real time analysis. Therefore, no specialized hardware is required to realize phase sensitive fault detection. Furthermore, the most complicated mathematical tool used in the simple detection algorithm is the basic trigonometric functions that can be handled either with look-up tables or numeric functions. The overall execution time of the fault detection algorithm takes a few seconds to obtain high enough resolution.

A typical normalized fault signature is within the range of -40 dB to -80 dB; hence fault detection is quite prone to the negative effects of noise content in the current spectrum. Therefore, noise suppression is a significant requirement for small signature detection, which is achieved by a phase sensitive lock-in algorithm in the present work. This method simply locks to and measures the particular frequency of interest, ignoring all other signals at the input. The eliminated signals might either be at the same frequency with different phase angle or at some other frequencies. Fortunately, phase sensitive fault detection provides a technique for rejecting both ac and dc noise sources while the signal is measured. When the floor noise is high, the inspected small signatures will mostly be comparable with the noise content including the components at the same frequency. A lock-in detector is capable of measuring small ac signals that are obscured by large amounts of noise. In fact, ac signals can be extracted even when dominated by far greater noise.

The lock-in detector is a phase sensitive demodulator that examines how two entities are related. It is generally used to determine the presence of a periodic signal that has been buried under noise. The lock-in detector demodulates the frequency of interest. Its output is a function of the relative phase angle between the input signal and the associated reference signal generated by the processor. Therefore, the lock-in detector is used to measure both the relative phase and normalized magnitude of the fault signatures.

One of the most commonly used magnitude measurement techniques is the fast Fourier transform (FFT) method [1-4]. The main duty of the FFT-radix algorithms is to reduce the complexity by decomposing the discrete Fourier transforms (DFTs) into smaller DFTs in a recursive manner [9-10,59]. In order to compute the DFT of discritized signals, all signal data should be stored and indexed. Moreover, to obtain high resolution and accurate results in inverter driven systems, a large number of data points should be buffered due to low signal frequency and high switching frequency constraints. Therefore, implementing FFT algorithms in real time using low-cost industrial processors is a challenge. Consequently, the proposed method is an excellent alternative to the problems addressed above for magnitude detection particularly in noisy environment.

4.3. Phase Sensitive Detection

Phase sensitive detection is based on correlation of two signals. In the correlation process, the input signal is compared with a reference signal and similarity between these signals is determined [9-10, 59]. Given two real valued sequences *x(n)* and *y(n)* of finite energy, the cross-correlation of *x(n)* and *y(n)* is a sequence $r_{xy}(\ell)$ defined by,

$$r_{xy}(\ell) = \lim_{k\to\infty} \frac{1}{2N} \sum_{N=-k}^{N=k} x(n)y(n-\ell) \tag{4.1}$$

where ℓ is called the shift or lag parameter. The special case of (4.1) when *x(n)=y(n)* is called the auto-correlation. It provides a measure of self-similarity between different alignments of the signals and is given by,

$$r_{xx}(\ell) = \lim_{k\to\infty} \frac{1}{2N} \sum_{N=-k}^{N=k} x(n)x(n-\ell) \tag{4.2}$$

Similarly, a lock-in detector takes a periodic reference signal and a noisy input signal, and then extracts only that part of the output signal whose frequency and phase match the reference. To see how the phase sensitive detector works, consider a reference signal, I_{ref}, which is a pure sine wave with frequency of w_{ref},

$$I_{ref}(t) = I_{ref}\cos(w_{ref}t + \varphi_{ref}) \tag{4.3}$$

and the noisy fault signal,

$$I_{in}(t) = I_{fault}\cos(w_{fault}t + \varphi_{fault}) + \sum I_{noise}\cos(w_{noise}t + \varphi_{noise}) \tag{4.4}$$

The correlation between these two signals is given by,

$$\begin{aligned}
I_{II}(\varphi) &= I_{ref}\cos(w_{ref}t+\varphi_{ref})I_{fault}\cos(w_{fault}t+\varphi_{fault}) \\
&\quad + I_{ref}\cos(w_{ref}t+\varphi_{ref})\sum I_{noise}\cos(w_{noise}t+\varphi_{noise}) \\
&= I_{ref}I_{fault}\cos(w_{ref}t-w_{fault}t+\varphi_{ref}-\varphi_{fault}) \\
&\quad + I_{ref}I_{fault}(w_{ref}t+w_{fault}t+\varphi_{ref}+\varphi_{fault}) \\
&\quad + I_{ref}I_{noise}\sum\cos(w_{ref}t-w_{noise}t+\varphi_{ref}-\varphi_{noise}) \\
&\quad + \cos(w_{ref}t+w_{noise}t+\varphi_{ref}+\varphi_{noise})
\end{aligned} \tag{4.5}$$

The generated reference signal frequency is set to be the same as the fault signal frequency; therefore some of the terms in (4.5) are converted to dc as given by (4.6).

$$\begin{aligned}
I_{II}(\varphi) &= I_{ref}I_{fault}\cos(\varphi_{ref}-\varphi_{fault}) + I_{ref}I_{fault}(2w_{ref}t+\varphi_{ref}+\varphi_{fault}) \\
&\quad + I_{ref}I_{noise}\sum\cos(w_{ref}t-w_{noise}t+\varphi_{ref}-\varphi_{noise}) \\
&\quad + \cos(w_{ref}t+w_{noise}t+\varphi_{ref}+\varphi_{noise})
\end{aligned} \tag{4.6}$$

If the auto-correlation output is low pass filtered simply by averaging, only two terms survive, the dc term due to the output of the system, and the noise component with frequency near the reference signal. The rest of the noise and low order harmonics disappear as shown in (4.7).

$$I_{II\_filtered}(\varphi) \approx K_1 \cos(\varphi_{ref} - \varphi_{fault}) + K_2 \sum \cos(\varphi_{ref} - \varphi_{noise}) \tag{4.7}$$

The phase of the noise signal varies randomly. In order to minimize the effects of noise content at the same frequency, the phase angle difference between the reference signal and the fault signals should be minimized. There are some alternatives to maximize the low pass filtered portion of the auto-correlation function. One alternative is to track the auto-correlation function and detect the peak point where the phase angles of the reference signal and the fault signal are the same. The second and more efficient method is examining both the correlation of cosinusoidal and sinusoidal reference signals to the same phase angle instantaneously. The arctangent of the correlation ratio results the phase angle difference between the reference signal and the fault signal. The maximum correlation degree and minimum noise effect are observed when the phase angles are equated to each other by simply adjusting the reference signal's phase angle. The similar processes are repeated for the fundamental component to calculate the correlation ratio between the fundamental and fault components to find the normalized magnitude of the fault signature.

The characteristic frequencies of the well-known motor faults are given in the literature [1-4]. The most commonly reported faults in electric machines are bearing faults, eccentricity, broken rotor bar and stator faults. All of these faults are modeled as functions of both stator frequency and rotor speed. These two variables are mostly observed by drive systems to control the motor effectively. Therefore, the reference signals are generated according to the fault equations using the rotor speed and the excitation frequency to capture the associated fault signatures precisely.

4.4. Simulation Results

In order to verify the effectiveness of the proposed method, a typical line current is modeled as shown in Fig. 4.1. A few low order harmonics are added to distort the fundamental component as in the case of inverter driven motor line current. The total harmonic distortion (THD) is about 11%. Apart from the low order harmonics, relatively high amplitude white noise is added when compared to the fault signature as shown in Fig. 4.1 (a).

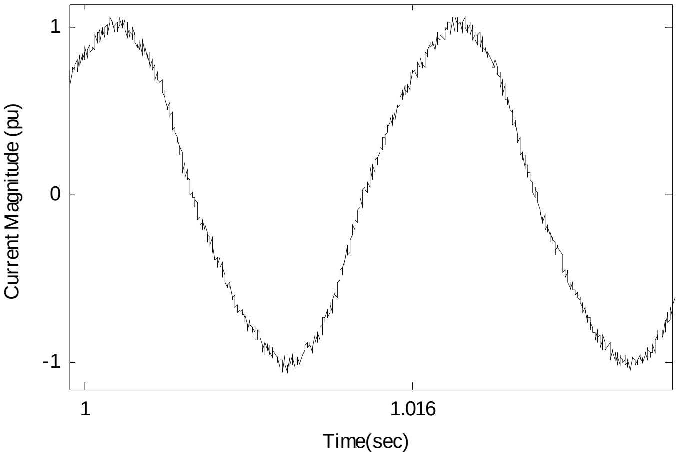

Fig. 4.1. Simulated noisy line current.

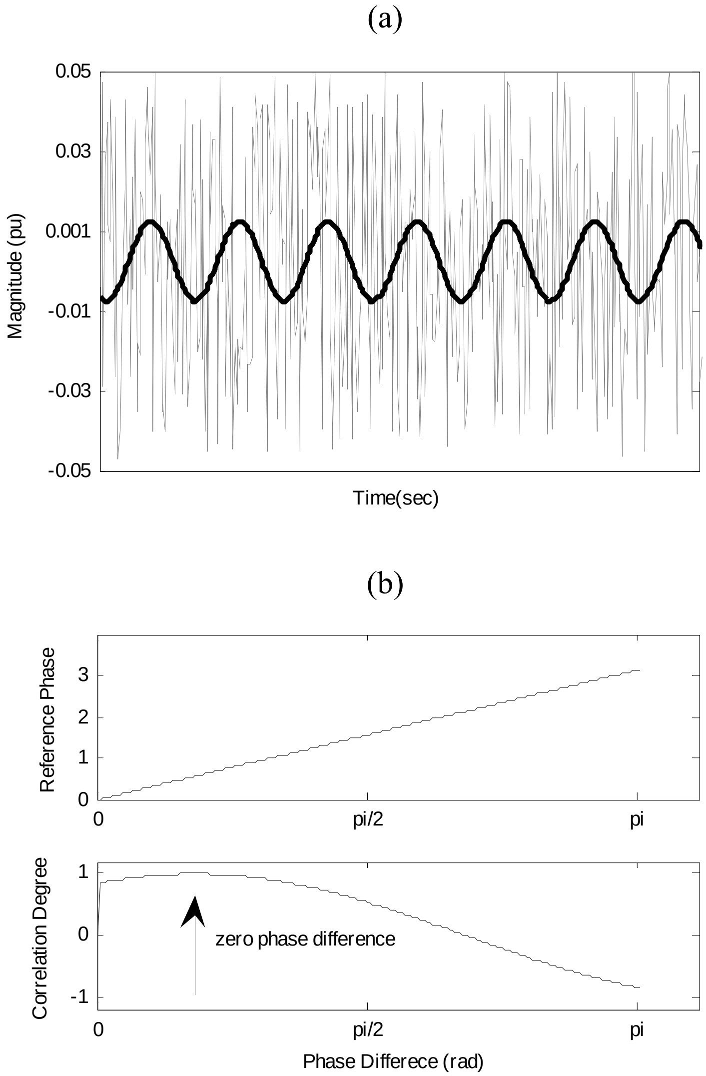

Fig. 4.2. Simulated (a) injected noise and the inspected fault component, (b) correlation degree between the reference signal and the fault component with respect to the phase angle of the reference signal.

At first, the phase angle detection is realized in order to filter out the low order harmonics including the fundamental component, and to minimize the effect of the noise component. The phase angles of the fault component and the fundamental are set to π/6 and π/2, respectively. The correlation degree between the fault component and the reference signal phase angle are given in Fig. 4.2 (b). As shown in Fig. 4.2 (b), the correlation degree increases when the phase angle of the reference signal comes close to phase angle of the fault component ($\pi/6$). Therefore, the phase angle of the reference signal is set at this point during the rest of the analysis.

Table 4.1. Simulation results under noise

Fault Component	THD%	SNR (dB)	Lock-in Result
-40 dB	~11%	-14	-39.74 dB
-40 dB	~15%	-14	-40.48 dB
-40 dB	~10%	-20	-39.38 dB
-40 dB	~14%	-20	-40.69 dB

Table 4.2. Simulation results of sampling time and number

PU Fault Component	Sampling Time	# of Samples	Lock-in Result
-40 dB	25	25	-40.09
-40 dB	25	2.5	-39.68
-40 dB	2.5	25	-39. 70
-40 dB	2.5	2.5	-39.36

A number of tests were performed under various conditions to examine the precision of the proposed method. The results are given in Table 4.1 and Table 4.2. While defining the signal to noise ratio (SNR) of the signal in Table 4.1, only the fault signal and white noise are considered. Although a significant amount of noise and low order harmonics are injected to the line current, the -40 dB fault component is successfully filtered out with less than |1dB| error. On the other hand, the effects of sampling time and number of data are tested and the results are given in Table 4.2. The sampling time is chosen to be close to the typical switching frequency interval of a motor drive. Because the proposed method processes each data at real time using the inverter processor, the samples are neither buffered in the simulations nor in the experiments. Although the precision of lock-in detector increases as the sampling time and the number of data increase, under-sampled and fewer data provide sufficient precision as shown in Table 4.2. The ratio of the number of data to the switching frequency should be set to certain values depending on the duty cycle characteristics of the motor. This ratio should be equal or less than unity under dynamically changing duty cycle operations to track the dynamic changes accurately. On the other hand, it can be set to a value larger than unity to increase the resolution where the duty cycle profile is mainly constant.

4.5. Experimental Results

A number of identical induction motors are modified to test the bearing, broken rotor bar and eccentricity faults. A conventional test bed is used in order to validate the proposed method to detect the stator current fault signature components of the 3-phase induction machine. A 3 hp induction motor is loaded by a dc generator and is driven by a custom designed Semikron inverter. The inverter control and the online fault diagnosis are performed by the 32 bit fixed-point, 150 MHz digital signal processor TMS320F2812. A signal conditioning board including the voltage and current sensors is designed and connected to the data acquisition board through the voltage amplifiers to scale the magnitude and low-pass filters to set the frequency bandwidth to a correct range. In order to obtain raw current-voltage data, a 1.25 MS/s, 16-bit resolution data acquisition card is used for offline tests. A 16 bit A/D at 256 kHz SR760 FFT spectrum analyzer is used to monitor the real time current and voltage spectrums.

4.5.1. Offline Experimental Results

In order to confirm the precision of the lock-in detector, a motor with bearing outer raceway defects is tested. In fact, the most challenging fault detection is reported to be in the case of bearing fault due to the very low amplitude of fault signatures. The challenges encountered are not only the small bearing fault signatures, but also the proximity between the floor noise level and the signature level. Therefore, computation of fault signatures becomes quite prone to noise disturbance. The reference signatures captured by the 16-bit ADC, 256 kHz sampling frequency FFT analyzer are recorded as shown in Fig. 4.3. The line current data is processed using the lock-in detector at maximum correlation degree point. It is reported that the normalized results obtained by the lock-in detector are quite satisfactory and close to the reference signatures with a very high proximity as given in Table 4.3.

Table 4.3. Normalized comparative experimental results

Signature Freq.		**143.3 Hz**	**167.5 Hz**	**383.3 Hz**	**395.4 Hz**
Healthy	FFT*	-99.55 dB	-94.99 dB	-97.80 dB	-94.84 dB
Healthy	Lock-in	-98.83 dB	-96.17 dB	-98.44 dB	-96.60 dB
Faulty	FFT*	-82.72 dB	-87.58 dB	-84.03 dB	-82.95 dB
Faulty	Lock-in	-82.93 dB	-88.02 dB	-84.94 dB	-82.78 dB

* FFT Analyzer

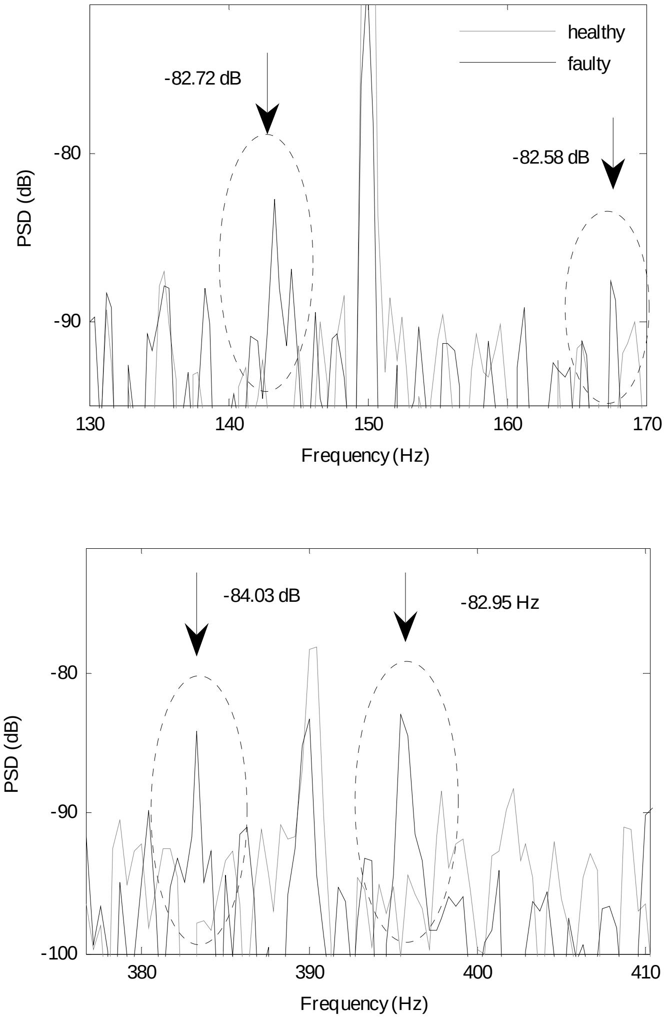

Fig. 4.3. Experimentally obtained normalized outer race bearing fault signatures.

The noise immunity of lock-in detector is tested by injecting white noise to experimentally obtained line current at constant low order harmonics THD in each step. The outer race fault signature at 143.3 Hz is measured as -82.93 dB by the lock-in detector when inherent experimental setup noise is on the line current. The effects of the added noise on the lock-in detector findings are given in Table 4.4. Although the added noise is several times higher than the inspected signature, the lock-in provides quite successful results with acceptable errors.

Table 4.4. Normalized experimental results

Fault Signature (Inherent Noise)	**Amplitude of Injected Noise**	**Lock-in Results**
-82.93 dB	-100.00 dB	-82.936 dB
-82.93 dB	-80.00 dB	-82.949 dB
-82.93 dB	-60.00 dB	-83.072 dB
-82.93 dB	-40.00 dB	-86.702 dB

4.5.2. Online Experimental Results

Similar tests are repeated online using the TMS320F2812 DSP, which is employed both for inverter control and fault signature detection. When using DSP core for both control and fault purposes, the fault code is embedded into the main control algorithm as a subroutine that processes the instantaneously measured current data. The number of data is chosen to be the same as the sampling frequency, which can be adjusted between 4k and 20k depending on the applications. The stator frequency is equated to the reference value depending on the control type. The rotor speed can either be measured using the encoder or estimated to update the signature frequencies in real time. Because the embedded ADC in TMS320F2812 has 12-bit, the quantization constraints prevent sensing signals less than -65 dB. The experiments are carried out by testing broken rotor bar and eccentric motors.

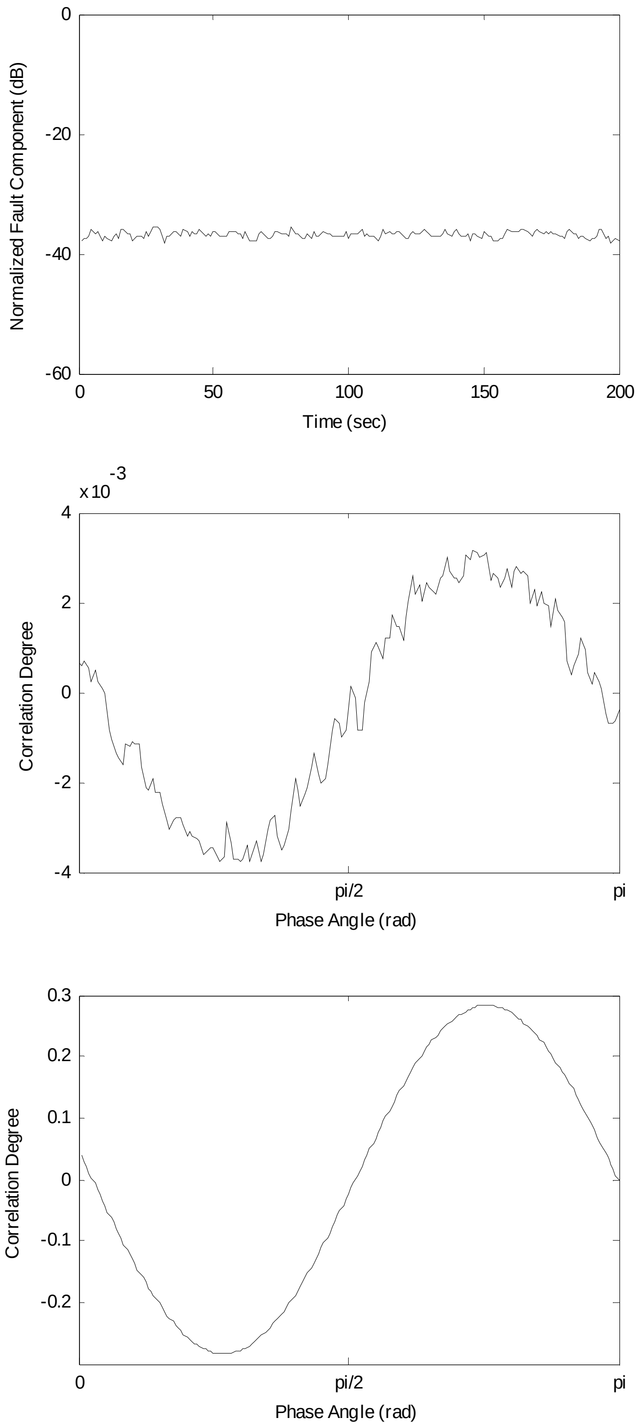

Fig. 4.4. Experimentally obtained (a) left eccentricity sideband in real time, (b) correlation degree between reference signal and the fault component, (c) correlation degree between reference signal and the fundamental component.

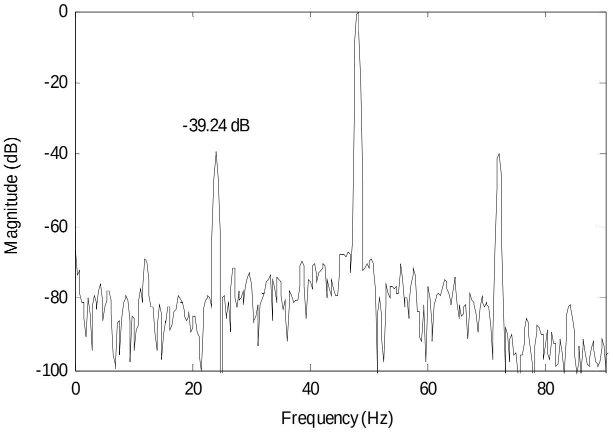

Fig. 4.4. Continued.

The results obtained in Fig. 4.4 using the DSP with 12-bit ADCs are very close to results obtained from the FFT spectrum analyzer that has two DSP core and a 16-bit ADC with a sampling rate of 256 kHz. The left sideband signature of an eccentric motor is measured to be -39.24 dB and -38.98 dB using the FFT analyzer and the DSP, respectively. It is reported that the fault signature magnitude is not remarkably affected by the switching frequency of the inverter. Since this measurement is taken when the motor is running at the steady state, the ratio of the number of data to the switching frequency is mostly taken as unity which provides sufficient resolution. The correlation of the fault component and the fundamental component with respect to the reference signals generated by the DSP are given in Fig. 4.4 (c) and 4.4 (d). It is possible to obtain smoother waveforms simply by processing more data. These online experimental results confirm that the proposed method can be adapted to the real time applications successfully.

In order to realize online lock-in of reference signal and fault signature, a few ways are possible. For instance, the phase angle difference between the reference signal and the fault signature can be calculated using the arctangent relation of the cross-correlation and the auto-correlation at each fault signature detection cycle. Next, the minimum phase angle difference point is chosen as operating point that maximize the correlation and minimize the noise effects. Once this point is detected, the rest of the fault diagnosis process can be continued at this point or it can be updated at each phase difference zero crossings.

As shown in Fig. 4.5 (a), the correlation degree of fault component is set to maximum at zero crossing of the phase difference and fixed at this point until the next zero crossing. A similar process is repeated for the fundamental component to normalize the fault component as shown in Fig 4.5 (b). Despite the decrease in precision, the phase angle scanning can be accelerated by increasing the reference signal phase angle increments in each drive control cycle. Since the period of phase angle scanning is in the range of minute, this method is appropriate for constant duty cycle steady state operations.

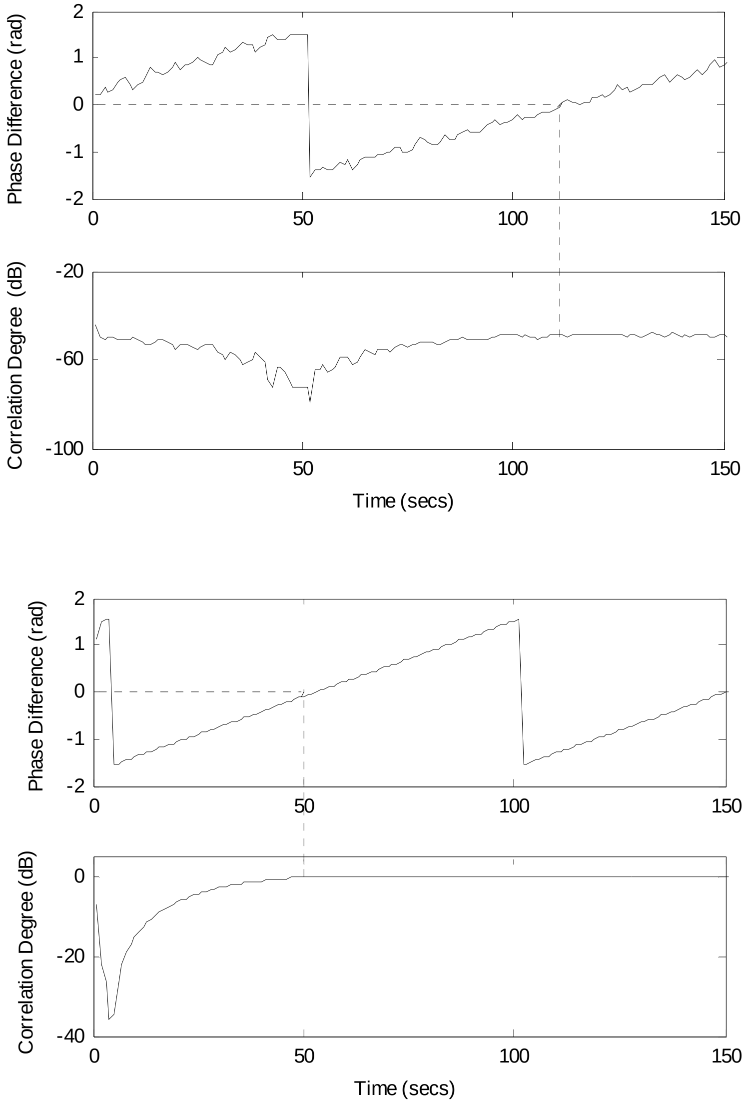

Fig. 4.5 Experimentally obtained (a) phase difference between reference signal and fault component, and normalized left eccentricity sideband correlation degree in real time, (b) phase difference between reference signal and fault component, and normalized left eccentricity sideband correlation degree in real time.

In order to examine the motors the duty cycles of which are continuously fluctuating, an alternative auto-tuning algorithm is developed. Apart from the previous method, the phase difference between the reference signal and the fault signature is continuously updated. Thanks to this method, it is possible to track fault signature not only at the steady state but during transients as well. Therefore, one can follow the dynamic characteristics of fault signatures during acceleration, deceleration and loadings. The false error warnings can be minimized employing this method and previously determined operating point dependent adaptive threshold. If there are rare measurements to be made of a current magnitude that does not change significantly in time, it may be acceptable to process as many data as possible to enhance the precision of the result. However, if there are multiple measurements to be made particularly during transients, the number of processed data should be optimized. Typically, a few drive control cycles data processing time is enough at steady state and at most one or half cycle will be sufficient during transients. It is reported that less than half a control cycle degrades precision significantly. Since the results are normalized, computation time will not affect the relative amplitude of the fault signature or the correlation degree.

In Fig. 4.6, continuous tracking of the right eccentricity sideband is given. The phase lock-in is achieved in each drive control cycle by auto-tuning algorithm. Using the phase sensitive detection, the right eccentricity sideband is measured as less than |1| dB error when compared to the FFT analyzer results.

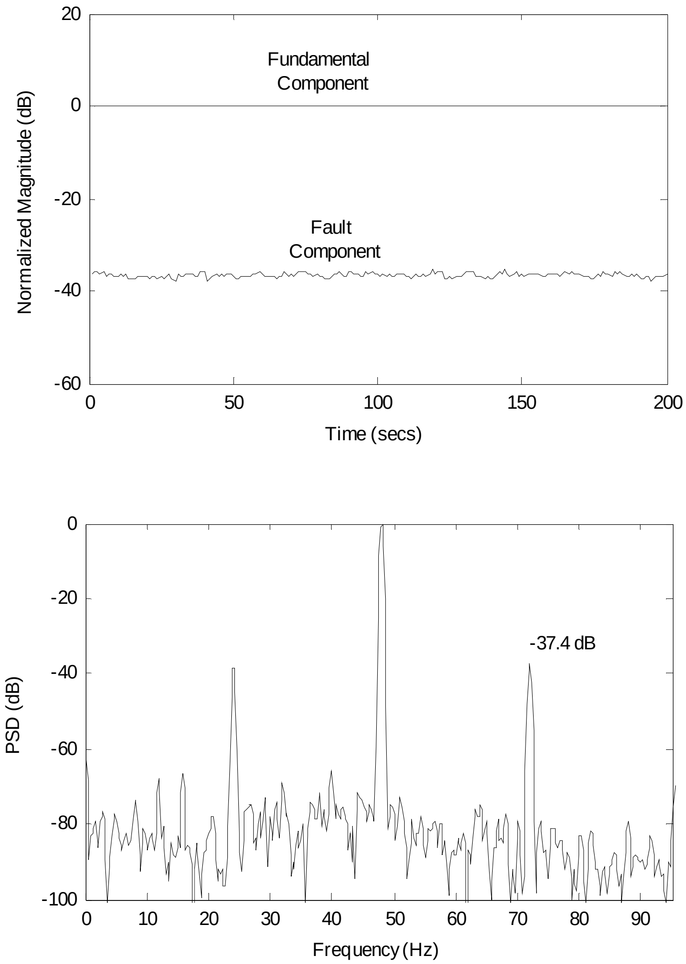

Fig. 4.6. Experimentally obtained (a) normalized fundamental and right eccentricity sideband correlation degree in real time, (b) FFT analyzer output.

In Fig. 4.7, the real time fault signature tracks are given. In Fig. 4.7 (a), the right eccentricity sideband variation is given from no-load to 0.33 pu load using the auto tuned phase sensitive lock-in detector. In Fig. 4.7 (b), the broken bar fault right sideband variation is given from 0.8 pu to 1.1 pu load. Because the excitation frequency is already continuously available in the control algorithm and the rotor frequency is measured or estimated, these parameters are used to update the fault signature frequencies given in the appendix in real time at various operating points. These results prove that the proposed method has a powerful real time fault signature tracking capability.

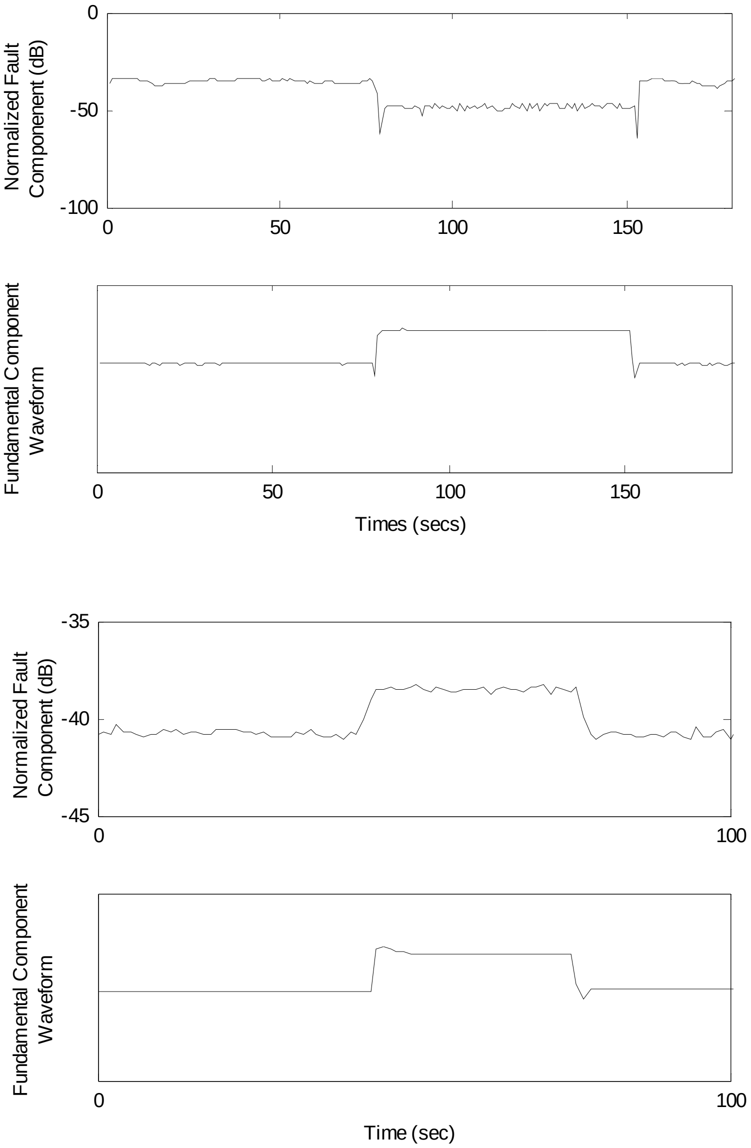

Fig. 4.7 Experimentally obtained (a) normalized right eccentricity sideband correlation degree in real time under no load and 0.33 pu load, (b) normalized broken bar fault right sideband correlation degree in real time under 0.8 pu and 1.1 pu load.

4.4. Conclusions

In this chapter, a simple noise immune real-time fault signature detection tool is presented. Since this method can easily be implemented using industries' general purpose microcontrollers without any additional hardware, PC, filters and large size memory, it can be adapted to the single and multi phase drive systems. The accuracy of the proposed method is tested experimentally and the results are compared to a commercial FFT analyzer. Furthermore, the noise suppression capability of this method is verified by injecting various amplitude white noises to the line current. All the test results confirmed that the phase sensitive lock-in detector is an excellent and promising tool for real time drive embedded fault detection systems.

CHAPTER V

ON-BOARD DIAGNOSIS OF ELECTRIC MOTORS FOR HYBRID ELECTRIC VEHICLES

5.1. Introduction

The integrity of the electric motors in work and passenger vehicles can best be maintained by monitoring its condition frequently on-board the vehicle. In this chapter, a signal processing based fault diagnosis scheme for on-board diagnosis of rotor asymmetry at start-up and idle mode is presented. Regular rotor asymmetry tests are done when the motor is running at certain speed under certain load with stationary current signal assumption. It is quite challenging to obtain these regular test conditions for long enough time during daily vehicle operations. In addition, automobile vibrations cause a non-uniform air-gap motor operation which directly affects the inductances of electric motor and results quite noisy current spectrum. Therefore, examining the condition of electric motor integrated to an HEV, regular rotor fault detection methods become impractical. The proposed method overcomes the aforementioned problems simply by testing the rotor asymmetry at zero speed. This test can be achieved and repeated during start-up and idle modes. The proposed method can be implemented at no cost basically using the readily available electric motor inverter sensors and microprocessing unit.

5.2. On Board Fault Diagnosis (OBFD) For Hybrid Electric Vehicles

It is very important for any vehicle to monitor its vital equipments continuously. Therefore, nowadays almost all vehicles are equipped with on-board diagnosis (OBD) system [62]. This system has been used for warnings and monitoring critical failures in the vehicle such as ignition, battery, oil and gasoline level, engine, brakes, etc. If a problem or malfunction is detected, OBD system set a malfunction indicator light (MIL) readily visible to the vehicle operator on the dashboard, to inform the driver that a problem existed. When illuminated, it shall display a universally recognizable symbol, or a similar phrase for each failure. OBD is a valuable tool that assists in the service and repair of vehicles by providing a simple, quick, and effective way to pinpoint problems by retrieving vital automobile diagnostics from the OBD systems [63].

According to the U.S. Code of Federal Regulations (CFR), all light-duty vehicles, light-duty trucks and complete heavy-duty vehicles weighing 14,000 pounds GVWR or less (including MDPVs) must be equipped with an onboard diagnostic (OBD) system capable of monitoring all emission-related powertrain systems or components during the applicable useful life of the vehicle. A vehicle shall not be equipped with more than one general purpose malfunction indicator light for emission-related problems; separate specific purpose warning lights (e.g. brake system, fasten seat belt, oil pressure, etc.) are permitted [63]. Although CFR's requirements for OBD are mainly related to the environmental protection purposes, safety issue in the vehicles should also be considered by using the OBD system.

The Code of Federal Regulations does not state any diagnostics requirements of electric machines in HEV. Besides battery which is quite vital electrical component in HEV, monitoring the conditions of electric machine is very critical in case of any failures such as bearing, rotor and stator faults as shown in Fig 5.1. By diagnosing the electric machine faults as early as possible, one can prolong the lifetime of the electric machine in HEV by performing maintenance before a catastrophic failure occurs. Therefore, emerging hybrid electric vehicle systems require onboard fault diagnosis as shown in Fig. 5.2, both to support critical functions of the control system and to provide cost effective maintenance.

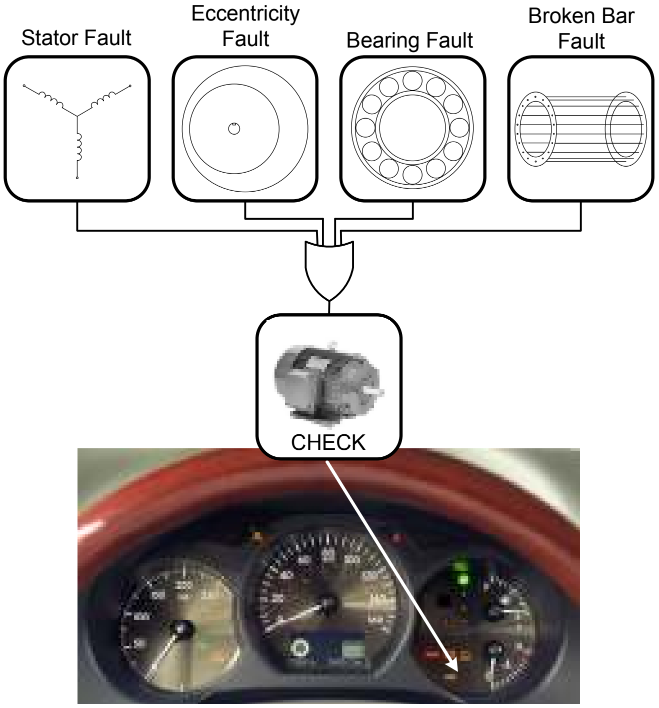

Fig. 5.1 Motor fault can be displayed in the hybrid electric vehicle instrumental cluster (Lexus GS 450h).

A catastrophic failure in an electric machine might result dangerous situations during driving especially in highway. Unless frequently monitored, an incipient fault in the machine can be propagated until it totally falls apart. Therefore, an accident afterwards might become inevitable. Once the fault diagnostic system makes any kind of severe electric motor fault decision, the traction of the vehicle can totally be taken over by combustion engine in order to prevent permanent damages and total loss of electric motor. Basically, this solution is applicable if HEV is designed based on parallel or parallel & series architectures. However, in series configurations, the ICE is directly connected to the electric motor [64]. Therefore, in series architectures the proposed solution is limited to electric faults and has partial use for mechanical faults such as bearing fault.

Mechanical vibration of vehicle degrades the fault diagnosis of electric motor integrated to the HEV. The vibration causes non uniform air-gap operation, therefore, the machine inductance oscillates. Because of this oscillation, the line current becomes noisy and the noise floor of current spectrum becomes higher. This noise in the current spectrum generated by mechanical vibration degrades the fault signature analysis results. Therefore, one of the best alternatives is condition monitoring at zero speed. Either idle modes or start up might provide long enough time to process the current data and report the condition of electric motor. On the other hand, vibrating nature of vehicle makes the use of other vibration sensitive sensors such as accelerometer impractical due to the excessive noise at sensor output. Unlike accelerometers, flux sensors etc. which are mounted on the electric motor for fault diagnosis, the current sensors are located inside the motor drive unit which is far away from the main source of vibration. Moreover, the cost of current sensor is relatively low when compared to the other sensors. Thus, one of the best alternative combinations is employing current sensors at zero speed where mechanical vibration effect is minimum.

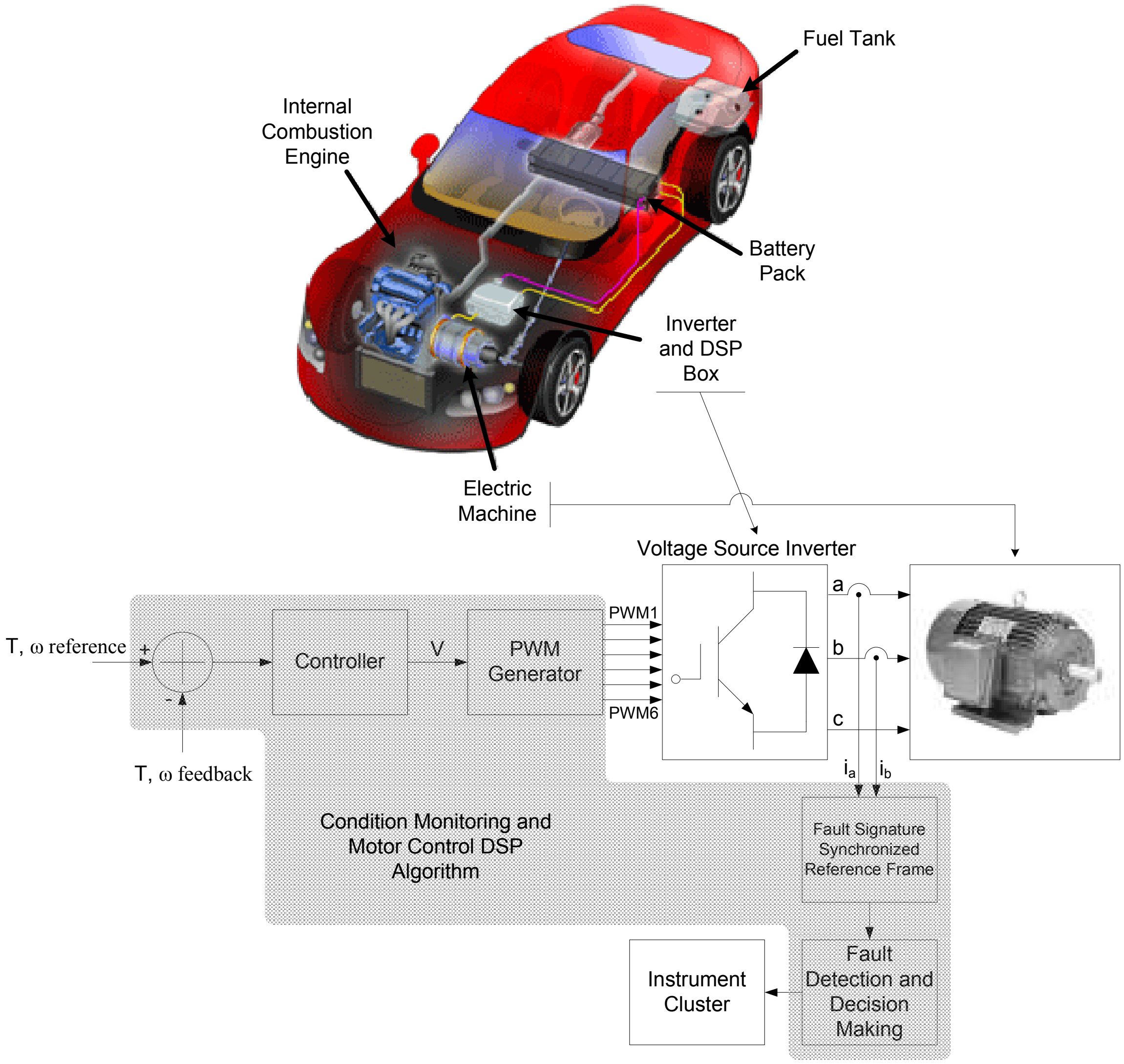

Fig. 5.2. Drive embedded fault diagnosis scheme integrated to HEV [65].

5.3. Drive Cycle Analysis for OBFD

Drive cycle is typically used by independent emissions testing laboratories to validate hybrid electric vehicle economy and emissions. The US EPA city cycle is the first 1300s of the Federal Test Procedure, FTP75, regulated cycle charted out in Fig. 5.3. Table 5.1 shows the most common drive cycles and their statistics respective of their geographical regions [66]. Other than highway mode, traffic flow is uneven, with very frequent stop-go events and long idle times as shown in Table 5.1. This is why city cycles have low average speed compared to similar performance on the US highway cycle. Because of the high percentage of stop time as shown in Table 5.1, the proposed OBFD algorithm can often be run to monitor the motor condition where the mechanical vibration is minimum. Since the current spectrum analyses mostly based on transformed signal averaging, the transient state fault signature analysis has high degradation potential. As shown in Fig. 5.3, drive cycle is dominated by transients where the motor current has non-stationary characteristics. Thus, instead of continuous condition monitoring, fault detection can be limited to start up and idle modes in order to enhance

Table 5.1 Standard drive cycles and statistics

Region	Cycle	Time Idling (%)	Average Speed (kph)
Asia-Pacific	10-15 mode	32.4	22.7
Europe	NEDC	27.3	32.2
NA-city	EPA-city	19.2	34
NA-highway	EPA-hwy	0.7	77.6
NA-US06	EPA	7.5	77.2
Industry	Real World	20.6	51

the reliability of fault decision warning. Idle stop functionality as shown in urban drive cycle in Fig. 5.3, the primary means of which is fuel consumption reduction, turns out to be a safe strategy for electric motor fault diagnostics. Every time the vehicle stops at the stop sign, traffic lights or bumped in a heavy traffic, the fault monitoring algorithm is run. If the stop (zero speed) time is not enough to finalize fault decision which is typically a few seconds, then the diagnostic result is neglected and resumed.

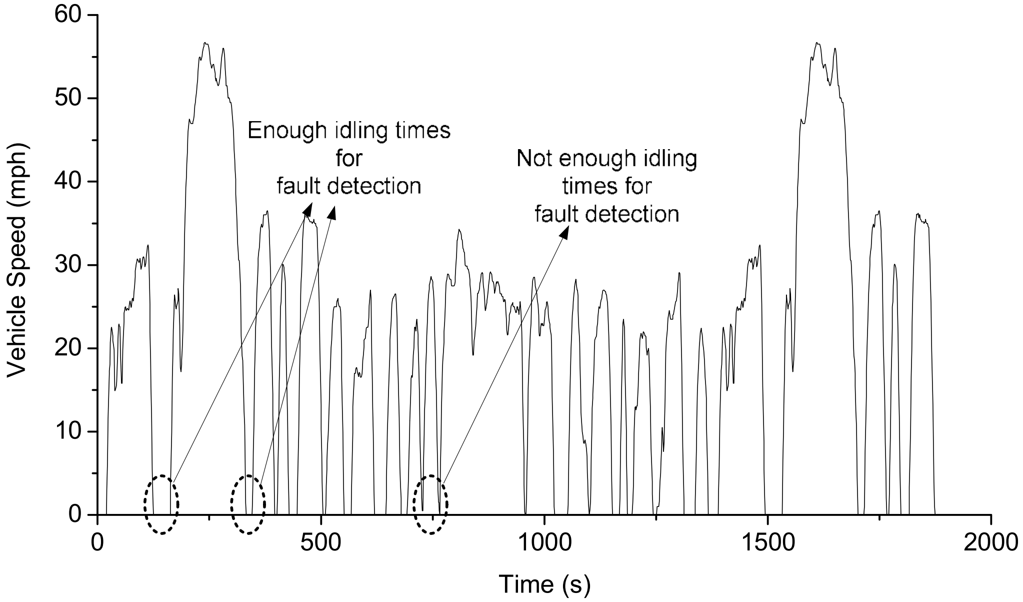

Fig. 5.3 US FTP75 city drive-cycle and fault detection points during idling.

5.4. Rotor Asymmetry Detection at Zero Speed

Broken bars in an induction motor rotor cause field asymmetry which results special sidebands at frequencies $f_s(1 \pm 2s)$ [60-61]. In real time applications, a number of challenges must be considered to detect these sidebands. For example, because these signatures directly depend on the slip value, the rotor speed should be measured precisely. Otherwise, without accurate enough speed information, it is not possible to distinguish broken bar sidebands from the fundamental component. One alternative solution might be to eliminate fundamental component using a notch filter for line driven motors. However, this solution is not applicable to adjustable speed drive systems due to dynamically changing stator frequency. Furthermore, notch filter might cause sideband suppression unless a sufficient loading is not provided during the tests. Another alternative is to estimate the rotor speed during the operation which brings extra computational burden. However, at low speed range most of the speed estimation algorithms cannot provide precise information. Therefore, high speed operation must be guaranteed in order to obtain high precision speed value for sensorless broken bar detection.

Next, the motor should be loaded at certain torque value smoothly in order to raise these sidebands and separate them from the fundamental component in the current spectrum. Smooth and proper loading might not be available for various applications to test the rotor asymmetry. The proposed method detects broken bars in real time without employing speed sensor and loading systems. Some other external hardware employed in previous works [60-61] such as the data acquisition systems, analog filters, and etc. are also eliminated.

The test is implemented at zero speed; therefore there is no need for speed measurement or speed estimation. The rotor is locked mechanically or electrically using dc braking. Because the injected signal to test the rotor asymmetry is below 10 % of rated voltage values, the generated torque during the test is negligible. Thus, broken rotor bar test can be implemented without an additional featured loading system. The $f_s(1+2s)$ term is caused by torque vibrations [26] and cause electromechanical chain interaction between the rotor and the stator that result many asymmetrical signatures in the spectrum. Therefore, low frequency range is dominated by consecutive asymmetry signatures which sophisticate fault analysis as shown in Fig 5.4 (a).

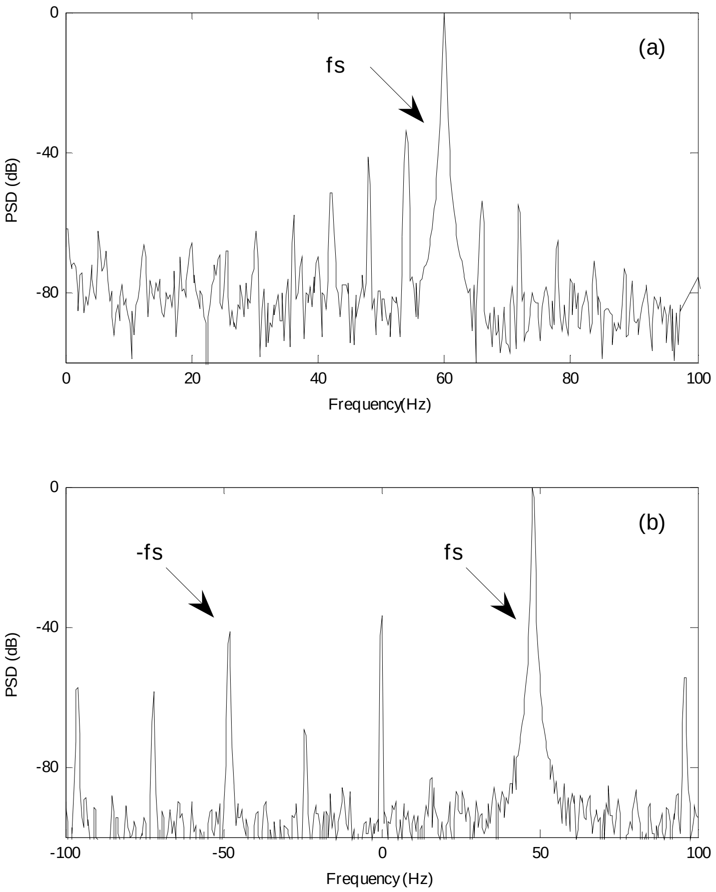

Fig. 5.4. Current spectrum of broken bar motor (a) regular test (b) zero speed test.

Since the slip is maximum when the rotor is stationary, the existing consecutive signatures are quite far away from each other as shown in Fig 5.4 (b). Indeed, at zero speed these terms vanish theoretically and the spectrum is quite clean when compared to the current spectrum at rated speed and rated torque operation.

The method presented here focuses on $f_s(1-2s)$ term. At zero speed s=1, thus the $f_s(1-2s)$ term is at frequency of $(-f_s)$. Single-phase reference frame analyses do not work for negative frequency; therefore three-phase current vectors are transformed to complex current space vector. Single-phase real or imaginary current analyses are insensitive to vector rotation direction, thus they find superposition of the left sideband and the fundamental component at the excitation frequency (f_s). In order to compute the left sideband and the fundamental components separately, the current space vector fault relevant frequencies are examined experimentally.

In Fig. 5.5 and Fig 5.6, the real time fault signature tracking result is given when the motor is injected low voltage at standstill near the rated current. Both the fault signature magnitude at $(-f_s)$ and the fundamental component at (f_s) computed simultaneously and separately in real time by the DSP in order to obtain the normalized fault signature magnitude.

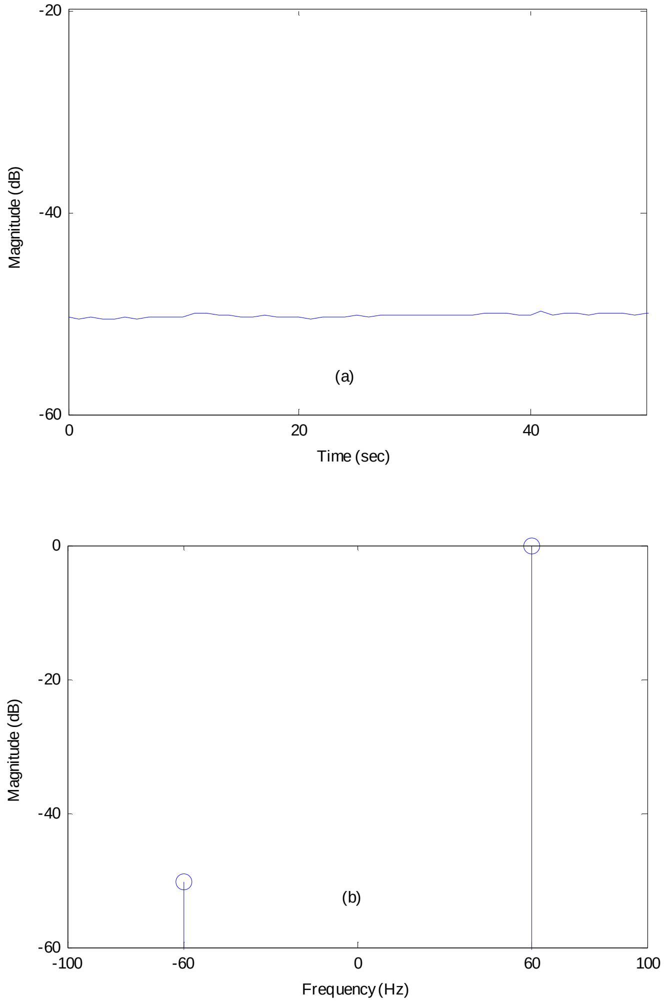

Fig. 5.5. Normalized left sideband magnitude of a healthy motor obtained by the DSP in real time at standstill (I = 9A, V/Hz =1.0, f=48 Hz), (a) time-frequency domain, (b) frequency domain.

In order to verify the proposed method, a number of experiments implemented under various Volts/Hz ratios, line currents, and frequencies. It is reported that, if high enough current is supplied around or higher than the rated current, under all conditions the healthy and faulty motors can be distinguished easily using the proposed method. In Fig. 5.5, fault signature frequencies of a healthy motor are examined when Volts/Hz is set to 1.0 at 48 Hz. In Fig. 5.5 (a), DSP continuously computes and updates the normalized left sideband of healthy motor current spectrum in each second. Fig. 5.5 (b) depicts an instant magnitude of left sideband component relative to fundamental in frequency domain.

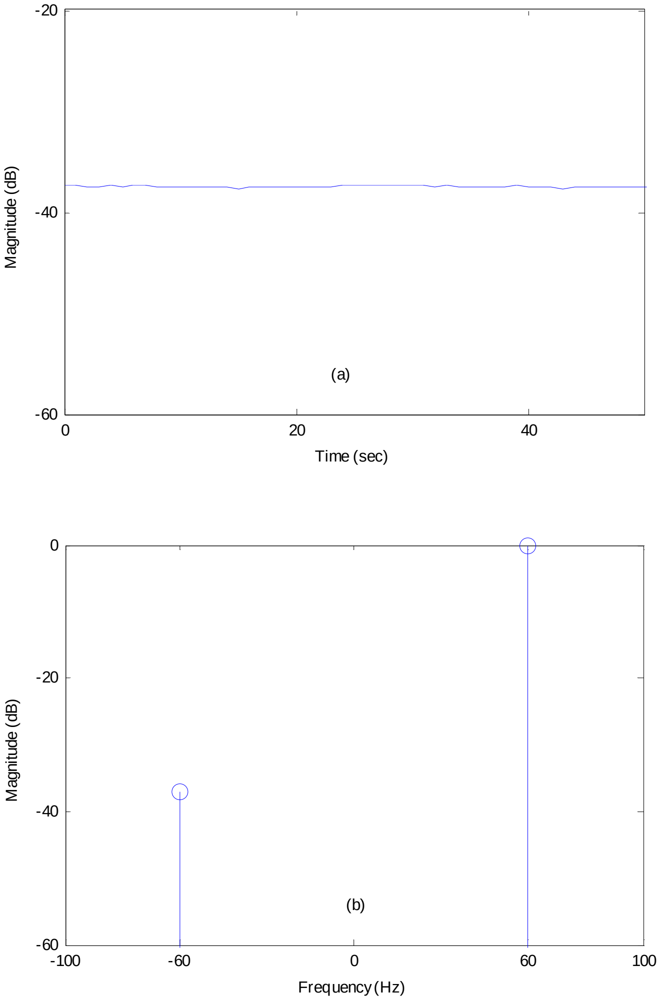

Fig. 5.6. Normalized left sideband magnitude of a faulty motor obtained by the DSP in real time at standstill (I = 9A, V/Hz =1.0, f=48 Hz), (a) time-frequency domain, (b) frequency domain.

A similar test is repeated for the motor which has less than 10 % broken bars on the cage and the results are shown in Fig. 5.6 (a) and (b). When Fig 5.5 and Fig. 5.6 are compared to each other, it is clearly seen that under the same conditions the left sideband is increased by 13 dB which is high enough to distinguish healthy and faulty motors from each other.

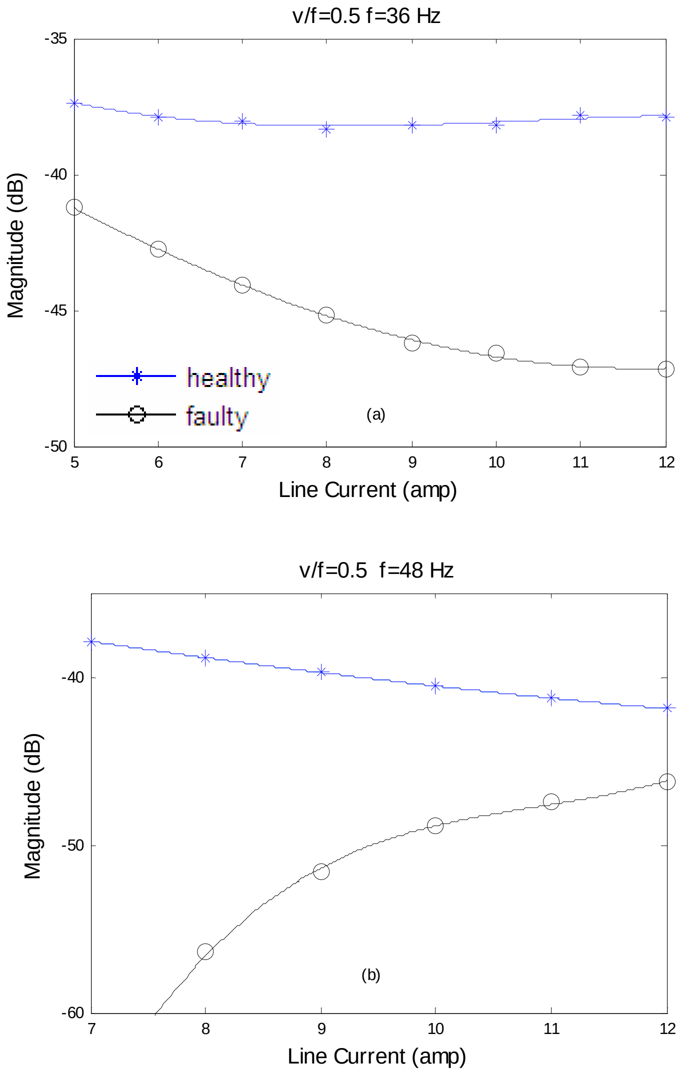

Fig. 5.7. Normalized left sideband magnitude obtained by the DSP in real time vs line current (Volts/Hertz = 0.5), (a) 36Hz, (b) 48Hz, (c) 60 Hz (d) 72 Hz.

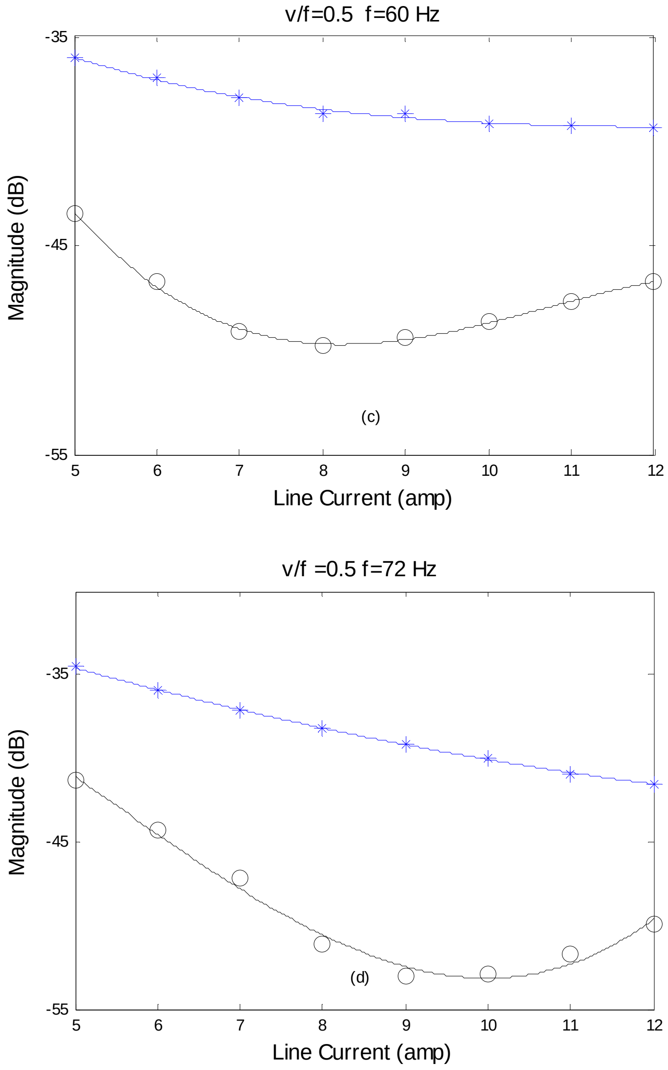

Fig. 5.7. Continued.

In Fig. 5.7, the normalized fault component magnitudes are given at various frequencies when the Volts/Hertz ratio is equal to 0.5. The comparative results are as promising as the regular (full-load, rated speed) broken bar test. It is reported that the difference between the left sideband of healthy and faulty motor fault signatures are very close to regular test results. Therefore, the same results can be obtained at standstill without the need for any external hardware just before the motor startup or at idle mode in a few seconds.

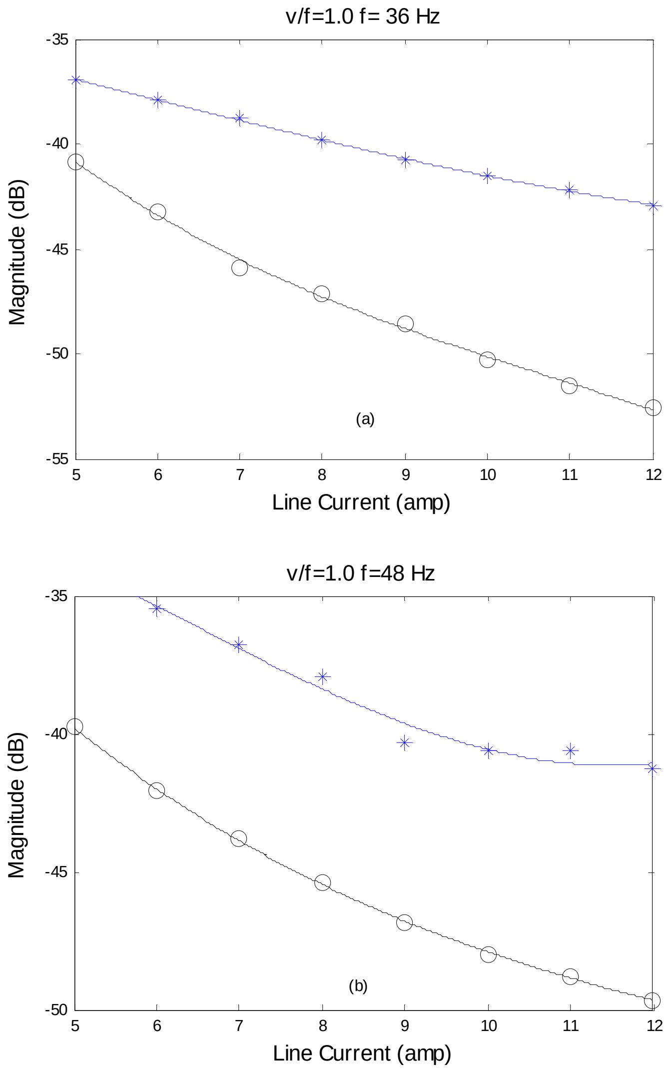

Fig. 5.8. Normalized left sideband magnitude obtained by the DSP in real time vs line current (Volts/Hertz = 1.0), (a) 36Hz, (b) 48Hz, (c) 60 Hz.

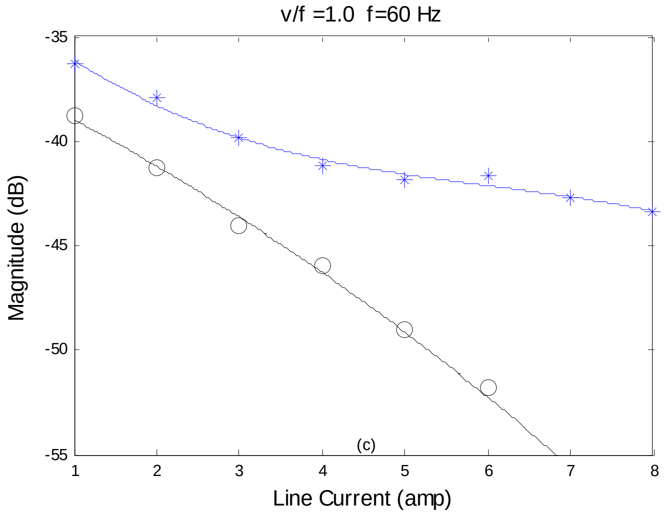

Fig. 5.8. Continued.

The same test is implemented when the v/f ratio is set to 1.0 to examine the effect of magnetizing current. It is noticed that the results are close to the ones obtained at two different v/f ratio tests as shown in Fig 5.8 and Fig 5.9. Thus, magnetization current level has limited effect on the left sideband at standstill and can be ignored as fault analysis parameter.

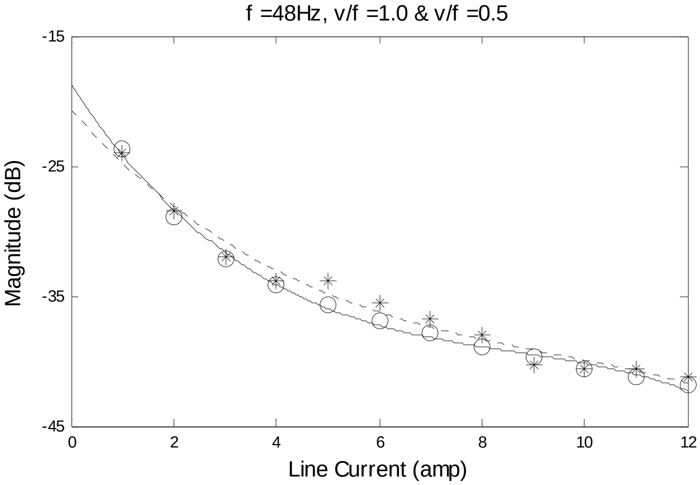

Fig. 5.9. Normalized left sideband magnitude obtained by the DSP in real time vs line current (Volts/Hertz = 1.0 and 0.5, *f*=48Hz).

5.5. Conclusions

Condition monitoring and fault detection of electric motors in hybrid electric vehicles (HEVs) are quite vital for safety and cost-effective maintenance. This chapter proposes a simple online on-board fault diagnosis (OBFD) of induction motor for HEVs at start-up and idle (standstill) conditions based reference frame theory. The major advantages of the method are very fast convergence time, no need to an additional sensor or hardware, robust and reliable, speed sensorless implementation, and zero speed application making it highly robust against the mechanical vibrations effects. It is experimentally shown that the proposed method detects the rotor asymmetry fault signatures at start-up and idle mode (zero speed) and determines the severity of the fault. The proposed solution can easily be extended to the other faults for a complete motor monitoring.

CHAPTER VI

CONCLUSIONS

In this chapter the research work presented in the earlier chapters are summarized. The challenges of inverter driven motor fault diagnosis using line current signature brought to attention and the fault signatures due to inverter harmonics are modeled. A robust signal processing based real time fault diagnosis algorithm is proposed and applied to bearing, eccentricity and broken bar faults. In case of small fault signals detection noisy line current, a noise immune algorithm is successfully implemented both theoretically and experimentally. Finally, the proposed fault detection algorithms are extended for HEV applications to enhance the reliability of passenger and work vehicles.

6.1. Summary of the Research

This dissertation is mainly concerned with real time fault diagnosis of inverter driven induction motors. A drive embedded fault detection schematic at no cost is proposed to capture fault signatures in real time quite rapidly. Inverter harmonics advantages and line current noise disadvantages have been investigated in detail.

In chapter I, a brief overview of the induction motor faults, their cause and detection techniques are explained roughly. Next the state of the art is presented and the new trends are indicated based on market demand.

The effects of inverter harmonics on motor current fault signatures are studied in detail in chapter II. According to theory and experimentation given in this chapter, the fault signatures caused by the inverter harmonics are similar and comparable to those generated by the fundamental harmonic of the line current. Unlike the utility-driven motor, monitoring the current of the inverter-fed motor is considerably noisy, which can mask the fault signatures and render a wrong fault warning. Therefore, the proposed additional fault data processing technique is expected to support the inverter-fed motor fault decision making algorithms effectively. The theoretically derived bearing fault relations are found to match the experimental results. In order to confirm these claims, outer race bearing faults are tested and the line current spectrum of the faulty motor is compared to the healthy one.

Next, apart from the conventional applications, it is reported that the reference frame theory can also be applied to fault diagnosis of electric machinery systems as a powerful toolbox to find the magnitude and phase quantities of fault signatures. The reference frame theory and its applications to fault diagnosis are explored in chapter III. The core idea is to convert the associated fault signature to a dc quantity, followed by calculating the signal average value in the new reference frame to filter out the rest of the signal harmonics, i.e. its ac components. Broken rotor bar and rotor eccentricity faults are experimentally tested both offline using the data acquisition system, and online employing the TMS320F2812 DSP to prove the efficacy of the proposed tool.

The proposed method has been theoretically and experimentally proven to detect the fault harmonics and determine the existence and the severity of machine faults. The advantages of this method include the following: (1) no need to employ external hardware or a PC running a high level program; (2) provides instantaneous fault monitoring using a DSP controller in real time; (3) embedded into the motor drive; thus, readily available drive sensors and the core processor are used without employing additional hardware; (4) no need to store machine currents data, and thus no need for large memory size; (5) very short convergence time capability; (6) immune to non-idealities like sensor dc offsets, imbalance, etc. ; (7) no need for a notch filter to filter out the fundamental harmonic; (8) steady state or stationary current signal assumptions are not necessary; (9) a familiar concept for motor control engineers; and (10) applicable to all multi-phase and single phase motors.

In chapter IV, digital signal processor (DSP)-based phase-sensitive motor fault signature detection is presented. The implemented method has a powerful line current noise suppression capability while detecting the fault signatures. Because the line current of inverter driven motors involve low order harmonics, high frequency switching disturbances, and the noise generated by harsh industrial environment; the real-time fault analyses yield erroneous or fluctuating fault signatures. This situation becomes a significant problem when signal to noise ratio (SNR) of the fault signature is quite low. It is theoretically and experimentally shown that the proposed method can determine the normalized magnitude and phase information of the fault signatures even in the presence of noise, where the noise amplitude is several times higher than the signal itself.

In chapter V, a signal processing based fault diagnosis scheme for on-board diagnosis of rotor asymmetry at start-up and idle mode is presented. Regular rotor asymmetry tests are done when the motor is running at certain speed under certain load with stationary current signal assumption. It is quite challenging to obtain these regular test conditions for long enough time during daily vehicle operations. In addition, automobile vibrations cause a non-uniform air-gap motor operation which directly affects the inductances of electric motor and results quite noisy current spectrum. Therefore, examining the condition of electric motor integrated to an HEV, regular rotor fault detection methods become impracticable. The proposed method overcomes the aforementioned problems simply by testing the rotor asymmetry at zero speed based on reference frame theory as mentioned in chapter III.

REFERENCES

[1] G. B. Kliman, R. A. Koegl, J. Stein, R. D. Endicott, and M. W. Madden, “Noninvasive detection of broken rotor bars in operating induction motors,” *IEEE Transactions on Energy Conversions*, vol. 3, pp. 873–879, Dec. 1988.

[2] R. Schoen, T. Habetler, F. Kamran, and R. Bartfield, “Motor bearing damage detection using stator current monitoring,” *IEEE Transactions on Industry Applications*, vol. 31, no. 6, pp. 1274–1279, Nov./Dec. 1995.

[3] M. E. H. Benbouzid, “A review of induction motors signature analysis as a medium for faults detection,” *IEEE Transactions on Industrial Electronics*, vol. 47, no. 5, pp. 984–993, Oct. 2000.

[4] S. Nandi, M. Bharadwaj and H. A. Toliyat, “Performance analysis of a three-phase induction motor under mixed eccentricity condition,” *IEEE Transactions on Energy Conversions*, vol. 17, pp. 392-399, Sep. 2002.

[5] D. G. Dorrell, W. T. Thomson, and S. Roach, “Analysis of airgap flux, current, vibration signals as a function of the combination of static and dynamic air gap eccentricity in 3-phase induction motors,” *IEEE Transactions on Industry Applications*, vol. 33, pp. 24–34, Jan. 1997.

[6] M.J. Devaney and L. Eren, “Detecting motor bearing faults,” *IEEE Instrumentation & Measurement Magazine*, vol. 7, issue 4, pp. 30-36, Dec 2004.

[7] C. Riley,K. Lin, T. Habetler, G.B Kliman, “Stator current harmonics and their causal vibrations: A preliminary investigation of sensorless vibration monitoring applications,” *IEEE Transactions on Industry Applications*, vol. 35, no. 1, pp. 94-99, Jan. 1999.

[8] Nandi, S.; Toliyat, H.; Li, X; “Condition monitoring and fault diagnosis of electrical motors—A review”, *IEEE Transactions on Energy Conversions*, vol. 20, no. 4, pp. 719 – 729, Dec. 2005.

[9] Oppenheim, A. V. and R. W. Schafer, *Discrete-Time Signal Processing*, New York: Prentice-Hall, 1989.

[10] S. S. Haykin and B. Van Veen, *Signals and Systems*, New York: John Wiley & Sons, 1998.

[11] B. Yazici, and G. B. Kliman, “An adaptive statistical time-frequency method for detection of broken bars and bearing faults in motors using stator current”, *IEEE Transactions on Industry Applications,* pp: 442-452, March 1999.

[12] H.Ocak, “Fault detection, diagnosis and prognosis of rolling element bearings: Frequency domain methods and hidden markov modelling,” PhD Dissertation, School of Electrical Engineering, Case Western Reserve University, Cleveland 2004.

[13] H. Douglas, P. Pillay,A. K. Ziarani “Broken rotor bar detection in induction machines with transient operating speeds”, *IEEE Transactions on Energy Conversions*, vol. 20, pp. 135-141, Mar. 2005.

[14] L. Eren, “Bearing damage detection via wavelet package decomposition of stator current,” PhD Dissertation, School of Electrical Engineering, University of Missouri-Columbia, 2002.

[15] Ilonen, J., Kamarainen, J.-K., Lindh, T., Ahola, J., Kälviäinen, H., Partanen, J., “Diagnosis tool for motor condition monitoring”, *IEEE Transactions on Industry Applications*, vol. 41, pp. 963-971, April 2005.

[16] R R Schoen, B K Lin, F G Habetter, H J Shlog and S Farag: “An unsupervised on-line system for induction motor fault detection using stator current monitoring”, *IEEE Transactions on Industry Applications*, vol. 31, no. 6, pp. 1280-1286, November/December 2005.

[17] J.R. Stack, R.G. Harley and T.G. Habetler, “An amplitude modulation detector for fault diagnosis in rolling element bearings”, *IEEE Transactions on Industrial Electronics*, vol. 51, no. 5, Oct. 2005 pp 1097-1102.

[18] G.Stone, J. Kapler “Stator winding monitoring”, *IEEE Industry Applications Magazine*, September/October 1998.

[19] E.L. Brancato “Insulation aging”, *IEEE Transactions on Dielectrics and Electrical Insulation*, vol. EI-13, no. 4, August 1978.

[20] *Handbook to Assess Stator Insulation Mechanism*, EPRI EL-5036, vol. 16, New York: Power Plant Electrical Reference Series.

[21] Douglas, J “Hydro generator failure”, *IEEE Power Engineering Review*, vol. 8, no. 11, pp. 4-6, November 1988

[22] G. Stone, S. Campbell, and S. Tetreault, “Inverter-fed drives: Which motor stators are at risk”, *IEEE Industry Application Magazine*, vol. 6, pp. 17–22, Sept. /Oct. 2000.

[23] B.Fernando, “Online Stator winding fault diagnosis in inverter-fed AC machines using high-frequency signal injection”, *IEEE Transactions on Industry Application*, vol. 39, no 4, August. 2003.

[24] S.Lee, G.B. Kliman, “An online technique for monitoring the insulation condition of ac machine stator windings”, *IEEE Transactions on Energy Conversions*, vol. 20, no 4, Dec. 2005.

[25] G.C.Stone “Advancements during the past quarter century in on-line monitoring of motor and generator winding insulation”, *IEEE Transactions on Dielectrics and Electrical Insulation*, vol. 9, no. 5, October 2002.

[26] F. Filippetti, G. Franceschini, C. Tassoni, and P. Vas, “AI techniques in induction machines diagnosis including the speed ripple effect,” *IEEE Transactions on Industry Applications*, vol. 34, pp. 98-108, 1998.

[27] N.M. Elkasabgy, A.R. Eastham, G.E. Dawson, "Detection of broken bars in the cage rotor on an induction machine" *IEEE Transactions on Industry Applications,* vol. 28, no. 1, pp. 165 – 171, Jan/Feb 1992.

[28] K.R. Cho, J.H. Lang, S.D. Umans, "Detection of broken rotor bars in induction motors using state and parameter estimation" *IEEE Transactions on Industry Applications*, vol. 28, no. 3, pp.702 – 709, May/Jun 1992.

[29] J. Milimonfared, H.M. Kelk, S. Nandi, A.D. Minassians, H.A. Toliyat, "A novel approach for broken-rotor-bar detection in cage induction motors" *IEEE Transactions on Industry Applications,* vol. 35, no. 5, pp. 1000-1006, Sep/Oct 1999.

[30] S.Nandi “Detection of stator faults in induction machines using residual saturation harmonics”, *IEEE Transactions on Industry Applications,* vol.42, no.5, pp. 963-971, Sept. 2006.

[31] A. Bellini, F. Filippetti, G. Franceschini, and C. Tassoni, “Closed-loop control impact on the diagnosis of induction motors faults,” *IEEE Transactions on Industry Applications*, vol. 35, no. 1, pp. 94-99, Jan. 1999.

[32] X. Huang, T.G. Habetler, “Detection of mixed air gap eccentricity in closed-loop drive connected induction motors,” *IEEE International Symposium on Diagnostics for Electric Machines, Power Electronics and Drives’ 03*, Atlanta-2003.

[33] O. Duque, M. Pérez, and D. Moríñigo, “Detection of bearing faults in cage induction motors fed by frequency converter using spectral analysis of line

current" *IEEE International Electric Machines and Drives Conference'05*, San Antonio, 2005.

[34] B. Raison, G. Rostaing, O. Butscher, and S. Maroni, "Investigation of algorithms for bearing fault detection in induction drives," *IEEE Industrial Electronics'02*, pp. 1696-1701, 2002,.

[35] R. Wieser, C. Kral, F. Pirker, and M. Schagginger, "On-line rotor cage monitoring of inverter-fed induction machines by means of an improved method," *IEEE Transactions on Power Electronics*, vol. 14, pp. 858–865, Sept. 1999.

[36] F. Briz, M.W. Degner, A.B. Diez, and J. Manuel Guerrero, "Online diagnostics in inverter-fed induction machines using high-frequency signal injection," *IEEE Transactions on Industry Applications*, vol. 40, no. 4, pp. 1153-1161, Jul-Aug. 2004.

[37] N. Afshari, "A model-based technique for rolling element bearing fault detection," PhD Dissertation, School of Systems, Control and Industrial Engineering, Case Western Reserve University, Cleveland, 1998.

[38] P.L. Alger, *The Nature of Induction Machines*, New York: Gordon and Beach, 1965.

[39] B. Heller, V.Hamata, *Harmonic Field Effects in Induction Machines*, New York: Elsevier Scientific, 1977.

[40] D. Rice, "A detailed analysis of six-pulse converter harmonic currents," *IEEE Transactions on Industry Applications*, vol. 30, no.2, 1994, pp 294-304.

[41] J. Phipps, and P. Nelson. "A harmonic distortion control technique applied to six-pulse bridge converters," *IEEE Transactions on Industry Applications*, vol. 29, no.3, pp. 616-624, 1993.

[42] Y. Plotkin, M. Stiebler, D. Hofmeyer, "Sixth torque harmonic in PWM inverter-fed induction drives and its compensation," *IEEE Transactions on Industry Applications*, vol. 41, no.4, pp. 1067-1074, 2005.

[43] R. Sepe, J.H. Lang, "Inverter nonlinearities and discrete-time vector current control," *IEEE Transactions on Industry Applications*, vol. 30, no.1, pp. 62-70, 1994.

[44] D. Antic, J.B. Klaassens, W. Deleroi, "Side effects in low-speed ac drives," in *Proc. IEEE-Power Electronics Society Meeting*, pp. 998–1002, 1994.

[45] B. Ayhan, M. Chow, “Multiple signature processing-based fault detection schemes for broken rotor bar in induction motors,” *IEEE Transactions on Energy Conversion*, vol. 20, no. 2, pp. 336-343, June 2005.

[46] N. Arhtur and J. Penman, “Induction machine condition monitoring with higher order spectra,” *IEEE Transactions on Industrial Electronics*, vol. 47, pp.1031–1041, Oct. 2000.

[47] S. Nandi, S. Ahmed and H.A. Toliyat, “Detection of rotor slot and other eccentricity related harmonics in a three phase induction motor with different rotor cages,” *IEEE Transactions on Energy Conversions*, vol. 16, pp. 253-260, Sep. 2001.

[48] M.J. DeBortoli, S.J. Salon, and C.J. Slavic, “Effect of rotor eccentricity and parallel winding on induction machine behavior: A study using finite element analysis,” *IEEE Transactions on Magnetics*, vol. 29, no. 2, pp. 1676–1682, March 1993.

[49] A. Bellini, F. Filippetti, G. Franceschini, and C. Tassoni, “Quantitative evaluation of induction motor broken bars by means of electrical signature analysis,” *IEEE Transactions on Industry Applications*, vol. 37, pp. 1248–1255, Sept./Oct. 2001.

[50] C.C.M. Cunha, R.O.C. Lyra, B.C. Filho, “Simulation and analysis of induction machines with rotor asymmetries,” *IEEE Transactions on Industry Applications*, vol. 41, pp. 18–24, Jan. /Feb. 2005.

[51] S. Nandi, X. Li and H.A. Toliyat, “Condition monitoring and fault diagnosis of electrical motors—A review,” *IEEE Transactions on Energy Conversion*, vol. 20, pp. 719-729, Dec. 2005.

[52] I.J. Pitel, S.N. Talukdar, and P. Wood, “Characterization of programmed-waveform pulse width modulation,” *IEEE Transactions on Industry Applications*, vol. 16, pp. 707–715, 1980.

[53] J.R. Wells, J.R. Nee, J.R., P.L. Chapman, and P.T. Krein, “Selective harmonic control: A general problem formulation and selected solutions” *IEEE Transactions on Power Electronics*, vol. 20, pp. 1337-1345, Nov. 2005.

[54] H. Henao, C. Demian, and G.A. Capolino, “Analytical approach of the stator current frequency harmonics computation for detection of induction machine rotor faults,” *IEEE Transactions on Industry Applications*, vol. 41, pp. 801–807, 2005.

[55] J. Hsu, "Monitoring of defects in induction motors through air-gap torque observation," *IEEE Transactions on Industry Applications*, vol. 31, pp. 1016-1021, 1995.

[56] F. Filippetti, G. Franceschini, C. Tassoni, and P. Vas, "AI techniques in induction machines diagnosis including the speed ripple effect," *IEEE Transactions on Industry Applications*, vol. 34, pp. 98-108, 1998.

[57] P. Krause, O. Wasynczuk, and S. Sudhoff, *Analysis of Electric Machinery*, Piscataway, NJ: IEEE Press, 1995.

[58] Chee-Mun Ong, *Dynamic Simulation of Electric Machinery Using Matlab/Simulink,* New York: Prentice Hall, 1998.

[59] V.Ingle and J. Proakis, *Digital Signal Processing Using MATLAB*, Pacific Grove, CA: Brookes/Cole, 2000.

[60] C. Kral, F. Pirker, and G. Pascoli, "Detection of rotor faults in squirrel-cage induction machines at standstill for batch tests by means of the vienna monitoring method", *IEEE Transactions in Industry Applications*, vol. 38, no. 3, pp. 618-624, May 2002.

[61] H. Henao, C. Demian and G.A. Capolino, "Detection of induction machines rotor faults at standstill using signals injection", *IEEE Transactions in Industry Applications*, vol. 41, no. 6, pp. 1550-1559, Nov 2004.

[62] R. K. Jurgen, *On and Off-board Diagnostics*, Warrendale, PA: Society of Automotive Engineers, 2000.

[63] Office of the Federal Register (U.S.), Code of Federal Regulations, Title 40, Protection of Environment. Washington, DC: Office of the Federal Register, 2006.

[64] M. Ehsani, Y. Gao, S. E. Gay, and A. Emadi, *Modern Electric, Hybrid Electric, and Fuel Cell Vehicles: Fundamentals, Theory, and Design*, 1st ed. Boca Raton, FL: CRC Press LCC, 2004.

[65] IEEE Power Electronics Society Newsletter, vol. 19, no. 1, pp. 1, First Quarter 2007.

[66] J. M. Miller, *Propulsion Systems for Hybrid Vehicles*, Stevenage, U.K.: Peter Peregrinus Ltd., 2004.

VITA

Bilal Akin received the B.S. and M.S. degrees, both in electrical engineering, from the Middle East Technical University, Ankara, Turkey, in 2000 and 2003, respectively. In September 2003, he joined the doctoral program in the department of Electrical and Computer Engineering at Texas A&M University and received his Ph.D. in August 2007. He worked in the Electrical Machines and Power Electronics Laboratory, in the Department of Electrical Engineering at Texas A&M University, College Station, Texas, with Dr. Hamid A. Toliyat as his advisor until May 2005. Since 2005, he has been a Research and Development Engineer with Toshiba Industrial Division, Toshiba International Corporation, Houston, TX. His current research interests include advanced control methods in motor drives, fault diagnosis of electric machinery, machine design, and digital signal processor-based industrial applications.

Bilal Akin is a student member of the IEEE.

He can be reached in c/o

Dr. Hamid A. Toliyat
Electrical Machines & Power Electronics Laboratory
Department of Electrical Engineering
TAMU 3128
Texas A&M University
College Station, Texas 77843-3128